A Thesis Submitted for the Degree of PhD at the University of Warwick

Permanent WRAP URL:

http://wrap.warwick.ac.uk/96799

Copyright and reuse:

This thesis is made available online and is protected by original copyright.

Please scroll down to view the document itself.

Please refer to the repository record for this item for information to help you to cite it.

Our policy information is available from the repository home page.

For more information, please contact the WRAP Team at: wrap@warwick.ac.uk

warwick.ac.uk/lib-publications

Synthesis and characterisation of organophosphazene and porous carbon materials for energy storage applications

by

George S. Pappas

A thesis submitted in partial fulfilment of the requirements for the degree of Doctor of Philosophy in Engineering

WMG, University of Warwick

May 2017

Table of Contents

Acknowledgements

I would like to thank the advisors of my PhD research, Dr. Chaoying Wan and Prof. David M. Haddleton. I am grateful to them for giving me the opportunity to conduct this research in the University of Warwick. I would also like to acknowledge the WMG Research Funding for the financial support.

A considerable initial motivation to perform a research study in phosphazenes is dedicated to Roberto Milani. I will always be grateful to him for sharing the experience he gained during his research in phosphazenes.

During these 3.5 years, a number of people contributed to the efforts of this research either by providing technical support or sharing their knowledge through discussions. I would like to thank Dr. Stefania Ferrari who contributed on writing two papers with me and also provided valuable assistance in the battery lab. A huge "Thank you" goes to Dr. Paul Wilson for his valuable assistance all these years. Our discussions, especially on the final stage of my PhD, had a huge impact on the analysis of the results in Chapters 2 & 3. Enormous thanks goes to Dr. Marc Walker for training, teaching and assist me in the XPS analysis, which is one of the most valuable knowledge I gained through my PhD.

The SEM imaging was an operation on weekly basis and Dr. Geoff West by keeping the "babies" happy, made me happy too. Thank you Geoff.

I would like to thank Dr. Joaquin Sanchis-Martinez -my friend Ximo- for his continuous support and especially for the discussions we had over the issues I faced with the analysis in Chapter 3. ¡ Muchas gracias mi amigo!

Also, I must express my gratitude to Assoc. Prof. Giannis S. Papaefstathiou (Dept. of Chemistry, University of Athens, Greece) for the discussions we had which helped me to better understand some concepts of organic chemistry.

George S. Pappas

My friends Dr. Panos Efthimiadis, Dr. Yannis Papadimitriou supported me many times during the demanding stage of writing the thesis and thinking… of my future! Great times guys! Thank you!

I am grateful to Karla -*"The boss"* - Monterrubio for the support and help on the final stages of writing the thesis. Special thanks to Victoria Pereyra - Iraola for the long and funny nights we spent in the Library writing our thesis the last months. I should also acknowledge her contribution in the composition of some parts of this thesis.

Of course, my greatest gratitude goes to my family for their support and patience all these years… since I was born!

Declaration

Experimental work contained within this thesis is original research carried out by the author, unless otherwise stated, in the International Institute for Nanocomposites Manufacturing (IINM), Warwick Manufacturing Group at the University of Warwick, between December 2013 and May 2016. No material contained herein has been submitted for any other degree, or at any other institution.

Results from other authors are referenced in the usual manner throughout the text.

Date: 31st of May 2017

Signed: Georgios Pappas (SN: 1390115)

List of publications

The publications related to the presented thesis are listed below:

1. Pappas G.S, Ferrari S, Wan C. Recent advances in graphene-based materials for lithium batteries. *Current Organic Chemistry* 2015, **19**(18)**:** 1838-1849.

2. Pappas G.S, Ferrari S, Huang X, Bhagat R, Haddleton D, Wan C. Heteroatom Doped-Carbon Nanospheres as Anodes in Lithium Ion Batteries. *Materials* 2016, **9**(1)**:** 35.

3. Pappas G.S, Wan C, Bowen C, Haddleton David M, Huang X. Functionalization of BaTiO$_3$ nanoparticles with electron insulating and conducting organophosphazene-based hybrid materials. *RSC Adv* 2017, **7**(32)**:** 19674-19683.

Abstract

The developments in energy storage systems in the last two decades, resulted in a series of interdependent events in consumer's habits; the modern commercial devices became thinner, smaller and lighter with enhanced portability. Hence, the way in which users relate with electronic gadgets changed and this has derived in the invention of new applications. These developments within the electronic industry have demanded new materials and formulations in order to fulfil the growing requirements of new technologies and, especially in the last years, the electrification of transport.

The need to pursue research to develop safe, environmental friendly, recyclable and low-cost materials is, in this context, a pressing issue. While hybrid materials offer unique properties for the development of advanced energy storage systems such as hydrogen and solar cells, lithium-ion batteries and capacitors, these are usually expensive and entail serious environmental hazards. This thesis advances scientific analyses on the cyclomatrix organophosphazenes synthesis that could be applied for the development of low-cost and eco-friendly industrial processes for the production of electrode materials.

In Chapter 1, a brief introduction on the fundamental chemistry of phosphazene materials is presented followed by an outline description of the Li-ion batteries and dielectric materials and their current trends for the improvement of their efficiency. The research aim and objectives of this thesis are then presented.

Chapter 2 deals with the synthesis of cyclomatrix organophosphazene (OPZ) nanospheres. The effects of the solvent, organic base, and organic co-monomer on the morphology of the nanoparticles are studied. The morphology of the nanospheres was highly dependent on the polarity of the solvent, pK_a of the base and solubility of the produced salt during the reaction. A new design for the scale up synthesis of OPZs was developed based on distillation and

reuse of the solvent and organic base. The dependence of the morphology on the polarity of the solvent is further investigated in detail in Chapter 3 where a self-template-direct formation of hollow OPZs is described. The presence of water in the reaction mixture promoted the formation of nanospheres with a single hole on their surface while the reactions at higher water contents resulted in the formation of hollow nanospheres and semi-shells.

The subject of heteroatom-doped carbon nanospheres (CNS) as anode electrodes in Li-ion batteries is described in Chapter 4. A detailed analysis and discussion of the microporous structure and the heteroatom-doping carbon is presented in order to understand the structure-to-electrochemical properties of the CNS as anode materials. The ternary heteroatom doping had significant impact on the microporous structure of the CNS and their electrochemical performance. CNS with high pyridinic-N content and abundant micropores, showed impressive charge/discharge cycling stability for over 1100 cycles, delivering 130 mA h g^{-1}.

The facile OPZ chemistry is further applied in the presence of $BaTiO_3$ nanoparticles in order to produce electron insulating $OPZ@BaTiO_3$ and electron conducting $C@BaTiO_3$ core-shell hybrid nanoparticles. The successful growth of OPZ as a thin layer/coating is based on the substrate-independency of the method. The morphology and structural characteristics of obtained core-shell particles is discussed in detail, along with the results from the impedance spectroscopy characterisation. A stable relative permittivity ($\varepsilon_r \sim 35$) and low dielectric loss over a wide range of frequency was achieved by adjusting the OPZ shell thickness. The initial insulating OPZ shell was transformed to e$^-$ conducting carbon shell, by a pyrolysis step at 700 °C and the resulted $C@BaTiO_3$ showed a relatively high ac conductivity and specific surface area. The research outcome of this project together with suggestions for future directions are summarised in Chapter 6.

List of Figures

List of Schemes

List of Tables

Abbreviations

MeCN	Acetonitrile
MeCN-H_2O	Acetonitrile – water solution
AqPCPBS	hollow PCPBS nanospheres
AqPCPPG	hollow PCPPG
BET	Brunauer-Emmett-Teller
BJH	Barrett-Joyner-Halenda
BPS	4,4-Sulfonyldiphenol
c-AqPCPBS	carbonised hollow PCPBS
CNS	Carbon nanospheres
CNTs	Carbon nanotubes
COFs	Covalent organic frameworks
CV	Cyclic voltammogram
HCCP	Hexachlorocyclotriphosphazene
DCC	Dynamic covalent chemistry
DCM	Dichloromethane
DFT	Density-functional theory
DLS	Dynamic light scattering
DMAP	4-(Dimethylamino) pyridine
DMSO	Dimethyl sulfoxide
EDS	Energy-dispersive X-ray spectroscopy
Eq.	Equivalents
ESS	Energy storage systems
EVs	Electric vehicles
FT-IR	Fourier transform infrared spectroscopy
FWHF	Full width at half maximum
HCCP	Hexachlorotriphosphazene
LIBs	Lithium-ion batteries
Me_6TREN	Tris[2-(dimethylamino)ethyl]amine

MEEP	Poly[bis(2-(2-methoxyethoxy)ethoxy)phosphazene]
MOFs	Metal-organic frameworks
MR	Molar ratio
NLDFT	Nonlocal Density-Functional Theory
NMP	*N*-methyl-2-pyrrolidone
ODA	*4,4*-diaminodiphenyl ether
OPZs	Organophosphazenes
ORR	Oxygen reduction reaction
PCPBS	Poly (cyclotriphosphazene -co- *4,4*-sulfonyl diphenol)
PCPPG	Poly(cyclotriphosphazene-co-phloroglucinol)
PDCP	Poly (dichlorophosphazene)
PG	Phloroglucinol
PMDETA	*N,N,N',N'',N''*-pentamethyldiethylenetriamine
PMMA	Poly (methacrylic acid)
PS	Polystyrene
PVDF	Poly (vinylidene fluoride)
PZM	Melamine-based organophosphazene nanotubes
PZT	Organophosphazene nanotubes
ROP	Ring opening polymerization
SAED	Selected area of diffraction
SEI	Surface electrolyte interface
SEM	Scanning electron microscopy
Et_3N	Triethylamine
$Et_3N \cdot HCl$	Triethylamine hydrochloride
TEM	Transmission electron microscopy
TGA	Thermogravimetric analysis
THF	Tetrahydrofuran
TMEDA	Tetramethylethylenediamine
TPP-$(OH)_4$	Tetrahydroxyphenylporphyrin
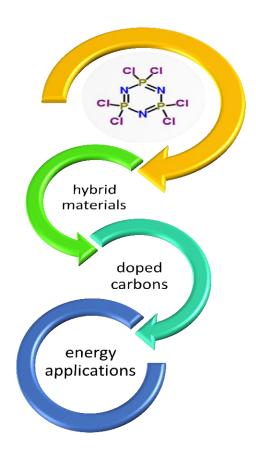
VR	Volume ratio
XPS	X-ray Photoelectron spectroscopy
XRD	X-ray diffraction
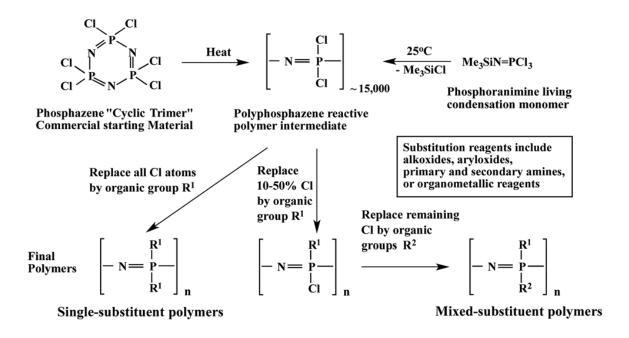
Chapter 1 Introduction

The electric energy storage has become one of the greatest and demanding challenges of our generation. From the miniaturization of portable electronic devices to the long driving range electric vehicles which influence the freedom of movement and hold the hope for an eco-friendly transportation future, the development on Li-ion batteries are of significant importance. Phosphazene chemistry has been contributing to the energy storage development by providing novel organic-inorganic hybrid materials with a broad variety of properties. Nowadays, more than ever, this contribution needs to be further expanded towards a new generation of energy storage systems.

Chapter 1 Introduction

1.1   Polyphosphazenes: A class of real hybrid materials

Polyphosphazenes with more than 700 reported polymers are the most studied member of the inorganic polymers family, which also includes polysiloxanes (silicone) and polysilanes.[1] The term "phosphazenes" refers to a class of hybrid polymers of alternating single and double bonded phosphorus (P) and nitrogen (N) atoms ($-$P$=$N$-$P$=$) with two organic, organometallic or halogen groups (R) bearing on each P atom. The basic compound of this class of materials is the hexachlorocyclotriphosphazene or phosphonitrilic chloride (($NPCl_2)_3$), HCCP), a cyclic form of the ($-$P$=$N$-$P$=$) structure with two chlorine (Cl) atoms attached on each P atom (**Scheme 1.1**). The HCCP was synthesized from ammonium chloride and phosphorous pentachloride in 1834 by Liebig and Wöhler, and in 1897 Stokes attempted to polymerise HCCP at high temperature resulting in a crosslinked and insoluble inorganic elastomer.[2] It was only until 1965 when Harry R. Allcock produced, under controlled synthetic conditions (*in vacuo* at 250 °C), a linear and soluble polydichlorophosphazene (PDCP) polymer of high molecular weight.[3] Since then, an enormous expansion of the produced polyphosphazenes was based on the high temperature ring opening polymerization (ROP) of HCCP followed by the substitution of the Cl atoms by aliphatic or aromatic organic compounds. Other developments include the polymerisation of several types of cyclic phosphazenes homologues (*i.e.*, carbophosphazenes, thiophosphazenes, and metalophosphazenes) in which, the substitution of one P atom enabled the ROP at lower temperatures. Additionally, linear PDCP of relative low polydispersity index ($M_w/M_n \approx 1.8$) can be synthesized at room temperature by the living cationic polymerisation of halogen-rich phosphoranimines of the type X_3P$=$NR (X = halogen; R = alkyl, aryl, silyl).[4] The synthetic methods of polyphosphazenes are well described in a comprehensive review paper by De Jaeger and Gleria[5], as well as, the most recent advances are presented in a tutorial review from Rothemund and Teasdale.[6]

Scheme 1.1 The general synthetic pathways for the synthesis of linear poly (organophosphazenes).[7]

Through the decades the developments in phosphazene chemistry brought to light new phosphazene materials with unique properties, which made them appropriate in several practical applications such as elastomers, permeable membranes, drug delivery systems, and energy storage. In particular, when it comes to fire risk minimization, most of the times someone will find the term "phosphazene" in the material's chemical structure. The most renowned property of phosphazenes is their fire resistivity owing to the P and N atoms' ability to retard the combustion of the organic side groups or the host polymer matrix.[8] As fire retardancy is a crucial parameter for the health and safety regulations in many applications, the literature is vast in this respect and covers a wide range of different structures ranging from linear to matrix-like polymers.[9] For the same reason, a substantial contribution on the phosphazene chemistry was made by the US Army in collaboration with Universities and R&D companies.[10] Other significant applications include the production of high permeability membranes owing to the high rotational ability of the P-N backbone (low T_g, high flexibility).[11, 12] Furthermore, owing to the biodegradability of the phosphazene backbone along with the appropriate biocompatible organic side groups, the polyphosphazenes are

recognised as promising biomaterials for drug delivery systems.[13] Last but not least, polyphosphazenes have been studied in lithium-ion batteries as fire retardants additives in the organic liquid electrolytes and as ion conducting polymer electrolytes/binders, respectively.[14,][15]

Despite the excellent properties of the high MW linear polyorganophosphazenes, their large scale production never reached the success of the carbon-backbone "classic" polymers. The need for high vacuum, temperature and purity of the reactants, greatly increases the complexity and cost for an industrial production. Although some of the methods require only mild conditions, the starting materials in these cases are either very expensive or not commercially available.

1.1.1 Cyclomatrix organophosphazenes

Apart from the linear polyphosphazenes obtained by the ring opening of HCCP, plenty of other phosphazene materials are based on the direct utilization of HCCP in order to afford the so called, cyclolinear[16] and cyclomatrix[17] organophosphazenes. As shown in **Scheme 1.2**, these structures are described by the covalently bonding of the inorganic cyclophosphazene rings through the exocyclic organic functional groups (Y), generating linear oligomers and cross-linked structures. Considerable interest has been also given to organic polymers bearing cyclophosphazenes[18, 19] as side groups of their repeating monomeric units.

Scheme 1.2 The basic structures of **a)** cyclolinear **b)** cyclomatrix and **c)** linear organic polymer bearing cyclic phosphazene as side group. "Y" represents the organic linker.[5]

Compared to linear OPZs, the studies on cyclomatrix OPZs were limited and outdated (1970s), and the relationship between synthesis-morphologies, as well as, the formation mechanism of OPZ based nanomaterials were unreported. The latter observation is mainly assigned to the fact that in the past, the selected reaction conditions and the organic co-linkers resulted in gel-like amorphous materials.[20] A turning point could be placed in 2006-2007, when the first highly cross-linked cyclomatrix OPZs were synthesised in the form of nanofibers[21] and microspheres[22]. These cyclomatrix OPZs - which are the subject of the presented work- are obtained through one-step substitution reaction between HCCP and a multifunctional -OH or -NH$_2$ organic molecule. Up to date, cyclomatrix OPZs range from zero to three dimensional structures and various functionalities have been synthesised and proposed for applications, such as fluorescent sensors, adsorbents, electrolytes and catalysis.[23] The unique chemical structure of the cyclomatrix OPZs has an apparent benefit on their thermal stability, which enabled the production of their carbon-derivatives.[24, 25] A unique property of the carbons produced from cyclomatrix organophosphazenes precursors is their multiple heteroatom-doping. In **Chapter 4**, the importance of heteroatoms in the electrochemical performance of these carbons is discussed. Up to date there are few publications dealing with the application of multiple-heteroatom doped carbons in energy storage systems. Considering the youth of the cyclomatrix OPZs nanomaterials research, further study is needed in order to improve the understanding of the current synthetic methodologies and explore the physicochemical properties both of the OPZs and their carbon derivatives.

1.2 Lithium-ion Batteries

One of the most important and innovative discoveries of the last 400 years, which changed the flow of human history, is undeniably the discovery of electricity. However, the first influential use of electrical energy came with the innovation of the first battery as energy storage system (ESS) by Volta in 1800. Later in 1859, Planté invented the first rechargeable (secondary) battery system, the lead-acid battery, and since then various rechargeable battery systems, such as nickel−cadmium, nickel metal hydride, and lithium ion batteries (LIBs), have serviced humankind for over a century with their use in a huge variety of applications.[26] LIBs which were first introduced in the market by SONY in 1991, represent the current state-of-the-art rechargeable battery technology, and is one of the most important areas for the industry.[27] In 2013, consumers bought five billion Li-ion cells to supply portable electronic devices and electric cars, and it is forecast that the global LIB market will exceed $60 billion by 2020.[28] However, the pathway to success was not easy and the commercialisation of LIBs delayed for almost 20 years, mainly due to the severe safety issues (*i.e.,* thermal runaway, short-circuiting) aroused from the highly reactive metallic lithium anode electrodes used in 1970s. To ameliorate these problems, Yoshino in 1985 used Lithium Cobalt Oxide ($LiCoO_2$) as cathode and carbonaceous fibres as anode materials, while polypropylene carbonate (PC) served as the electrolyte. The day of LIB birth came one year later when Yoshiro's battery successfully passed the safety tests without causing any ignition of the electrolyte.[29]

Owing to its abundance and low production cost along with the availability of compatible electrolytes, graphite became the most commonly used anode material in commercial LIBs. With a theoretical gravimetric capacity of 372 mA h g^{-1} (based on the assumption that one Li ion is coordinated by six C atoms)[30] graphite-based batteries soon became the ultimate choice as power source in small and medium portable electronic devices (mobile phones, laptops, PDAs, electronic hand tools, *etc.*).

Chapter 1 Introduction

In **Figure 1.1** the operation mechanisms of a typical LIB coin cell are presented. The basic components of a coin cell are the positive electrode (cathode) in contact with an aluminum current collector, a negative electrode (anode) in contact with a copper current collector, a porous polymer membrane (allowing Li ions to travel through) separating the two electrodes, and the liquid aprotic electrolyte witch transfers the Li ions between the two electrodes.
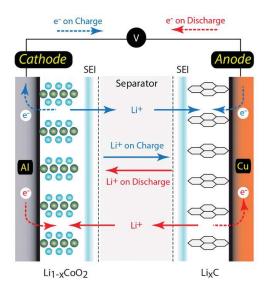
Figure 1.1 Schematic illustration of the operation of a rechargeable LIB with a graphite (Li_xC) anode and $Li_{1-x}CoO_2$ as cathode. The red and blue arrows show the discharging and charging pathways, respectively.[31]

During charging, Li^+ ions are extracted from the cathode (positive electrode) into the electrolyte, diffuse across the porous separator, while electrons (e^-) flow across the external circuit and finally combine with the Li^+ in the anode (negative electrode) where intercalation into the graphitic spacing between the graphene sheets takes place. The general reaction in a metal oxide (MO) cathode is as follows:

$$LiMO_x \underset{discharge}{\overset{charge}{\longrightarrow}} Li_{1-y}MO_x + yLi^+ - ye^- \qquad (Eq. 1.1)$$

During the discharge process the reverse pathway is followed, with Li ions to backfill the empty spaces in the cathode, while on the anode the following reaction takes place:

$$C_n + yLi^+ + ye^- \xrightleftharpoons[\text{discharge}]{\text{charge}} Li_yC_n \qquad \text{(Eq. 1.2)}$$

The overall reaction becomes:

$$LiMO_x + C_n \xrightleftharpoons[\text{discharge}]{\text{charge}} Li_{1-y}MO_x + Li_yC_n \qquad \text{(Eq. 1.3)}$$

These reversible insertion electrochemical reactions are intrinsically simple, resulting in very good reversible capacity and long cycling life. Nonetheless, as the functionalities of the portable electronics become more sophisticated and the demand for electric vehicles and storage of electricity from renewable sources increases, a further increase in energy density is needed. This could be achieved through an increase in the charge storage capacity of the anode and cathode materials and/or an increase in the cell voltage. However, the limited electrochemical-stability window of the currently available liquid electrolytes makes it difficult to increase the cathode operating voltage beyond ~4.3 V. Moreover, the capacities of the current metal oxide cathodes and graphite anodes have already reached their limits.[32] These limitations pushed the scientific community in the research, development, and testing of alternative electrode and electrolyte materials for LIBs, which offer higher capacities and longer cycling stability. The development and commercialization of advanced anode materials (silicon, transition metal oxides and sulphides, various alloys, *etc*.) for Li-ion batteries is at the core of today's efforts.[33, 34] These materials have much higher theoretical capacity (*i.e.,* Li-Si alloy has 4200 mA h g^{-1}) than graphite, but suffer mainly from low electrical conductivity and large volume expansion during lithiation, which lead to poor cycling performance. In the meantime, the "*traditional*" LIBs still hold a prominent position since graphite is the only material to combine low cost, performance and easy processability; three crucial factors for industrial production. However, the most important metric value in electrode materials is the volumetric rather than the gravimetric capacity, and graphite with a

theoretical volumetric capacity of 818 mA h cm^{-3} has failed to satisfy applications where small battery size and weight is important. For this reason, carbon nanotubes (CNTs)[35], graphene oxide[36], carbon fibers[37], fullerenes[38] and carbon nanospheres[39] with higher gravimetric and volumetric capacities than graphite, are some examples of this effort. In particular, disordered non-graphitic carbons have found their excellence as anode materials in novel alkali-metal batteries such as Na-ion[40] (sodium) and K-ion[41] (potassium), where graphite has failed to host these ions due to the small interlayer graphene distance.

The increasing need for environmental friendly transportation is at present the driving force for the design of electric vehicles (EVs) and the need for ESS with energy density comparable to gasoline longer, pushed the scientific community in the search for alternative battery formulations which extended beyond the "conventional" LIBs technology. Lithium-Air (Li-O$_2$)[42] and Lithium-Sulphur (Li-S)[32], having theoretical energy densities of 5000 and 2600 Wh/kg, respectively, are the two major technologies predicted to move forward towards the realisation of single-charge driving distance equal to gasoline. Again, carbon materials are the ultimate choice also for these battery systems while, besides the obvious advantages of the engineered carbons (hierarchically porous, hollow structures, onion-like structures *etc.*), doping of carbon-materials with heteroatoms (N, O, S, B, and P) is believed to continuous boost their research and development for metal-free energy storage and conversion system.[43] The excellent passivating surface electrolyte interface (SEI) films on carbon surfaces and the large accommodation of Li ions into the carbon structures are the *"two wonders* associated with the success story of carbons as anodes*"*, according to Winter, Moeller and Besenhard, who are also sceptical if there will be a third wonder for the lithiated carbons in the future.[44] From the recent developments in heteroatom-doped carbon materials[45-47] the previous question might soon find a clear and strong answer.

Nitrogen-doped carbon surface

hydroxylic oxygen

carbonylic oxygen

pyrodinic nitrogen

quaternary nitrogen

carboxylic oxygen

Strongly-coupled interface

hydrogen ● lithium ● carbon ● nitrogen ● oxygen ● sulfur
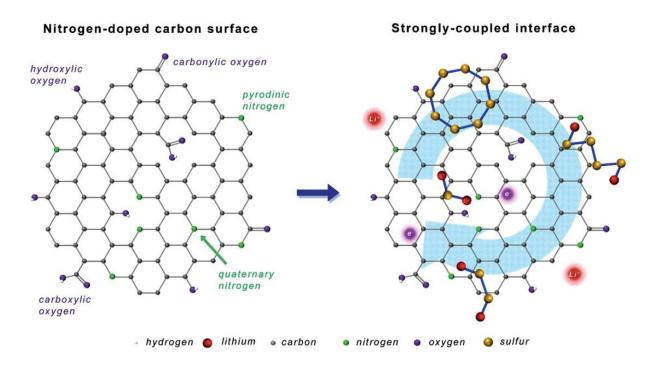
Figure 1.2 N- and O- co-doped CNTs for Li-S batteries [48]
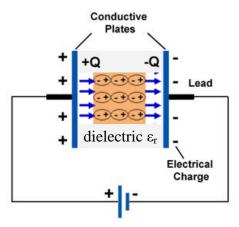
1.2.1 The contribution of phosphazene chemistry to LIBs technology

Phosphazene chemistry has already shown its excellence in LIBs development by providing high ionic conductivity solid polymer electrolytes. Linear poly [bis(2-(2-methoxyethoxy) ethoxy) phosphazene (MEEP)[49] and star-shaped oligo (ethyleneoxy) cyclotriphosphazenes[50] exhibited remarkable electrochemical stability and ionic conductivities of 10^{-4} S cm^{-1} at room temperature. Apart from the profound fire-resistivity, phosphazene significantly contributes to Li$^+$ solvation and conduction through the coordination between N atoms and Li$^+$.[51]

Additionally to the previous, phosphazene chemistry provides the necessary structures for the facile production of heteroatom-doped carbons either by the pyrolysis of cyclomatrix OPZs[52] or HCCP-functionalised graphene oxide.[53] Up to date, OPZs have only been reported as carbon-coatings on silicon-based anodes.[54-56] In **Chapter 4**, a brief review on multi-doped carbons derived from cyclomatrix OPZs is provided along with their utilization in ESS.

1.3   Dielectric materials

Instead of the generation of voltage by chemical reactions in the batteries, the electrical energy storage can also be achieved by the physical separation of the charges. The electrical insulating materials that can be polarized under an externally applied electric field are called "dielectrics" and the dielectric constant or relative permittivity (ε_r) is a measure of this capability. The most known application of dielectrics is as separators in solid-state ceramic capacitors. When connected to a DC electric source (V), a capacitor stores (charged state) negative (-Q) and positive charge (+Q) on its electron conducting plates which are separated by the insulating dielectric material (**Scheme 1.3**). The electric charge (Q) remains stored on the plates even when the voltage is removed. An external short circuit can cause the Q to flow through and result in the discharge of the capacitor.

Scheme 1.3 A simple diagram of a solid-state capacitor showing how the charge is stored.

The capacitance (C) is a measure of the amount of Q that can be stored in a capacitor and it is expressed by the equation[57],

$$C = \frac{Q}{V} \; or \; C = \frac{\varepsilon_0 \varepsilon_r S}{d} \qquad \text{(Eq. 1.4)}$$

where S is the electrode surface area (m^2), d the distance between the plates (m), and ε_0 and ε_r are the vacuum permittivity (8.85x10^{-12} F/m) and separator permittivity, respectively.

Contrary to the battery, the solid-stated capacitor is a short-term energy system of high power density but low energy density, at the time when the modern trend for smaller portable devices and EVs, demands both values to be as high as possible. The equation (Eq. 2.4) indicates that by changing the geometrical characteristics of the electrodes (large S, small d) and utilizing materials of high ε_r would lead to high capacitance C. However, the large S is not considered as an attractive solution for the apparent reasons (large size and weight). Furthermore, the maximum energy density per unit volume (U) is proportional to the square of the breakdown electric field (E$_b$) according to the following equation[58]:

$$U = \frac{1}{2}\varepsilon_0\varepsilon_r E_b^2 \qquad \text{(Eq. 1.5)}$$

The equations of capacitance and energy density enlighten the pathway that is needed to be followed in order to improve the performance of modern capacitors; this is the utilization of thin film materials of high e$_r$ and E$_b$. The scientific and industrial research has been focused on the development of nanocomposites materials composed by nanostructured dielectric ceramics dispersed in a ferroelectric polymer matrix film. Nanocomposites of barium titanate (BaTiO$_3$), a high permittivity (ε_r ~1200) ceramic of the perovskite family, dispersed in poly (vinylidene fluoride) (PVDF), a ferroelectric polymer of high E$_b$ (590 MV m^{-1}), have been extensively studied for the above propose.[59] Consequently, the polymer-based dielectrics exhibit high energy densities and at the same time offer easier mechanical processing and fabrication which nowadays has extended even to 3D-printng.[60] In order to achieve these targets an intrinsic problem needed a solution. The high fluorine content of PVDF, makes it immiscible with most of the organic and inorganic materials, due to the very low surface

energy. Therefore, the surface chemical treatment of the inorganic filler is necessary in order enhance the compatibilisation, thus the homogeneous dispersity in the matrix.[61]

For this purpose, organophosphazene chemistry can be a facile synthetic tool for the fabrication of core-shell nanostructures. A simple and quantitative nucleophilic substitution reaction between HCCP and *4,4'*-sulfonyldiphenol has been already utilized in order to prepare OPZ-coated substrates of various morphologies and surface functionalities. Some characteristic examples include: superparamagnetic Fe_3O_4 nanoparticles[62], CNTs[63], zirconium phosphate particles[64] and microscale polystyrene honeycomb films[65]. The synthetic nature of "independent-to-substrate" of the organophosphazene chemistry greatly favours its broad applicability over other coating methods.

1.4   Scope of the project

The aim of the thesis is to explore and develop the chemistry of cyclomatrix organophosphazene materials for the synthesis of hybrid nanospheres and their heteroatom-doped carbon derivatives, and investigate their electrochemical properties for electric energy storage systems.

Briefly, the study of the reaction mechanism for the formation of cyclomatrix OPZs was based on the synthesis of poly (cyclotriphosphazene-*co*-Bisphenol S) (PC**PBS**) nanospheres, under various reaction conditions. The reaction mechanism was discussed through the characterisation of the structure evolution and the physicochemical properties (**Chapters 2** & **3**). Moreover, the study was extended to the production and characterisation of multi-heteroatom-doped carbon nanospheres (**Chapter 4**), derived from a high temperature treatment of the PC**PBS** nanospheres synthesised in **Chapter 2**. The intrinsic hybrid nature of OPZ materials makes them perfect candidates for the production of multi-doped carbons in

one step synthesis. Until now, the knowledge on doped-carbons is limited to single or dual heteroatom doping while P-doped carbons are still rarely reported. Moreover, the electrochemical properties of the CNS as anodes in LIBs were explored for the first time and the results provided useful information for energy storage applications.

The same organophosphazene formulation was also extended for the synthesis of OPZ@BaTiO$_3$ core-shell particles as dielectric materials (**Chapter 5**). The inexpensive and facile organophosphazene chemistry is advantageous over other methods for the functionalisation of BaTiO$_3$ nanoparticles. Moreover, the conversion of the OPZ shell to a heteroatom-doped carbon shell enabled the production of both electron insulating and conducting nanomaterials from one batch synthesis. The outline and the major tasks in each experimental Chapter are shown in **Figure 1.3**.

Chapter 3
- Effect of water
- In situ hollow OPZs
- Contribution in OPZ chemistry

Chapter 2 Analysis of the OPZ synthesis mechanism

Chapter 4
- Production of carbon nanospheres from OPZs
- Analysis of the strucrure
- Electrochemical performance

Chapter 5
- Production of hybrid core-shell OPZ particles
- Evaluation of dielectric properties
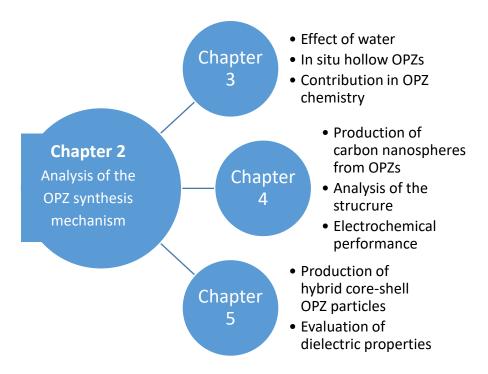
Figure 1.3 Diagram showing the outline of the thesis structure.

1.5 References

1.   J. E. Mark, H. R. Allcock and R. West, *Inorganic Polymers*, Oxford University Press, 2005.

2.   R. A. Shaw, B. W. Fitzsimmons and B. C. Smith, *Chemical reviews*, 1962, **62**, 247-281.

3.   H. R. Allcock and R. L. Kugel, *Journal of the American Chemical Society*, 1965, **87**, 4216-4217.

4.   H. R. Allcock, C. A. Crane, C. T. Morrissey, J. M. Nelson, S. D. Reeves, C. H. Honeyman and I. Manners, *Macromolecules*, 1996, **29**, 7740-7747.

5.   R. G. De Jaeger, M., *Progress in Polymer Science*, 1998, **23**, 179-276.

6.   S. Rothemund and I. Teasdale, *Chemical Society reviews*, 2016, **45**, 5200-5215.

7.   H. R. Allcock, *Dalton Trans*, 2016, **45**, 1856-1862.

8.   H. R. Allcock, *Journal of Inorganic and Organometallic Polymers and Materials*, 2007, **17**, 349-359.

9.   C. W. Allen, *Journal of Fire Sciences*, 1993, **11**, 320-328.

10.   R. E. Singler, *Journal of Inorganic and Organometallic Polymers and Materials*, 2007, **16**, 307-309.

11.   Z. Yang, W. Zhang, J. Li and J. Chen, *Separation and Purification Technology*, 2012, **93**, 15-24.

12.   R. Gutru, S. G. Peera, S. D. Bhat and A. K. Sahu, *Solid State Ionics*, 2016, **296**, 127-136.

13.   M. Akram, L. Wang, H. Yu, W. A. Amer, H. Khalid, N. M. Abbasi, Y. Chen, A. Zain ul, M. Saleem and R. Tong, *Progress in Polymer Science*, 2014, **39**, 1987-2009.

14.   H. W. Rollins, M. K. Harrup, E. J. Dufek, D. K. Jamison, S. V. Sazhin, K. L. Gering and D. L. Daubaras, *Journal of Power Sources*, 2014, **263**, 66-74.

15.   E. J. Dufek, M. L. Stone, D. K. Jamison, F. F. Stewart, K. L. Gering, L. M. Petkovic, A. D. Wilson, M. K. Harrup and H. W. Rollins, *Journal of Power Sources*, 2014, **267**, 347-355.

16.   H. R. Allcock, E. C. Kellam and M. A. Hofmann, *Macromolecules*, 2001, **34**, 5140-5146.

17.   T. Zhang, Q. Cai, D.-Z. Wu and R.-G. Jin, *Journal of Applied Polymer Science*, 2005, **95**, 880-889.

18.   H. R. Allcock, T. J. Hartle, J. P. Taylor and N. J. Sunderland, *Macromolecules*, 2001, **34**, 3896-3904.

19.   R. F. Hayes and C. W. Allen, *Journal of Inorganic and Organometallic Polymers and Materials*, 2010, **20**, 528-533.

20.   T. A. Luther, F. F. Stewart, R. P. Lash, J. E. Wey and M. K. Harrup, *Journal of Applied Polymer Science*, 2001, **82**, 3439-3446.

21.   Z. Lu, Y. Weizhong, P. Yang, T. Xiaozhen and H. Xiaobin, *Polymer International*, 2006, **55**, 1357-1360.

22.   L. Zhu, Y. Zhu, Y. Pan, Y. Huang, X. Huang and X. Tang, *Macromolecular Reaction Engineering*, 2007, **1**, 45-52.

23.   C. Wan and X. Huang, *Materials Today Communications*, 2017, **11**, 38-60.

24.   J. Fu, Z. Chen, Q. Xu, J. Chen, X. Huang and X. Tang, *Carbon*, 2011, **49**, 1037-1039.

25.   J. Fu, Q. Xu, J. Chen, Z. Chen, X. Huang and X. Tang, *Chemical communications*, 2010, **46**, 6563-6565.

26.   B. Scrosati, *Journal of Solid State Electrochemistry*, 2011, **15**, 1623-1630.

27.   G. E. Blomgren, *Journal of The Electrochemical Society*, 2017, **164**, A5019-A5025.

28.   R. Van Noorden, *Nature*, 2014, **507**, 26-28.

29.   A. Yoshino, *Angewandte Chemie*, 2012, **51**, 5798-5800.

30.   R. Fong, U. von Sacken and J. R. Dahn, *Journal of The Electrochemical Society*, 1990, **137**, 2009-2013.

31.   B. J. Landi, M. J. Ganter, C. D. Cress, R. A. DiLeo and R. P. Raffaelle, *Energy & Environmental Science*, 2009, **2**, 638.

32.   A. Manthiram, Y. Fu, S. H. Chung, C. Zu and Y. S. Su, *Chemical reviews*, 2014, **114**, 11751-11787.

33.	M. T. McDowell, S. W. Lee, W. D. Nix and Y. Cui, *Adv Mater*, 2013, **25**, 4966-4985.

34.	X. Xu, W. Liu, Y. Kim and J. Cho, *Nano Today*, 2014, **9**, 604-630.

35.	L. Li, H. Yang, D. Zhou and Y. Zhou, *Journal of Nanomaterials*, 2014, **2014**, 1-8.

36.	S. Wu, R. Xu, M. Lu, R. Ge, J. Iocozzia, C. Han, B. Jiang and Z. Lin, *Advanced Energy Materials*, 2015, **5**, 1500400.

37.	M. Endo, Y. A. Kim, T. Hayashi, K. Nishimura, T. Matusita, K. Miyashita and M. S. Dresselhaus, *Carbon*, 2001, **39**, 1287-1297.

38.	R. O. Loutfy and S. Katagiri, in *Perspectives of Fullerene Nanotechnology*, ed. E. Ōsawa, Springer Netherlands, Dordrecht, 2002, DOI: 10.1007/0-306-47621-5_32, pp. 357-367.

39.	A. D. Roberts, X. Li and H. Zhang, *Chemical Society reviews*, 2014, **43**, 4341-4356.

40.	B. Zhang, C. M. Ghimbeu, C. Laberty, C. Vix-Guterl and J.-M. Tarascon, *Advanced Energy Materials*, 2016, **6**, 1501588.

41.	Z. Jian, W. Luo and X. Ji, *J Am Chem Soc*, 2015, **137**, 11566-11569.

42.	Y. Shao, F. Ding, J. Xiao, J. Zhang, W. Xu, S. Park, J.-G. Zhang, Y. Wang and J. Liu, *Advanced Functional Materials*, 2013, **23**, 987-1004.

43.	T. Asefa and X. Huang, *Chemistry*, 2017, DOI: 10.1002/chem.201700439, n/a-n/a.

44.	M. Winter, K.-C. Moeller and J. O. Besenhard, in *Lithium Batteries: Science and Technology*, eds. G.-A. Nazri and G. Pistoia, Springer US, Boston, MA, 2003, DOI: 10.1007/978-0-387-92675-9_5, pp. 145-194.

45.	J. Zhang, Z. Xia and L. Dai, *Sci Adv*, 2015, **1**, e1500564.

46.	K. Gong, F. Du, Z. Xia, M. Durstock and L. Dai, *Science*, 2009, **323**, 760-764.

47.	L. Dai, *Nature Energy*, 2016, **1**, 16041.

48.	H.-J. Peng, T.-Z. Hou, Q. Zhang, J.-Q. Huang, X.-B. Cheng, M.-Q. Guo, Z. Yuan, L.-Y. He and F. Wei, *Advanced Materials Interfaces*, 2014, **1**, 1400227.

49.	S. Jankowsky, M. M. Hiller, R. Stolina and H. D. Wiemhöfer, *Journal of Power Sources*, 2015, **273**, 574-579.

50.   D. He, S. Y. Cho, D. W. Kim, C. Lee and Y. Kang, *Macromolecules*, 2012, **45**, 7931-7938.

51.   L. Long, S. Wang, M. Xiao and Y. Meng, *J. Mater. Chem. A*, 2016, **4**, 10038-10069.

52.   K. Chen, X. Huang, C. Wan and H. Liu, *Materials Chemistry and Physics*, 2015, **164**, 85-90.

53.   L. Dong, C. Hu, X. Huang, N. Chen and L. Qu, *Chem Asian J*, 2015, **10**, 2609-2614.

54.   C. Zhang, A. Song, P. Yuan, Q. Wang, P. Wang, S. Zhang, G. Cao and J. H. Hu, *Materials Letters*, 2016, **171**, 63-67.

55.   L. Xue, G. Xu, Y. Li, S. Li, K. Fu, Q. Shi and X. Zhang, *ACS applied materials & interfaces*, 2013, **5**, 21-25.

56.   P. Gao, J. Fu, J. Yang, R. Lv, J. Wang, Y. Nuli and X. Tang, *Physical chemistry chemical physics : PCCP*, 2009, **11**, 11101-11105.

57.   G. M. Garner and K. J. Humphrey, in *Special Polymers for Electronics and Optoelectronics*, eds. J. A. Chilton and M. T. Goosey, Springer Netherlands, Dordrecht, 1995, DOI: 10.1007/978-94-011-0569-9_5, pp. 186-220.

58.   A. Chauhan, S. Patel, R. Vaish and C. Bowen, *Materials*, 2015, **8**, 8009-8031.

59.   P. Barber, S. Balasubramanian, Y. Anguchamy, S. Gong, A. Wibowo, H. Gao, H. Ploehn and H.-C. Zur Loye, *Materials*, 2009, **2**, 1697.

60.   H. Kim, T. Fernando, M. Li, Y. Lin and T.-L. B. Tseng, *Journal of Composite Materials*, 2017, **0**, 002199831770470.

61.   J. Li, J. Claude, L. E. Norena-Franco, S. I. Seok and Q. Wang, *Chemistry of Materials*, 2008, **20**, 6304-6306.

62.   J. Zhou, L. Meng, Q. Lu, J. Fu and X. Huang, *Chemical communications*, 2009, DOI: 10.1039/b914394g, 6370-6372.

63.   J. Fu, X. Huang, Y. Huang, J. Zhang and X. Tang, *Chemical communications*, 2009, DOI: 10.1039/b818071g, 1049-1051.

64.   L. Xu, C. Lei, R. Xu, X. Zhang and F. Zhang, *RSC Adv.*, 2016, **6**, 77545-77552.

65.   S. Chen, X. Lu, Z. Huang and Q. Lu, *Chemical communications*, 2015, **51**, 5698-5701.

66.   V. Kulichikhin, A. Semakov, E. Frenkin, A. Shabeko and D. Tur, *Polymer Science Series B*, 2015, **57**, 687-701.

Chapter 2 Synthesis and characterization of cyclomatrix

organophosphazene nanospheres

In this Chapter the synthesis and characterisation of cyclomatrix OPZ nanospheres is presented. The morphological and chemical structure characterisation set up the fundamental understanding for the materials presented in the subsequent Chapters. Therefore, a detailed description of the substitution reaction between the cyclic hexachlorophosphazene and a bi-functional organic co-linker is given. Factors such as the geometry and acidity of the nucleophile, the polarity of the solvent and the basicity of the organic base proved to have a significant and combined impact on the production of cyclomatrix OPZs. This result is shown through the correlation between the reaction conditions and the morphological diversity of the obtained OPZs nanospheres.

2.1 Introduction

2.1.1 Hybrid nanoparticles strategies

The synthetic methods for the formation of spherical particles, organic, inorganic or hybrid, relies on the chemical nature of the precursors and reaction conditions, which directly determine the structure and properties of the final products. The applications of nanoparticles had awaken human's research interest from the ancient Roman era already[1] and the development is perpetual since then. The range of materials used for the synthesis of nanoparticles has become extremely wide owing to the modern methods of synthesis and characterisation. The synthetic methods of nanoparticles are divided into two categories; the top-down (*e.g.* ball milling[2], attrition[3]) and the bottom-up methods, and the latter has attracted more attention due to the facile control over the structure, morphology and chemical composition of the nanoparticles. The bottom-up methods can be applied via the sol-gel chemistry (SiO_2[4], TiO_2[5]), solvothermal processes (Fe_3O_4[6], zeolite[7]), emulsion polymerisation (PS, PMAA, *etc.*[8]), pyrolysis[9] and gas condensation[10]. While the top-down methods mainly produce inorganic nanoparticles of single chemical composition, the bottom-up methods can additionally produce organic/inorganic nanoparticles of various designs and chemical compositions, materials known as "hybrid nanoparticles". The term "hybrid" refers to structures of well distinguished organic and inorganic parts such as the core-shell nanostructures. Depending on the fabrication approach the hybrid nanoparticles structures can vary from inorganic-core/organic-shell and *vice versa*, polymer-core and *in situ* formation of inorganic nanoparticle seeds, and *in situ* simultaneously synthesis and combination of the organic and inorganic parts.[11] The strategies are illustrated in **Figure 2.1**.
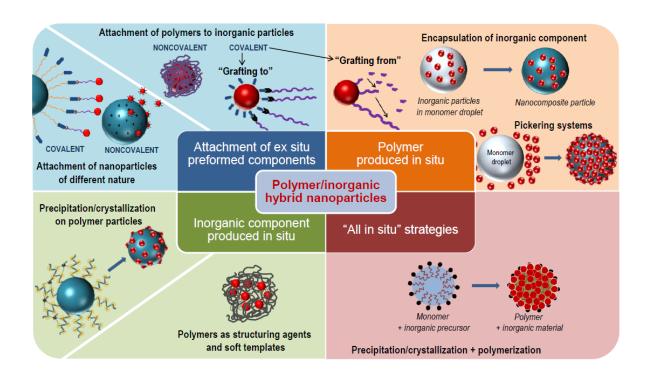
Figure 2.1. Methods for the production of hybrid nanostructures. [11]

2.1.2 Cyclomatrix organophosphazene nanostructures

Cyclomatrix organophosphazene 3D nanostructures (OPZs) are the group of hybrid materials composed by organic molecules (organic linker) covalently bonded to the cyclic trimer of HCCP (inorganic linker) in a cross-linked configuration. The molecule-level size of the building block units (linkers) places these materials in the boundaries of the "mixed organic/inorganic materials" class, where the well confined size of the inorganic/organic parts is in the nanometre scale. A more appropriate classification of the OPZs would place them in the family of covalent organic frameworks (COFs) materials, with the difference that the synthesis of OPZs is not driven by the dynamic covalent chemistry (DCC) rules of the COFs[12], thus most of the OPZs lack of crystallinity and "framework" structure, so as intrinsic microporosity. However, this is entrusted to the judgment of the reader. An example for the synthesis of OPZ nanospheres and the particle formation mechanism is presented in **Scheme 2.1**. An initial reaction between HCCP and *4,4'*-sulphonyl diphenol (BPS, Bisphenol S) in the

presence of triethylamine (Et₃N), generates oligomeric species and hydrogen chloride (HCl) with the latter to be trapped by Et₃N forming to afford Et₃N·HCl. The formation of the primary nucleus particles proceeds through the aggregation of the oligomeric species. The high free energy of these nuclei is minimized by their aggregation in order to form stable particles. Once the stable particles are generated, they continue to grow in size by absorbing oligomeric species or unreacted monomers from the solution. Finally, OPZ nanospheres, bearing numerous surface-OH groups, are precipitated. In this concept and by adjusting the synthesis parameters (solvent, monomer consecrations, molar ratios, co-linker structure), various structures ranging from nanometres to micrometres size bearing various surface functional groups can be obtained.

Scheme 2.1 General mechanism of OPZ formation.[13]

The last decade, via the nucleophilic substitution of HCCP the production of cyclomatrix organophosphazenes of spherical, tubular and sheet-like morphologies, has been steadily growing and a list of the reported nanostructures is presented in **Table 2.1**. In the majority of the published reports, the reaction takes place under sonication conditions for several hours and exclusively in the presence of excess Et₃N, as the "*acid trap*". Furthermore, the majority of the selected organic co-linkers are bi- or tri-functional aromatic compounds of various structures and functional groups. Only recently, the above method was extended to non-

aromatic building blocks with the synthesis of polyamine-, amino acid- and cyclamine-based

OPZs nanospheres[14,15,16] opening the way for the production of new OPZ materials.

Table 2.1. Summary of different co-monomers and obtained morphologies of cyclomatrix OPZs.
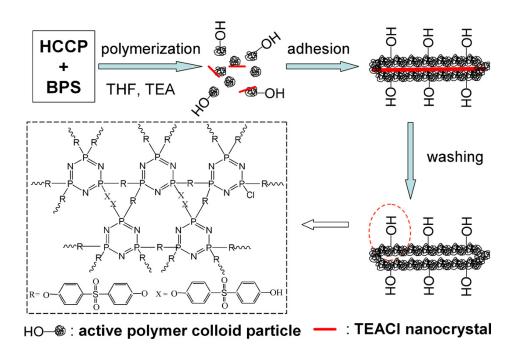
Co-monomer	Conditions	Morphology
4,4'-(hexafluoroisopropylidene) diphenol (BPAF)	MeCN/Et$_3$N/US 5h @50°C	Nanospheres ~500 nm [17]
3,5-ditrifluoromethyl)phenyl hydroquinone	MeCN/Et$_3$N/US 3h @RT	Submicron spheres in the range 600-950 nm depending the ultrasonic power and/or HCCP concentration [18]
2,2'-bis(trifluoromethyl)-4,4'-diaminodiphenyl ether (6FODA)	MeCN/Et$_3$N/US 8h@60°C	Hydrophophic micropsheres ~ 0.5-3μm [19]
4,4'-Sulfonyldiphenol (BPS)	THF/Et$_3$N/US 3h	Nanotubes ø 30-60 nm, L=1-2 μm [20]
BPS	Acetone/Et$_3$N/US 3h@R.T	Microspheres ~1.2 μm [21]
BPS	Acetone/Et$_3$N/US 3h	Fibres ø 20-50 nm, L>500 nm [22]
BPS	Acetone-Toluene/Et$_3$N/US 48h@RT	Fibres or submicron spheres depending the solvent mixture [23]
4,4'-oxidianiline (ODA)	MeCN/Et$_3$N/US 4h@40°C	Microspheres 0.5-2.5 μm depending on the HCCP:ODA ratio [24]
1,3,5-trihydroxybenzene (Phloroglucinol)	MeCN/Et$_3$N/US 2h@30°C	Microspheres 0.6-1.1 μm [25]
4,4'-diaminobiphenyl (benzidine)	MeCN/Et$_3$N/US 48h@ 45°C darkness	Microspheres ~ 2.3 μm [26]
Curcumin	MeCN/Et$_3$N/US 7h@ 40°C	Microspheres ~ 1 μm [27]

Table 2.1 (Continued)

Co-monomer	Conditions	Morphology
melamine	DMF/Et$_3$N/US 48h	Micro-spherical grumbled sheets 1-2 µm [28]
melamine	DMSO/ stirring 48h@180°C	Porous frameworks with high H$_2$ uptake ability [29]
1,3,5-tri(4-hydroxyphenyl) benzene	MeCN/Et$_3$N/US 3h@40°C	Microspheres 0.5-1.0 µm depending the HCCP conc. [30]
4-acetamidophenol	MeCN/Et$_3$N/static 25°C	High dispersity nanospheres < 200 nm [31]
4',5'-Dibromofluorescein (DBF)	MeCN/Et$_3$N/US 3h	fluorescent nanospheres ~ 330 nm [32]
trimethoprime (TMP)	MeCN/US 4h@40°C	Microspheres 0.5-1.0 µm depending the HCCP:TMP [33]
5,10,15,20-tetrakis(4-hydroxyphenyl) porphyrine ((TPP-OH)$_4$)	MeCN or acetone/Et$_3$N/US 0.5-18 h	hollow (250 nm) or solid (670 nm) submicron fluorescent spheres [34]
p-phenylenediamine	THF/hydrothermal conditions @120 °C	highly microporous COFs [35]
3,3-diaminobenzidine (DAB)	Dimethyl sulfoxide (DMSO)	hierarchically porous COFs [36]

As it can be seen from the table above, not only the organic block but also the type of the solvent plays an essential role on the morphology of the OPZs. Acetonitrile (CH$_3$CN, MeCN) is the most often solvent for the synthesis nanospheres, while nanotubes are formed when THF is used. This morphological diversity is attributed to an *in situ* self-templated mechanism due to the low solubility of the Et$_3$N·HCl by-product which exists as rod-like crystals in low polarity solvents. As the reaction between HCCP and BPS proceeds, oligomers and nuclei are absorbed on the Et$_3$N·HCl crystals surface where the growth takes place. This leads to the formation of OPZ nanofibers and a subsequent removal of the Et$_3$N·HCl by washing with water, results in the nanotube structure as shown in **Scheme**

2.2. On the contrary, the high solubility of Et₃N·HCl in MeCN, prevents the formation of crystals, therefore the primary formed OPZ oligomers aggregate with each other in order to minimize their surface energy resulting to solid spherical particles.

Scheme 2.2 *In situ* template method for the synthesis of the OPZs nanotubes in THF.[37]

The synthesis of cross-linked cyclomatrix organophosphazenes (OPZs) has proved to be a facile method to fabricate the precursors for N, P and S co-doped carbon nanospheres and nanotubes.[38] [39] The unique chemical and textural structures of these materials, along with the cost effective and mild synthetic conditions, are the major characteristics that urged their study as potential materials in electric energy storage devices. It is noteworthy that the knowledge around double or ternary heteroatom-doped carbons is still limited and the effect of the heteroatoms on the electrochemical performance is under investigation.

2.2   Aim of the Chapter

This Chapter describes the effect of the solvents and organic bases on the morphology evolution of cyclomatrix OPZ nanospheres based on HCCP and Bisphenol S. A detailed description of the reaction mechanism is proposed and discussed in detail in order to provide a fundamental understanding of the synthetic chemistry of OPZs, which has not been clear so far. Apart from the morphological characterisation of the OPZs, a comprehensive analysis with FT-IR, TGA and XPS is given in order to illustrate the relationship of structure and properties of the nanomaterials, which were also lack of study in the previous literature. The clarification of the reaction and the facile synthesis of OPZs helped to develop a scale-up fabrication method, which provides a practical database and guidance for industrial production of OPZ –based materials. Additionally, the establishment of the current organophosphazene chemistry fundamentals is crucial for the explanation and understanding of the content of **Chapter 3** as well as for the materials synthesis of **Chapters 4** and **5**.

2.3   Experimental

2.3.1   Materials

Hexachlorocyclotriphosphazene (HCCP, Aldrich), *4,4'*-sulphonildiphenol (BPS, Sigma), triethylamine (Et$_3$N, Fisher), *N,N,N',N'',N''*-pentamethyldiethylenetriamine (PMDETA, Aldrich), Tetramethylethylenediamine (TMEDA, Aldrich), 4-(Dimethylamino) pyridine (DMAP, Sigma), acetonitrile (Acros), THF (Acros), acetone (Acros), *1,4*-dioxane (Sigma), dichloromethane (DCM, Acros) and dimethyl sulfoxide (DMSO, Fisher) were used as received. Tris[2-(dimethylamino)ethyl]amine (Me$_6$TREN) was synthesized according to a previously reported protocol.[40]

2.3.2 Characterization

Field emission gun-scanning electron microscopy (FEG-SEM) was performed on a Zeiss SIGMA SEM operated at 10kV. Gold/Palladium (AuPd) sputtering was applied to the samples before observation. The carbonised samples did not require any preparation due to their high electrical conductivity. FT-IR spectra were collected in the range 4000-500 cm^{-1} on a Brucker VECTOR-22 FT-IR spectrometer equipped with an attenuated total reflection (ATR) accessory (Gold Gate series). Thermogravimetric analysis curves were obtained with a Mettler Toledo instrument in the temperature range 25 - 1000 °C at a heating rate of 10 °C min^{-1} under gas N_2 flow (80 mL min^{-1}). X-ray Photoelectron spectroscopy (XPS) characterization was carried out with a Kratos Axis Ultra DLD spectrometer using monochromatic Al Kα source (hv = 1486.6 eV). Survey spectra were collected with pass energy of 160 eV over a binding energy (BE) range of 1200 - 0 eV. Core-level scans were obtained using 20 eV pass energy (resolution approximately 0.4 eV) and an analysis area of ~300 × 700 μm. The spectrometer was calibrated using the Fermi edge position of a polycrystalline Ag sample immediately prior to the experiments reported below. Peak fitting process was performed with the CasaXPS software using mixed Gaussian-Lorentzian (Voigt) line shapes and Shirley backgrounds.

2.3.3 Synthesis of poly (cyclophosphazene-*co*-Bisphenol S) nanospheres (PCPBS)

For the morphological study and structural analysis, hybrid nanospheres of poly (cyclophosphazene -co- Bisphenol S) (PCP**BS**) were prepared in a small scale, under sonication conditions. The general procedure is described as follows: In a 25 mL glass vial, of 1 eq. of HCCP (17 mg, 4.9×10^{-5} mol) and 3.5 eq of BPS (42.5 mg, 1.7×10^{-4} mol) were dissolved in 15 mL of MeCN, under sonication (80 W, 37 kHz). After complete dissolution of the compounds, Et_3N (0.4 mL, 3.9×10^{-3} mol) were added at once under continuous sonication. The solution became turbid within 10 seconds and the reaction left under

sonication for 40 min. The temperature increased from 20-30 °C during the reaction time due to the sonication energy. The PCP**BS** nanospheres were collected by centrifugation (8000 rpm, 10 min), washed twice with acetone and once with a 1:1 volume mixture of acetone/water, and finally dried in a vacuum oven at 50 °C for 24 hours. In the same manner, experiments with various BP**S**/HCC**P** molar ratio (MR$_{S:P}$), solvent and base type, were performed and the conditions are listed in **Table 2.2**.
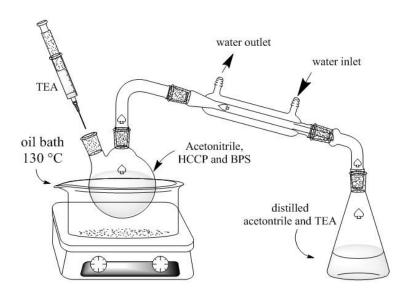
Table 2.2 Reaction conditions for the synthesis of PCP**BS** nanospheres.

EXP.	Sample	BPS (mol) × 10^{-5}	MR$_{S:P}$	Solvent	Base	Size (nm)	Yield %
1	PCP**BS**-1	4.9	1	MeCN	Et$_3$N	-	-
2	PCP**BS**-2	9.8	2	MeCN	Et$_3$N	390 ± 15	25
3	PCP**BS**-3.5	17.2	3.5	MeCN	Et$_3$N	190 ± 25	78
4	PCP**BS**-5	24.5	5	MeCN	Et$_3$N	240 ± 27	82
5	PCP**BS**-6	29.4	6	MeCN	Et$_3$N	220 ± 37	71
6	PCP**BS**-1	4.9	1	MeCN	Et$_3$N	520 ± 70	-
7	PCP**BS**-1	4.9	1	MeCN	Et$_3$N	700 ± 60	-
8	PCP**BS**-3.5	17.2	3.5	acetone	Et$_3$N	900 ± 50	53
9	PCP**BS**-3.5	17.2	3.5	DCM	Et$_3$N	265 ± 60	19
10	PCP**BS**-3.5	17.2	3.5	dioxane	Et$_3$N	2475±245	29
11	PCP**BS**-3.5	17.2	3.5	DMSO	Et$_3$N	-	-
12	PCP**BS**-3.5	17.2	3.5	MeCN	TMEDA	340 ± 70	77
13	PCP**BS**-3.5	17.2	3.5	MeCN	PMDETA	240 ± 25	79
14	PCP**BS**-3.5	17.2	3.5	MeCN	DMAP	255 ± 70	76
15	PCP**BS**-3.5	17.2	3.5	MeCN	Me$_6$TREN	300 ± 45	78
16	PCP**BS**-3.5	17.2	3.5	THF	PMEDTA	8800±1100	60

2.3.4 Synthesis of PCPBS nanospheres under distillation precipitation conditions (scale-up)

In a 500 mL RBF, 2.5×10^{-3} mol of HCCP and 8.8×10^{-3} moles of BPS were dissolved in 430 mL of MeCN under sonication. The flask was transferred in an oil bath placed on a magnetic hot stirrer plate and stirred with a magnetic stirring bar at medium speed (400 rpm)

at room temperature. Then 39×10^{-3} mols of Et$_3$N were added and the solution became turbid within 10 seconds. A distillation apparatus was fitted on the flask as shown in **Scheme 2.3**. The temperature was set to 130 °C, well above the boiling points of both MeCN and Et$_3$N, and the stirring was adjusted at full speed. 380 mL of the reaction solution were distilled and stored in a glass bottle. The PCPBS nanospheres were collected from the remaining dispersion solution, by centrifugation at 8000 rpm for 10 min. The solids were washed 2 times with acetone and once with acetone/water mixture (1:1 v/v) and then dried in vacuum oven at 50 °C for 24 hours.

Scheme 2.3. Experimental apparatus for the eco-friendly and large synthesis of PCP**BS**.

2.3.5   Synthesis of PCPBS nanospheres in the recycled solution

The MeCN/Et$_3$N distilled solution from the scale-up method was reused to replicate the synthesis of PCPBS nanospheres. In a 500 mL RBF, 8.9 mmol of BPS were dissolved in 390 mL of the distilled solvent and the flask was placed in an oil bath on a magnetic hot stirrer at r.t. 2.6 mmol of HCCP were dissolved in 40 mL of fresh MeCN by sonication and then added directly to the flask under continuous stirring. Same as previously, particle formation was observed within 10 seconds and once again the solvent was distilled as described in the

previous paragraph and stored in glass bottle. The same procedure was continued for 2 more times using the collected solvent from the previous experiment.

2.4 Results and Discussion

2.4.1 The S_N2 substitution reaction between HCCP and BPS

The nucleophilic substitution reaction of HCCP and BPS, in the presence of Et_3N, is shown in **Scheme 2.4** and the reaction pathways are described; the phenol group of the BPS, as a week acid, is deprotonated and forms a phenoxide due to the high acid dissociation constant, ($pK_a = 17. 24$) of Et_3N in MeCN.

Scheme 2.4 Mechanisms of nucleophilic substitution reaction of HCCP by BPS in the presence of Et_3N as proposed in this study.

In a second step, the phenoxide anion acts as a nucleophile and attacks the P centre of the HCCP, with the simultaneous loss of one Cl$^-$ anion, which then is trapped from Et$_3$N to form the Et$_3$N·HCl salt. This process is repeated in a fast and random way and results initially in HCCP-BPS oligomers and finally in highly cross-linked 3D structures. Both the properties of the solvent and the pK_a value of the organic base, play essential roles in this reaction.

Since the above nucleophilic substitution is driven by a S$_N$2-type mechanism, an aprotic polar solvent is needed in order to stabilize the phenoxide anions which are the reactive species. On the other hand, polar protic solvents such as water and alcohols tend to stabilize the phenol homologues and thus reduce the reactivity of the nucleophile.[41] In Mechanism II, the BPS is initially weakly bonded to the HCCP and the phenol group attacks the P atom which results a build of positive charge on the O atom and a reduction of the pK_a of the phenol group. Then, Et$_3$N removes the proton and the loss the Cl$^-$ atom takes place following the formation of Et$_3$N·HCl salt. The above two mechanisms may take place simultaneously and the equilibrium between them could be adjusted by parameters such as temperature, solvent polarity, pK_a *etc*. This study was beyond the scope of the current research project.

2.4.2   Synthesis and characterisation of PCPBS nanospheres

2.4.2.1   Effect of [BPS]:[HCCP] mola ratio (MR$_{S:P}$) on the formation and morphology of PCPBS nanospheres

The PCP**BS** formation mechanism was studied through the morphological analysis of nanospheres synthesized under different conditions. Firstly, the [BPS]: [HCCP] molar ratio (MR$_{S:P}$) was varied from 1 to 6, while keeping the HCCP mass concentration at 1.13 mg/mL and Et$_3$N concentration at 0.5 M. At MR$_{S:P}$ =1, no particle formation was observed (transparent solution) even after reaction for over 5 hours. This indicates that the reaction proceeds up to poorly cross-linked oligomers which were not sufficient to form stable

primary nuclei. At $MR_{S:P}$ = 2 - 6, the solution became turbid within seconds upon addition of the Et_3N, thus indicated the particle formation. **Figure 2.2** shows the morphology of the nanospheres obtained under different $MR_{S:P}$.
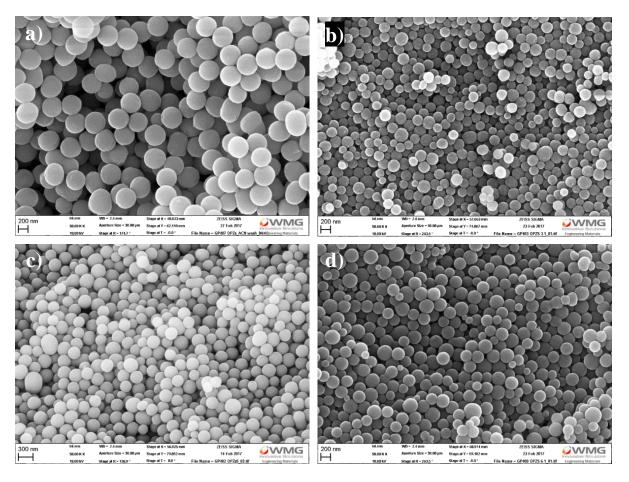
Figure 2.2. SEM images of PC**PBS** nanospheres synthesized in MeCN at different BPS: HCCP molar ratio a) 2:1, b) 3.5:1, c) 5:1 and d) 6:1. Magnification at 50 k x.

All samples were sub-micron spherical particles with relatively narrow size distribution and smooth surfaces. Specifically, at $MR_{S:P}$ = 2 the mean particle diameter was Đ = 390 ± 15 nm while, a low mass yield of 25 % was observed. By increasing the $MR_{S:P}$ to 3.5, a significant decrease of the particles' size (Đ = 190 ± 15 nm) with a simultaneously increase of the mass yield to 78%, was noticed (**Figure 2.2 b**). At $MR_{S:P}$ = 5 the diameter and mass yield were slightly increased to 240 ± 27 nm and 82 %, respectively (**Figure 2.2 c**). Finally, at the highest $MR_{S:P}$ = 6 the particle size did not change much Đ = 220 ± 37 nm), however, the

mass yield was lower than the $MR_{S:P}$ = 3.5 (**Figure 2.2 d**). Although, there is a correlation between the particle size and the $MR_{S:P}$, other factors such as impurities and sonication position could also contribute to the above differences. However, the differences in the mass yield indicated that there is a limit on the substitution reaction in an explanation can be given through the rate of the reaction kinetics.

A macroscopic observation of the solutions at the initial stage of the reaction showed that at $MR_{S:P}$ >2 the rate of the transparency change was noticeable faster than $MR_{S:P}$ = 2 where the solution remained only translucent. In this case, the low $MR_{S:P}$ resulted into oligomers of low cross-linking degree and consequently a small number of the primary nuclei (growth sites). The particle formation did not take place at $MR_{S:P}$ = 1, thus the speculation of the oligomers formation as well as their reactivity or "livingness" needed to be resolved. For this reason, the next experiments were performed; stoichiometric (Exp.6, Sol. A) and excess (Exp.7, Sol. B) amounts of Et_3N were added in MeCN solutions of HCCP and BPS of $MR_{S:P}$=1. No particle formation was observed, as expected. Then, 2.5 eq. of BPS (in 0.5 mL MeCN) were added in Sol. A, in order to replicate the experiment where $MR_{S:P}$ = 3.5. Again, no particle formation was observed, showing that the initial stoichiometric amount of Et_3N was fully protonated and no new phenoxides could be formed while the solution rapidly became turbid, only when extra amount of Et_3N was added. On the other hand, the initial excess amount of Et_3N in Sol. B resulted in the instant particle formation upon addition of 2.5 eq of BPS (in 0.5 mL MeCN), thus no additional Et_3N was needed. The results are shown in **Figure 2.3**. The nanospheres obtained from Exp.7 had a Đ = 700 ± 60 nm and exhibited smooth surfaces in contrast to the material of Exp.6, where the particles had rough surfaces with Đ =520± 70nm along with the presence of some smaller particles of Đ = 175 ± 40 nm), as shown in **Figure 2.3 a, b.** This result indicated that the nucleation and growth in Exp.6 took place in two stages while the PC**PBS** nanospheres obtained from Exp. 7 proceeded via a single step.
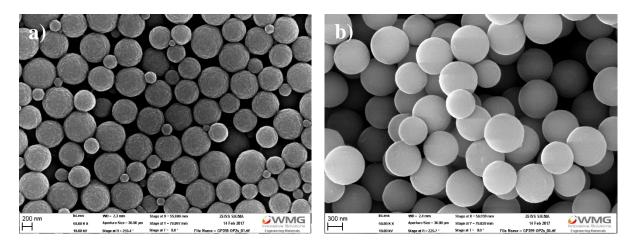
Figure 2.3. SEM images of PCPBS synthesized initially from $MR_{S:P} = 1$ and then $MR_{S:P} = 3.5$ with a) stoichiometric (Exp.6) and b) excess amounts of Et_3N (Exp.7). Mag. at 50 k x.

In the latter case, more oligomers were available to take part in the growth step rather in the nuclei formation step thus explaining the larger Đ. Here, it is important to highlight that the stoichiometric amount of Et_3N was calculated in accordance to the nucleophile and not to the HCCP concentration, since Et_3N is not get involved in any P-Cl cleavage. The presence of some smaller nanospheres is unavoidable since the reaction is very fast resulting to a variation of nucleation and growth rates which are also affected by the fact that the sonication power is not evenly distributed throughout the water bath. From the current results as well as from the published findings, the above reaction can be explained by the LaMer nucleation and growth mechanism, which evolves in three distinguished phases[42, 43]:

    i.   An initial monomers' concertation above S_C is necessary to break the energy barrier of the homogenous nucleation

    ii.   Fast primary nuclei formation and decrease of monomers' concertation below S_c (no further nucleation).

    iii.   Simultaneous growth of the primary nuclei into stable particles.
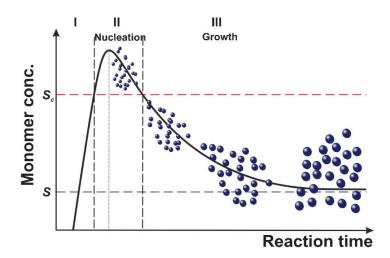
Figure 2.4. LaMer plot illustrating the separation of nucleation and growth during the synthesis of monodisperse NPs. S and Sc are supersaturation and critical supersaturation, respectively.[44]

2.4.2.2 Effect of the nucleophile's stereochemistry

Another important parameter that influences the morphology of the resulting particles is the geometry of the nucleophilic building block. Analogous to the above experiments, Huang *et*.al*.,* have previously reported the synthesis of polyphosphazene microspheres through the reaction of HCCP with *4,4'*-oxidianiline (ODA) in MeCN under sonication conditions [24]. Contrary to the results presented here, they showed that sub-micron spheres of 0.5 µm were obtained even at low ODA:HCCP molar ratio, $MR_{O:P} = 1$, and an increase of the $MR_{O:P}$ resulted in an increase of the particle size up to 2.5 µm. This difference can be explained by the different stereochemistry and geometry of BPS and ODA and consequently their different nucleophilic reactivity. **Scheme 2.5** represents the 3D structure of BPS and ODA on the same coordinate (001) view. In general, the phenylamines are stronger nucleophiles than phenols, however in the particular solvent-base system the produced phenoxides, are more reactive than the phenylamines since the pK_a of Et_3N is not sufficient high in order to fully deprotonate ODA. Therefore the reaction proceeds in much slower rate. Additionally, the

high reactivity of BPS is favoured by the presence of the bridged sulfone group which is more electron withdrawing group than the bridged O of ODA.

4,4'- sulfonyl diphenol   *4,4'- oxidianiline*
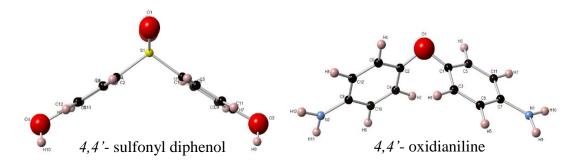
Figure 2.5. Stereochemical structures of BPS and ODA.

The differences in the nucleophilic activities were also confirmed from the significant difference reaction times where **PCPBS** were formed almost instantly while the ODA-based OPZs formed in at least 20 minutes after the addition of Et$_3$N.[24] The second noticeable difference is the different angles between the neighbouring benzene rings and the bridging groups. In general, the S$_N$2 reaction occurs with inversion of configuration where the nucleophile attacks the chiral atom from the opposite side of the leaving group (back attack). [41] In the case of the cyclic hexachlorophosphazene, an attack from the nucleophile to the P atom will substitute one Cl, but the geminal Cl on the same P atom is less likely to be substituted from a second nucleophile due to the steric hindrance effects. This is expected to have an effect on the substitution degree of the Cl atoms of the HCCP ring due to the different stereochemical hindrance of BPS and ODA. The degree of nucleophilic substitutions of the six Cl atoms is highly depended on the stereochemistry of the substituent and for diphenols or diphenylamines it has been previously shown that non-geminal substitution is more likely to take place instead of neighbouring Cl replacement (geminal substitution).[45] Consequently, the **PCPBS** chemical structure is expected to have a theoretical building block ratio BPS: HCCP = 3. The above assumption is also supported by the fact that the mass yield of **PCPBS**-6 was lower than the **PCPBS**-3.5, indicated that there was excess of

BPS which remained unreacted. On the other hand, **PCPBS-5** with the highest yield indicated

that at $MR_{S:P} = 3.5$ a small amount of HCCP remained unreacted with and a further addition of

BPS increased the yield.

2.4.2.3 Effect of the solvent properties on the particle formation

As mentioned above, the kinetics of the nucleophilic substitution reaction is highly dependent

on the polarity of the solvent and, subsequently, affect the morphology of the produced

nanospheres. For comparison **PCPBS** nanospheres were synthesized in acetone under the

same synthetic conditions as presented in the previous paragraph and $MR_{S:P} = 3.5$ was

selected as a reference. It was noticed that the particle formation in acetone was much slower

(few minutes) compared to the same experiment in MeCN and resulted in 53 % mass yield of

large microspheres of $Đ = 900 \pm 50$ nm of, while the particles synthesized in MeCN were

significantly smaller with $Đ = 190 \pm 25$ nm (**Figure 2.6**).
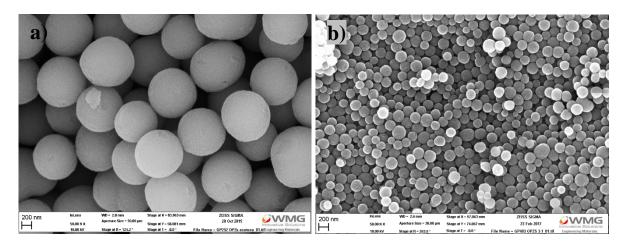
Figure 2.6 SEM images of PCP**BS** synthesized at $MR_{S:P} = 3.5$ in **a)** acetone and **b)** MeCN.

Likewise in acetone, similar results were observed when the reaction performed in solvents

such as dichloromethane (DCM) and *1,4*-dioxane, that do not belong to the family of aprotic

polar solvents. The reaction in both cases resulted in a low mass yield (~ 19-29%) of

nanospheres of $Đ = 265 \pm 60$ nm in DCM (**Figure 2.7 a, b**) and microspheres of $Đ \approx 2.5 \pm$

0.25 μm in *1,4*-dioxane (**Figure 2.7 c**). The formation of large particles in dioxane was

attributed to its low dipole moment and dielectric constant which affected the reaction rate and consequently the nucleation and growth proceeded in much lower speed than in DCM. Additionally, large micron-sized structures were found under SEM examination which were suggested to be unsolubilized Et$_3$N·HCl crystals (**Figure 2.7 d**). Contrary to the above solvents, the reaction in DMSO was not successful and no particle formation was observed.
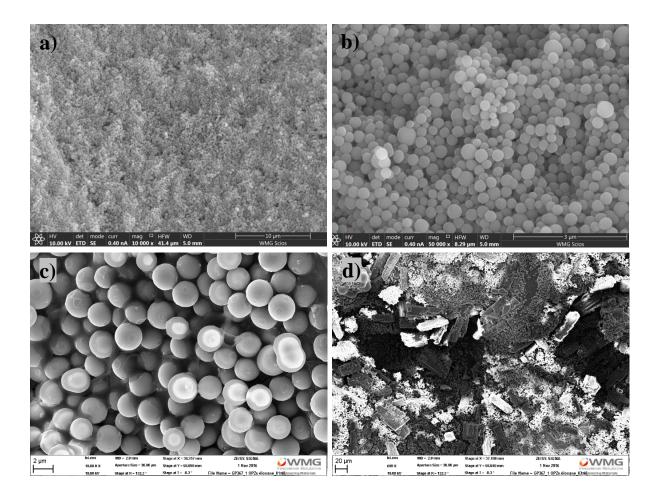
Figure 2.7 SEM images of PCPBS particles synthesized in a, b) DCM and c, d) *1, 4*-dioaxane.

2.4.2.4 Effect of different organic bases on the morphology

As described earlier, the role of the organic base is firstly to deprotonate the nucleophile, and then to serve as the acceptor of Cl$^-$ that is released from the substitution reaction. In order to investigate the effect of the chemical structure of the organic base, **PCPBS**s were synthesized in MeCN utilizing organic bases with different chemical structures as shown in **Scheme 2.5**.

TMEDA with two tertiary amines, PMDETA with three tertiary amines, Me$_6$TREN and DMAP were successfully promoted the S$_N$2 reaction and the formation of nanospheres, showing in this way the versatility of the method and the expansion of the synthetic procedure.

Scheme 2.5. Chemical structures of the alternative to Et$_3$N organic bases used for the synthesis of **PCPBS** particles.

From the SEM micrographs in **Figure 2.8**, it can be seen that nanospheres of Đ≈ 240 ± 25 nm were obtained when PMDETA was used while, TMEDA resulted to larger and more polydispersed nanospheres of Đ ≈ 340 ± 70 nm. The sample prepared with DMAP was rather polydispersed and highly agglomerated, however, particles of D = 255 ± 70 nm were measured. Here, the pK_a value of the organic base determined the rate of the reaction and consequently the particle size and PDI. PMDETA owing three tertiary amines should be more reactive than Et$_3$N thus the reaction equilibrium is shifted faster towards the phenoxide formation. This was also confirmed macroscopically by the faster change of the solution turbidity when PMDETA was used. On the other hand, TMEDA with pK_a of 9.87 showed a similar sample morphology to Et$_3$N experiment. It is noteworthy to highlight that the mass

yield of these series of experiments was similar to the results from Et_3N. This result shows

that Et_3N is not the ultimate choice as highlighted from the summary of literature in **Table 2.1** and other organic base can also be selected for the synthesis of PCB**PS** nanospheres.
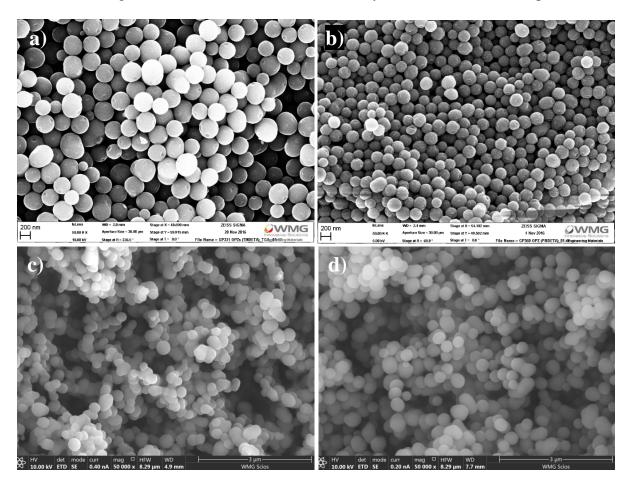
Figure 2.8. SEM images of PCP**BS** synthesized in MeCN with a) TMEDA, b) PMDETA, c) DMAP and d) Me_6TREN.

The agglomerated structure of the PCP**BS** prepared with DMAP could be due to the fact that

either the phenoxide formation is slow or the substitution, in this case, follows Mechanism II

(see **Scheme 2.4**). This was also attributed to the pK_a of DMAP (17.95) which is close to the

BPS (7.8) so the phenoxide formation rate is low. Additionally, the poor solubility of the

DMAP·HCl in MeCN is a concern that might have had an effect on the reaction kinetics.

2.4.3 PCPBS hollow Nano-flowers

As mentioned before, Et$_3$N·HCl salt, the by-product of the S$_N$2 reaction, is formed and re-dissolved in the solvent (MeCN, acetone, DCM) instantly and only in *1,4*-dioxane a poor solubility resulted the formation and precipitation of large Et$_3$N·HCl crystals, although **PCPBS** nanospheres were also produced. Tang et al., have previously reported that the poor solubility of Et$_3$N·HCl in THF resulted in the *in situ* formation of rod-like nanocrystals which served as templates for the formation of cyclomatrix organophosphazene nanotubes (PZT). Similarly, Zhang *et.*al*.,* prepared melamine-based organophosphazene nanotubes (PZM) in the presence of pyridine which served both as solvent and base.[46] The morphological differences between the PZT and PZM nanotubes, rely on the structure of the melamine as well as on the dispersity method (stirring *vs.* sonication), however, tubular structures were obtained in both cases.

In this project, a similar strategy to the synthesis of OPZ nanotubes was followed except that PMDETA -instead of Et$_3$N- was used. As **Figure 2.9** shows, the morphology of the sample was completely different compared to the reports utilized Et$_3$N, and micron sized spherical particles of D = 8.8 ± 1.1 μm were obtained. A closer observation revealed that the microspheres consisted of smaller particles of various sizes and shapes, and had agglomerated appearance. However, a washing step with acetone/water mixture revealed that the microspheres were completely disappeared indicating an aggregated structure rather than agglomerated. The previous appearance of a continuous mass was attributed to PMDETA·HCl absorbed on the surface. The internal structure of the microspheres was also revealed by the SEM analysis of the carbonisation traces after heating the sample (washed only with THF) to 1000 °C. The presence of some holes with relatively large openings proved the hollow structure of the carbonized material.
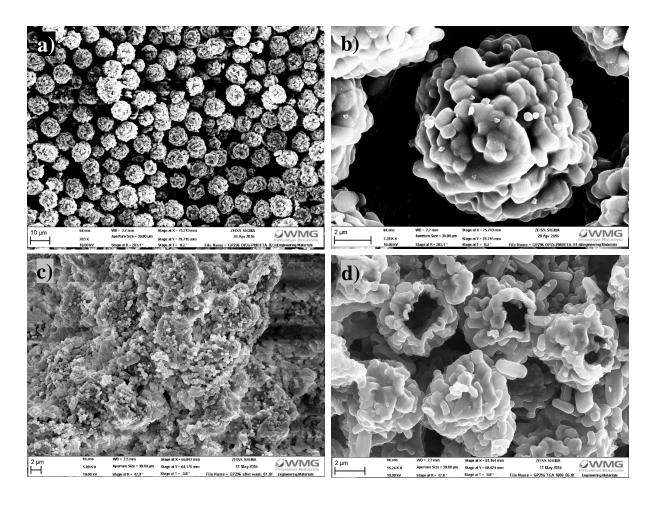
Figure 2.9. SEM images of **a, b)** PC**PBS** microspheres obtained in THF/PMDETA, **c)** after washing with acetone/water **d)** the as obtained PC**PBS** microspheres after carbonisation at 1000 °C.

2.4.4   Scaled-up synthesis of PCPBS nanospheres

The already reported synthetic procedures for the production of cyclomatrix OPZ nanospheres and nanotubes involved ultra-sonication, long reaction times, and a relatively low HCCP concentration ≤ 1 mg/mL. These conditions, which are also found in other nanomaterials synthesis, are convenient for lab-scale synthesis, fundamental studies of the reactions mechanisms, and properties characterization. However, for the realization of these materials to industrial scale production and real life applications, simplified procedures are needed in order to minimize the environmental impact and the cost of the production.

In this section, a simple and efficient method is presented for the scaled-up synthesis of PCP**BS** nanospheres. The idea and design of the proposed method were born from: i) the initial experiments' observations, ii) the need of larger quantities for the electrochemical testing presented in Chapters 4 and 5, and iii) the available lab-scale equipment. In general, it was observed that the S_N2 reaction of HCCP and BPS in MeCN was rapid (~10 sec) which was also macroscopically confirmed by the instant transformation of the initially transparent solution to a white dispersion of PCP**BS** nanospheres. Therefore, a rough comparison of the products obtained from long and short time reactions was needed in order to estimate if the procedure could be simplified in terms of time scale. Indeed, PCP**BS** nanospheres obtained after 10 min of reaction had similar mean diameter, shape, surface morphology and mass yield as with the nanospheres obtained after 3 hours of continuous sonication (for simplicity these results are not presented). Thus, it can be concluded that the growth step is terminating in the early stages of the experiments and no other nucleation and growth process is taking place after the initial formation of the particles as the particle size deviation was independent of the reaction time. Secondly, similar results were obtained when the reaction was performed under mild stirring conditions instead of ultrasonication. Consequently, the reaction time could be minimized to few minutes time and the stirring method is easier to be applied in larger scale rather than sonication. One more problem to overcome was the limitation on the building blocks concentration. It has been reported before that a high HCCP concentration ≥ 4 mg/mL tends to form particles with irregular shapes and agglomerates.[24] *Ipso facto*, this reflects that a large quantity of solvent is required for a large scale synthesis and consequently multiple centrifugations in order to collect the particles. Here, a new distillation precipitation setup was designed for the scale-up synthesis of PCP**BS** nanospheres, as illustrated in **Scheme 2.3**. The SEM of the PCP**BS** synthesized with the distillation precipitation method from fresh solvent as well as from the previously distilled

solvent containing Et$_3$N, are shown in **Figure 2.10**. The morphology and topography of the samples was similar to the samples prepared under sonication.
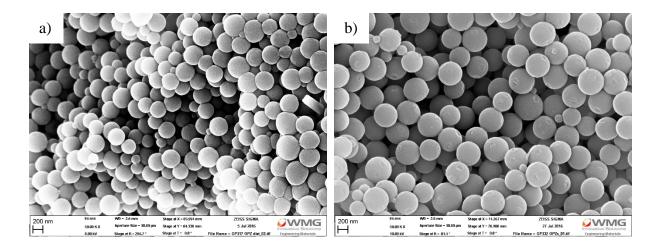
Figure 2.10. SEM images of **PCPBS** synthesized under distillation precipitation conditions a) with fresh and b) recycled MeCN/Et$_3$N.

2.4.5   Characterisation of the PCPBS nanospheres

2.4.5.1   FT-IR spectroscopy analysis

The chemical structure of the **PCPBS** was studied by the analysis of the ATR FT-IR spectra (**Figure 2.11**). The contribution of BPS in the IR spectra was shown by the characteristic peaks from the phenyl C-C/C=C vibrations at 1585 cm^{-1} and 1488 cm^{-1} as well as from the sulfone group vibrations at 1290 cm^{-1} and 1145 cm^{-1}.[47] The phosphazene trimer showed only one "exocyclic" P-N vibration at 1182 cm^{-1} while the second "exocyclic" at 1126 cm^{-1} and the 2 "endocyclic" at 1285 cm^{-1} and 1221 cm^{-1} [48] were not visible due to the overlapping with the BPS vibrations. For comparison reasons the infrared spectra of the starting materials, HCCP and BPS, are shown in **Figure 2.12a.** The absence of the strong absorption at 3360 cm^{-1} from the O-H (phenol) as well as the appearance of the peak at 935 cm^{-1} attributed to the

P-O-C$_{ph}$ stretch vibrations showed the successful substitution reaction of the P-Cl by the phenol groups.
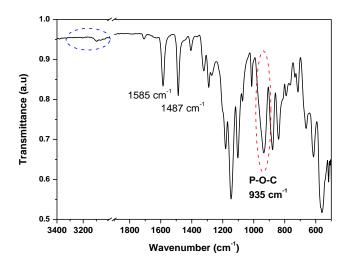
Figure 2.11. FT-IR spectrum of the PC**PBS**-3.5 nanospheres.

Furthermore, **Figure 2.12b** shows a comparison of the phenyl C=C stretch vibrations before (BPS) and after (PC**PBS**) the substitution reaction. It can be seen that the initial doublet at 1439 cm^{-1}/1602 cm^{-1} was transformed to a singlet at 1585 cm^{-1} while, the second pair of peaks showed a red shift (towards lower wavenumbers) and a change of their intensity ratio. This result was attributed to the bonding with the electron withdrawal P atom which disturbs the π-electron cloud of the phenyl rings.
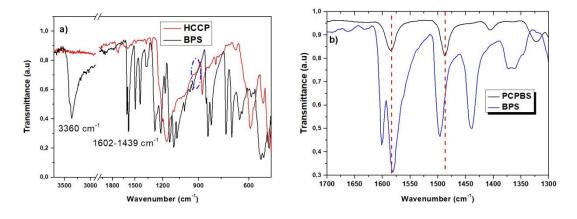
Figure 2.12. FT-IR spectrum of **a)** HCCP and BPS, and **b)** comparison spectra of PC**PBS** nanospheres and BPS showing the changes of the phenyl C=C stretch vibrations.

2.4.5.2 Thermogravimetric analysis

The thermal degradation behaviour of the PCP**BS** nanospheres was studied by the TG analysis of the powders. **Figure 2.13** shows the TGA curves obtained under N_2 for PCP**BS** and the starting materials, HCCP and BPS. The first mass loss step from 25-120 °C is originated from the atmospheric moisture or molecular water absorbed on the surface of the nanospheres. The first degradation onset temperature point (T^1_{on}) is located at around 480 °C and is almost completed just above 530 °C.
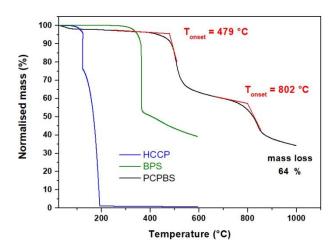
Figure 2.13. TGA curves of PCP**BS**, HCCP and BPS obtained under N_2 atmosphere.

At T^1_{on} the collapse of the entanglement network is taking place followed by i) the breakage of the cross-linking points, ii) rearrangement of the atoms and iii) the loss of small molecules/fragments. The above processes lead to the transformation of the OPZ network to carbon material. Above 700 °C, a second mass loss was observed which has not been shown before in the related literature. The T^2_{on} at ~ 800°C contributed to an extra mass loss of 25 % resulting to a total mass loss of 64 % at 1000 °C. It should be noted that both mass losses are characterized by negative slops at the end of each step, indicating that the mass loss is continuous in all the range of temperatures above 480 °C. A further investigation of the processes and the fragments involved in these mass loss steps is presented in **Chapter 4** (**par.**

4.4.3). A comparison between the curve of the as prepared nanospheres and the curves of the starting materials, BPS and HCCP, showed that the cross-linked network of the PCP**BS** provided a significantly higher thermal stability.

2.4.5.3   XPS analysis

The XPS spectrum of the PCP**BS** nanospheres was analysed in detail, in order to reveal the surface chemical composition and the electron binding energies of each atom. The representative survey scan shown in **Figure 2.14** revealed the material composition consisted of C, N, P, S, O and Cl.
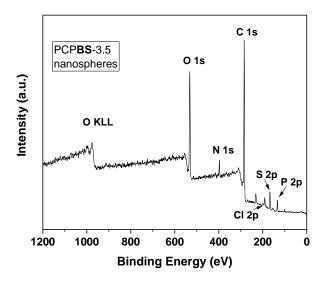
Figure 2.14 XPS survey scan of PCP**BS** nanospheres.

The PCP**BS** synthesised at different $MR_{S:P}$ did not show any spectra difference to the PCP**BS**-3.5 thus only this sample is presented for simplicity reasons. **Table 2.3** shows the experimental and theoretical atomic weight of each element for the samples with low, mid and high BPS: HCCP molar ratio. In each case, the calculated theoretical values were based on the assumption that the BPS molecules substitute the same number of Cl atoms in the HCCP ring. For all the samples the O and S at% originated from the BPS were almost

constant and the measured the S:P at% ratio was ~1 regardless the initial BPS:HCCP molar ratio. This result along with the discussion in the previous paragraphs clearly shows indicating that the HCCP was substituted by only three BPS molecules. Accordingly, the explanation of the lower mass yield of PCP**BS**-6 and the presence of excess BPS are further supported by the result above. In conclusion, an excess amount of BPS would not increase the substitution degree of HCCP, resulting to "higher crosslinking" of the nanospheres or larger particles and all PCP**BS** have the same BPS: HCCP ratio. This result also showed that the level of heteroatom doping of the carbon derivatives, as discussed in Chapter 4, cannot be controlled by the synthesis conditions. Additionally, the experimental data were in agreement with the Theoretical-3 calculation (**see Table 2.3**) assuming that the chemical formula of the unit cell is $C_{36}O_{12}S_3P_3N_3Cl_3$ and the molecular weight 961.874 g/mol. Compared to the theoretical calculations, the experimental samples showed higher C at% due to adventitious carbon contamination, which is usual in XPS measurements.

Table 2.3. Elemental composition by XPS.

Sample	C 1s	O 1s	S 2p	P 2p	N 1s	Cl 2p
	Atomic weight %					
PCPBS-2	69.7	19.2	4.0	4.0	2.8	0.3
Theoretical-2	38.07	16.91	8.47	12.27	5.55	18.73
PCPBS-3.5	69.5	19.3	4.0	4.1	2.7	0.4
Theoretical-3.5	47.4	21.05	10.55	8.33	3.95	8.33
PCPBS-6	68.7	20.0	4.0	4.1	2.8	0.4
Theoretical-6	54.87	24.36	12.21	5.9	2.67	-
Theoretical-3	44.95	19.96	10.0	9.66	4.37	11.06

The high resolution scans of each element along with the de-convoluted fitted peaks are presented in **Figure 2.15**.
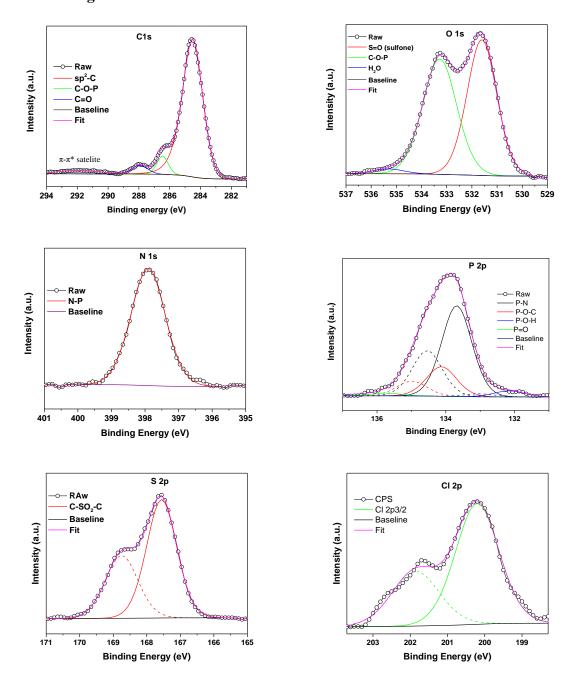
Figure 2.15 Core-level scans of all the elements present in PCP**BS** nanospheres.

The C 1s photoline consisted of three peaks at 284.6, 286.4 and 287.9 eV assigned to the sp^2-C from the phenyl rings, C-O-P[49] from the bonding of BPS with the P atom and C=O as terminal (surface) or unreacted phenol. A low and broad intensity peak was observed at ~292

eV, a characteristic of the non-covalent π-interactions that may be present due the random configuration of the BPS molecules. The O 1s peak was resolved in two peaks at 531.6 eV and 533.3 eV which originated from the sulfone oxygens and the P-O-C bond, respectively. A smaller peak at higher eV was attributed to molecular-level adsorbed water. A double binding state was found for the P 2p peak which was fitted with 2 pair of peaks (P $2p_{3/2}$ and P $2p_{1/2}$) due the orbital splitting. The energy splitting was set to 0.86 eV while the area intensity ratio was 2:1. For clarity the p1/2 peaks are shown with dashed lines. The first pair at 133.7 and 134.5 eV was assigned to the phosphazene-type phosphorus (P-N)[50] and the second pair at 134.1 and 135.0 eV to the P-O-C bonding. The area ratio of the [P-N]:[P-O] species was 3:1 indicating also here the stoichiometric of the PZ-BPS structure. The two smaller peaks at 132.6 and 135.7 eV were attributed to to P-O-H and P=O from the reaction with atmospheric water. The single fitted peak of N 1s at 397.9 eV indicated the presence of only phosphazene-type nitrogen (P=N, P-N) and no organic N was detected showing that $Et_3N \cdot HCl$ was completely washed out. Sulphur was also present in a single energy state characterised by a S p3/2 - S p1/2 orbital splitting of 1.18 eV at 167.6 and 168.8 eV assigned to the sulfone group (C-SO_2-C). Finally, the presence of Cl 2p3/2 at 200.2 eV and Cl 2p1/2 at 201.9 eV was attributed to the presence of some unreacted P-Cl.

2.5 Conclusions

The production of PCP**BS** nanospheres was studied under various synthetic conditions and the properties of solvent and organic base are proved to be crucial for the morphology development of the particles. The $MR_{S:P}$ did not have any significant effect on the size of the PCP**BS** for $MR_{S:P} > 2$ and the XPS analysis showed a 3:1 stoichiometry of BPS to phosphazene. Therefore, the substitution degree is constant and independent of the $MR_{S:P}$. Contrary to other reported OPZ systems, here, when $MR_{S:P} = 1$ was used no particle

formation was observed, which was explained by the significant differences of the stereochemistry and reactivity of the nucleophiles in MeCN solutions of Et_3N. By changing the organic base from Et_3N to PMDETA, hollow PCP**BS** microspheres and their carbon derivatives from pyrolysis treatment were obtained. Additionally, a new synthesis set-up based on a distillation precipitation method and use of recycled solvent and Et_3N, was presented. This facile method enables the realisation of scale-up these materials in industrial production due to its low-cost and environmental-benign. A detailed S_N2 nucleophilic substitution mechanism between HCCP and BPS (or any other nucleophile) was proposed based on fundamental organic chemistry theory. This approach helps not only an in-depth understanding of the synthesis mechanism and formation the cyclomatrix OPZ nanostructures, but also opens a pathway towards the design of new experiments and related materials for the future.

2.6   References

1. I. Freestone, N. Meeks, M. Sax and C. Higgitt, *Gold Bulletin*, 2007, **40**, 270-277.

2. T. Xing, J. Sunarso, W. Yang, Y. Yin, A. M. Glushenkov, L. H. Li, P. C. Howlett and Y. Chen, *Nanoscale*, 2013, **5**, 7970-7976.

3. C. C. Koch, *Nanostructured Materials*, 1993, **2**, 109-129.

4. G. S. Pappas, P. Liatsi, I. A. Kartsonakis, I. Danilidis and G. Kordas, *Journal of Non-Crystalline Solids*, 2008, **354**, 755-760.

5. I. A. Kartsonakis, I. L. Danilidis, G. S. Pappas and G. Kordas, *Journal of Nanoscience and Nanotechnology*, 2010, **10**, 5912-5920.

6. T. J. Daou, G. Pourroy, S. Bégin-Colin, J. M. Grenèche, C. Ulhaq-Bouillet, P. Legaré, P. Bernhardt, C. Leuvrey and G. Rogez, *Chemistry of Materials*, 2006, **18**, 4399-4404.
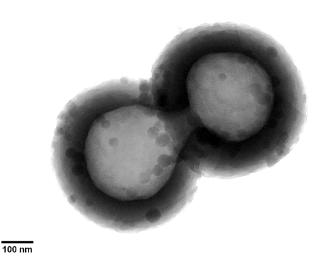
7.   E.-P. Ng, D. Chateigner, T. Bein, V. Valtchev and S. Mintova, *Science*, 2012, **335**, 70-73.

8.   P. Bilalis, N. Boukos and G. C. Kordas, *Materials Letters*, 2012, **67**, 180-183.

9.   R. Mueller, L. Mädler and S. E. Pratsinis, *Chemical Engineering Science*, 2003, **58**, 1969-1976.

10.   E. Perez-Tijerina, M. Gracia Pinilla, S. Mejia-Rosales, U. Ortiz-Mendez, A. Torres and M. Jose-Yacaman, *Faraday Discussions*, 2008, **138**, 353-362.

11.   M. Hood, M. Mari and R. Muñoz-Espí, *Materials*, 2014, **7**, 4057-4087.

12.   X. Feng, X. Ding and D. Jiang, *Chemical Society reviews*, 2012, **41**, 6010-6022.

13.   Y. Zhu, X. Huang, W. Li, J. Fu and X. Tang, *Materials Letters*, 2008, **62**, 1389-1392.

14.   J. Köhler, S. Kühl, H. Keul, M. Möller and A. Pich, *Journal of Polymer Science Part A: Polymer Chemistry*, 2014, **52**, 527-536.

15.   Z. Huang, F. Zheng, S. Chen, X. Lu, C. G. Catharina Elizabeth van Sittert and Q. Lu, *RSC Adv.*, 2016, **6**, 75552-75561.

16.   O. Sahin, O. K. Koc, H. Ozay and O. Ozay, *Journal of Inorganic and Organometallic Polymers and Materials*, 2016, **27**, 122-130.

17.   W. Wei, X. Huang, X. Zhao, P. Zhang and X. Tang, *Chemical communications*, 2010, **46**, 487-489.

18.   Y. Wang, L. Shi, W. Zhang, Z. Jiang and J. Mu, *Polymer Bulletin*, 2013, **71**, 275-285.

19.   X. Wei, G. Zhang, L. Zhou and J. Li, *Applied Surface Science*, 2017, DOI: 10.1016/j.apsusc.2017.04.236.

20.   L. Zhu, Y. Xu, W. Yuan, J. Xi, X. Huang, X. Tang and S. Zheng, *Advanced Materials*, 2006, **18**, 2997-3000.

21.   L. Zhu, Y. Zhu, Y. Pan, Y. Huang, X. Huang and X. Tang, *Macromolecular Reaction Engineering*, 2007, **1**, 45-52.

22.   Z. Lu, Y. Weizhong, P. Yang, T. Xiaozhen and H. Xiaobin, *Polymer International*, 2006, **55**, 1357-1360.

23.   Y. Zhu, X. Huang, J. Fu, G. Wang and X. Tang, *Materials Science and Engineering: B*, 2008, **153**, 62-65.

24. P. Zhang, X. Huang, J. Fu, Y. Huang, Y. Zhu and X. Tang, *Macromolecular Chemistry and Physics*, 2009, **210**, 792-798.

25. T. Pan, X. Huang, H. Wei, W. Wei and X. Tang, *Macromolecular Chemistry and Physics*, 2012, **213**, 1590-1595.

26. W. Wei, X. Huang, K. Chen, Y. Tao and X. Tang, *RSC Advances*, 2012, **2**, 3765.

27. W. Wei, R. Lu, S. Tang and X. Liu, *J. Mater. Chem. A*, 2015, **3**, 4604-4611.

28. K. Chen, C. Wan, W. Wei, X. Huang and H. Liu, *Materials Letters*, 2015, **139**, 93-97.

29. R. Muhammad, P. Rekha and P. Mohanty, *RSC Adv.*, 2016, **6**, 17100-17105.

30. S. U. Dar, S. Ali, M. U. Hameed, Z. Zuhra and Z. Wu, *New J. Chem.*, 2016, **40**, 8418-8423.

31. Z. Li, G. Wang, A. Zhang, L. An and Y. Tian, *Journal of Applied Polymer Science*, 2016, **133**, 1-7.

32. L. Meng, C. Xu, T. Liu, H. Li, Q. Lu and J. Long, *Polym. Chem.*, 2015, **6**, 3155-3163.

33. H. Ozay and O. Ozay, *Colloids and Surfaces A: Physicochemical and Engineering Aspects*, 2014, **450**, 99-105.

34. Y. Hu, L. Meng and Q. Lu, *Langmuir : the ACS journal of surfaces and colloids*, 2014, **30**, 4458-4464.

35. S. Zhang, X. Zhao, B. Li, C. Bai, Y. Li, L. Wang, R. Wen, M. Zhang, L. Ma and S. Li, *Journal of hazardous materials*, 2016, **314**, 95-104.

36. P. Mohanty, L. D. Kull and K. Landskron, *Nature communications*, 2011, **2**, 401.

37. J. Fu, X. Huang, Y. Zhu, Y. Huang and X. Tang, *Applied Surface Science*, 2009, **255**, 5088-5091.

38. J. Fu, M. Wang, C. Zhang, P. Zhang and Q. Xu, *Materials Letters*, 2012, **81**, 215-218.

39. J. Fu, Y. Huang, Y. Pan, Y. Zhu, X. Huang and X. Tang, *Materials Letters*, 2008, **62**, 4130-4133.

40. M. Ciampolini and N. Nardi, *Inorganic Chemistry*, 1966, **5**, 41-44.

41. M. B. Smith and J. March, in *March's Advanced Organic Chemistry*, John Wiley & Sons, Inc., 2006, DOI: 10.1002/9780470084960.ch10, pp. 425-656.

42.   V. K. LaMer and R. H. Dinegar, *Journal of the American Chemical Society*, 1950, **72**, 4847-4854.

43.   N. T. Thanh, N. Maclean and S. Mahiddine, *Chemical reviews*, 2014, **114**, 7610-7630.

44.   T. D. Schladt, K. Schneider, H. Schild and W. Tremel, *Dalton Trans*, 2011, **40**, 6315-6343.

45.   R. De Jaeger, *Progress in Polymer Science*, 1998, **23**, 179-276.

46.   Z. Li, G. Wang, C. Liang and A. Zhang, *Applied Surface Science*, 2015, **347**, 541-547.

47.   W. Liu, X. Huang, H. Wei, K. Chen, J. Gao and X. Tang, *Journal of Materials Chemistry*, 2011, **21**, 12964.

48.   R. K. Voznicová, J. Taraba, J. Příhoda and M. Alberti, *Polyhedron*, 2008, **27**, 2077-2082.

49.   A. M. Puziy, O. I. Poddubnaya and A. M. Ziatdinov, *Applied Surface Science*, 2006, **252**, 8036-8038.

50.   A. B. Boscoletto, M. Gleria, R. Milani, L. Meda and R. Bertani, *Surface and Interface Analysis*, 2009, **41**, 27-33.

Chapter 3 Aqueous induced self-templated formation of

hollow OPZ nanospheres

100 nm

The in situ formation of hollow organophosphazene (OPZ) nanospheres in MeCN-H₂O solutions is discussed. The morphological examination of the obtained materials and the studies at various conditions indicated a self-template–direct formation mechanism which is differentiated from the Ostwald ripening process. A self-formed cluster consisted of hydrolysed and weakly cross-linked oligomers along with a simultaneously dissolution of the unstable inner walls of the shells is proposed. Furthermore, stable hollow carbon nanospheres were obtained after a pyrolysis treatment.

3.1 Introduction
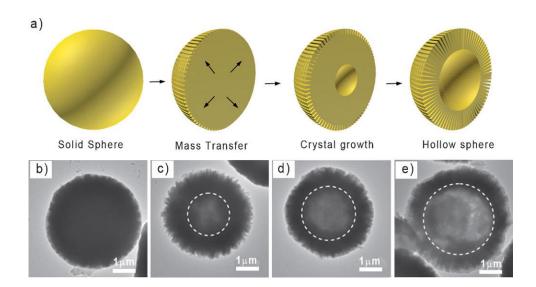
3.1.1 Strategies to hollow nanostructures

Hollow nano-spheres or micro-/nano-capsules have always been a fascinating research area for diverse applications ranging from catalysis[1], drug delivery[2], energy storage[3], gas sensors[4] and many others, and with a profound impact in advanced technologies. The most known and reported method for the synthesis of hollow nanospheres (either inorganic or organic) is the "sacrificial-template" method which is categorized into the "hard" and "soft" template methods [5]. In the first type, inorganic or polymeric spherical particles (*e.g.* SiO_2, PS latex, etc.) provide the confined surfaces for the nucleation and growth of inorganic salts or the polymerization of organic monomers, which finally form a stable coating (shell) around the initial templates. A subsequent selective removal (*e.g.* acid, organic solvents, pyrolysis process[6]) of the template, creates a void space and leaves an intact shell. The major advantage of this method is the high control over the cavity size and the shell thickness, provided by the morphology of the template and the coating chemistry, respectively. On the contrary, the multi-step process and the core removal involving expensive, harsh and environmental non-friendly conditions are the main drawbacks of the hard-template method, which limit its application. The soft-template methods involve the utilization of emulsions[7], micelles[8] and gas bubbles[9], however, the required multiple synthesis or toxic gases usage along with the extensively processes for the core removal are some of the limitation of this method for industrial production. Furthermore, the cavity size and shell thickness dispersity indexes are usually broad since these high entropic systems are easily affected by changes in the provided energy (thermal, mechanical, *etc.*).

3.1.2 Self-templated nanostructures

Hollow nanostructures can also be obtained directly from their dense forms by a self-deconstruction of the material located in the core of the nanostructure. The basis of such

systems mainly relies on the formation of thermodynamic stable large particles counter to smaller high energetic and unstable particles. The "self-templating" phenomenon has been observed for numerous metals and metal oxides and it has been reported as the Ostwald ripening [10], the Kirkendall effect[11], galvanic replacement[12] and surface-protecting etching [13]. Specifically, Ostwald ripening is described by the dissolution of the initial formed nuclei (core) which provide the substrates for the growth process and the subsequent mass diffusion of the solubilized salts through the pores which finally are redeposited on the outer shell, thus contributing in the growth process.[10] The Ostwald ripening effect has been extensively reported as the self-templated mechanism for formation of hollow inorganic particles but it has been rarely observed in organic chemistry or hybrid systems. In 2009 Jung et al. observed for the first time the self-templated-directed formation of hexagonal tubes and rings of a Zn(OAc)$_2$ coordination-polymer system [14] and a year later, Huo et al. reported the synthesis of hollow ferrocenyl coordination polymer microspheres formed by Ostwald ripening.[15] The general Ostwald ripening mechanism and the step-by-step established morphologies are shown in **Scheme 3.1**.
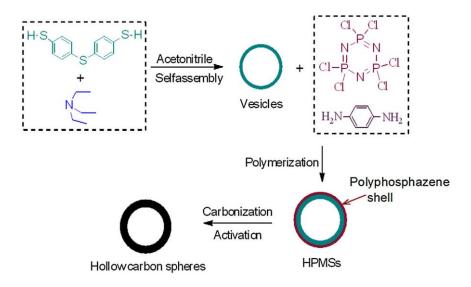
Scheme 3.1 a) Step-by-step schematic representation of the Ostwald ripening process and b, c, d, e) the dense to hollow structural evolution of ferrocenyl coordination polymer microspheres under TEM observation.[17]

Recently, self-templated hollow metal-organic frameworks (MOFs) and covalent organic frameworks (COFs) were also synthesized and the formation mechanism was assigned to the Ostwald ripening. Lee et al. prepared hollow Zinc-benzenetricarboxylic acid microparticles which were subsequently transformed to ZnO inorganic particles by calcination at 600 °C. Similarly, Tan et al. prepared ZIF-67 hollow spheres and their transition metal-doped derivatives (Cu, Zn) and also extended their approach to other type of MOFs, such as HKUST-1. However, in this method a surfactant was used for the formation of initial vesicles. More interestingly, hollow spherical COFs based on *2,5-dihydroxyterephthalaldehyde* and *1,3,5*-tris (4-aminophenyl)benzene (COF-DhaTab) were reported in 2015 by Kandabeth et al. and up to date it is the only report of pure organic-based hollow structure derived from Ostwald ripening.[16] The reported hollow COF-DhaTab microspheres exhibited high crystallinity and a mesoporous structure which resulted to a high surface area of 1500 m^2/g. On the other hand, when a building block of non-C_3-symmetry was used, the resulted material (COF-DhaBad) did not show any crystallinity and the specific surface area was much lower (447 m^2/g). The microscopy analysis of the COF-DhaBad revealed the presence of hollow microspheres with shells consisted of smaller particles rather than a continuous phase like in COF-DhaTab. Therefore, the formation mechanism might be slightly different from the original Ostwald ripening. However, no further analysis and discussion was reported for COF-DhaBad. Nonetheless, the COF-DhaTab is the first mesoporous and chemical stable COF structure reported in literature.

Up to date, hollow OPZ nanospheres and microspheres have been synthesized mainly *via* the templated methods, by performing the usual substitution reaction of HCCP and a multi-functional nucleophile, in the presence of particles such as $CaCO_3$[18],[19], SiO_2[20], and polystyrene latex[21]. A subsequent dissolution of the template by chemical treatment (HCl, HF, THF *etc.*) resulted to hollow OPZ nanospheres of various shell thickness and interior

sizes. Recently, an interesting soft-templated method was reported by Chen et al. who utilized an amphiphilic supramolecular structure[22] as a template for the synthesis of hollow polymeric microspheres.[23] A vesicle was initially formed through a proton-transfer hydrogen bonding between Et$_3$N and *4,4'*-thiobisbensenthiol (MPS) in MeCN. Then, in autoclave conditions, a substitution reaction between HCCP and p-phenylenediamine in the presence of the vesicles solution, resulted to the formation of hollow OPZ microspheres as shown in **Scheme 3.2**.

Scheme 3.2 Soft-templated synthesis of hollow OPZ microspheres. Initial vesicles are formed via a proton-transfer hydrogen bonding interactions.[23]

The same research group has also reported a non-templated method for the production of hollow bowl-shaped microspheres of poly(cyclotriphospazene - *co* - phloroglucinol) (PCP**PG**).[24] In that work, dense PCP**PG** microspheres were initially synthesized by performing the substitution reaction between HCCP and phloroglucinol in acetonitrile (MeCN). In a second step, the PCP**PG** microspheres were washed with acetone for various time periods and resulted in the dissolution of the core and the formation of bowl-like PCP**PG** microspheres. The same result was observed when the dense PCP**PG**s were treated with ethanol, THF and DMF, except in the case of water or MeCN where the PCP**PG**s found unchanged after the same period of treatment.[25] The post-formation of the hollow particles

was explained by assuming the dissolution of the small colloidal micelles consisted of low polymerization degree oligomers in the solvents. In addition, some surface structural defects were believed to play a crucial role as the "gates" for the oligomers escape.

3.2 Aim of the Chapter

As discussed in **Chapter 2**, the morphology of the OPZ 3D materials (spheres, tubes *etc*.) is highly dependent on the reaction parameters, namely, solvent and organic base type, concentration and molar ratio of the building blocks. During this project, single-hole PCP**BS** nanospheres were detected when the usual HCCP-BPS reaction - described in **Chapter 2**- was performed in MeCN-H_2O solutions. In order to investigate the profound mechanisms behind this phenomenon, a comprehensive testing of the reaction under various synthetic conditions with two different co-building blocks was performed, and the morphologies of the particles were observed by electron microscopy. This study will also address a general substitution mechanism between HCCP and multi-functional aromatic nucleophiles along with the transformation mechanism from dense to monoporous nanospheres, and finally capsules to hemispheres. This study aims to reveal more details of the reaction mechanism described in **Chapter 2** and contribute to the understanding of organophosphazene chemistry for the synthesis of phoshazene-based cyclomatrix materials.

3.3 Experimental

3.3.1 Materials

Phosphonitrilic chloride 99% (HCCP, Sigma-Aldrich), *4,4'*-sulphonildiphenol 98% (BPS, Sigma), *1,3,5*-trihydroxybenzene 99% (phloroglucinol, PG, Sigma-Aldrich), triethylamine $\geq$ 99% (Et$_3$N), acetonitrile (MeCN) and acetone were used as received. Acetone and deionized water were used for the purification of the products.

3.3.2 Synthesis of Poly (cyclotriphosphazene-*co*-Bisphenol S) in MeCN-H$_2$O (AqPCPBS)

A MeCN/H$_2$O mixture was used as solvent for the synthesis of hollow poly (cyclotriphosphazene-*co*-Bisphenol S) nanospheres (AqPCP**BS**). In a typical experiment, HCCP (17 mg, 4.9 × 10^{-5} mol) and BPS (38 mg, 1.52 × 10^{-4} mol) were dissolved by sonication in MeCN of different volumes and then water was added up to a total volume of 15 mL. Under continuous sonication, Et$_3$N (0.5 mL, 3.9 mmol) was added instantly with a syringe and the solution appearance changed gradually from transparent to turbid. The vial was removed from the bath after 10 minutes of continuous sonication and the particles were collected by centrifugation (8000 rpm, 5 min), washed three times with acetone and dried *in vacuo* at 50 °C for 24 hours. The same procedure was performed for the synthesis of phloroglucinol-based cyclomatrix organophosphazene hollow particles (AqPCP**PG**) except that MeCN was used for the washing step. In this series of experiments, 19 mg (1.52 × 10^{-4} mol) of phloroglucinol were used, thus keeping the same molar ratio of the nucleophile to HCCP (MR) at 3.1, as with the AqPCP**BS**. Finally, for the sake of comparison, PCP**BS** and PCP**PG** particles were synthesized in MeCN under the same synthetic procedure and the conditions are summarized in **Table 3.1**.

Table 3.1 Reaction conditions for the synthesis of AqPCPBS.

Sample	MeCN (mL)	H$_2$O (mL)	Size (nm)	Yield %
AqPCP**BS**-1	14	1	570 ± 45	31
AqPCP**BS** -2	13	2	705 ± 35	25
AqPCP**BS** -3	12	3	740 ± 40	21
AqPCP**BS** -4	11	4	670 ± 30	16
AqPCP**BS** -5	10	5	615 ± 60	13
AqPCP**BS** -6	9	6	560 ± 80	9
AqPCP**BS** -7	7.5	7.5	-	6
PCP**BS**	15	-	440 ± 20	74

3.3.3 Large scale synthesis of PCPBS and carbon nanospheres

In order to collect sufficient material for the N_2 sorption analysis, the synthesis of AqPCP**BS**-1 and PCP**BS** nanospheres was repeated in 20-fold scale. Both samples were subjected to carbonisation in a tube furnace at 850 °C under N_2 with a heating rate of 5 °C min $^{-1}$ and an isothermal step at the target temperature for 2 h.

3.4 Characterisation

Field emission gun-scanning electron microscopy (FEG-SEM) was performed on a Zeiss SIGMA SEM. A gold-palladium (AuPd) coating was applied to the samples before observation. The carbonized samples did not require any preparation due to their electrical conductivity nature. Transmission electron microscopy (TEM) micrographs were obtained on JEOL 2000FX electron microscope operated at 200 kV. Thermogravimetric analysis curves were obtained with a Mettler Toledo instrument in the temperature range 25-1000 °C at a heating rate of 10 °C min^{-1} under N_2 gas flow (80 mL min^{-1}). Nitrogen adsorption-desorption isotherms were obtained on a Quadrasorb Evo Analyser (Quantachrome). The specific surface area of the samples was calculated by the Brunauer-Emmett-Teller (B.E.T) equation applied on the linear part of the adsorption branch (0.05-0.30 P/P_0) and the pore size distribution was obtained by the Barrett-Joyner-Halenda (B.J.H) equation applied on the desorption branch data. The specific surface area of the carbonized samples was calculated by the *t*-plot method and the pore size distribution by Nonlocal Density-Functional Theory (NLDFT) and the implementation of 'slit-like pores' model of carbon. The samples were degassed at 150 °C for 19 hours under high vacuum before the measurements were taken. The X-ray diffraction (XRD) patterns were recorded on a Panalytical Empyrean diffractometer with a CoKα radiation source (1.79 Å) operated at 45

kV and 40 mA. FT-IR spectra were recorded on a Bruker Vector-22 infrared spectrometer equipped with an attenuated total reflectance (ATR) accessory.

3.5   Results and Discussion

3.5.1   Nucleation and growth of PCPBS in MeCN-H$_2$O (AqPCPBS): Unprecedented single-step towards hollow structures

In general, linear and cyclic chlorophosphazenes are sensitive to hydrolytic reactions in the presence of water or atmospheric moisture conditions.[26] Especially linear poly(dichlorophosphazene)s need careful storage under inert atmosphere otherwise all the chlorine atoms can be substituted by other more chemically stable groups.[27] In order to investigate the role of water in the synthesis and morphology of cyclomatrix organophosphazenes, the nucleophilic substitution reaction between HCCP and BPS was performed in MeCN-H$_2$O solutions in the presence of Et$_3$N. Initially, PCP**BS** nanospheres were synthesized in MeCN (~ 70 wt% yield) under sonication and with the same building blocks concentration and molar ratio, as for the AqPCP**BS** experiments. The PCP**BS** sample consisted of spherical particles of mean diameter Đ ≈ 440 ± 20 nm along with a few smaller particles (~360 nm and > 200 nm). The particles' surface was relatively smooth and almost all the particles had pits on their surface, as shown in **Figure 3.1 (a)**. The internal dense structure of the PCP**BS** nanospheres is demonstrated by the TEM micrograph which is shown in **Figure 3.1 (b)**. It is clearly seen that, the particles are characterized by a solid structure and no void space or gaps were detected in the core, even when the sample was washed with acetone and water or subjected to carbonization at high temperature (850 °C), as observed in **Figure 3.1 (c)**. From these results it is clear that the HCCP/BPS reaction in MeCN resulted in solid and chemically stable nanospheres only, owing to the high reactivity and non-planar structure of BPS which provided more stable initial nuclei.
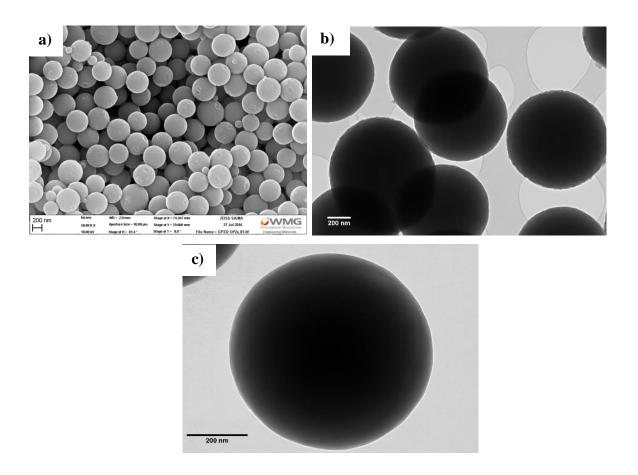
Figure 3.1 a) SEM image of PC**PBS** nanospheres synthesized in MeCN and b) the same sample under TEM observation showing the solid particle structure, c) TEM micrograph of the PC**PBS** after carbonization at 850 °C indicating the transformation of solid OPZ to solid carbon nanospheres.

Compared to the experiments in MeCN, the presence of water had an obvious effect on the reaction time and the mass yield of the samples. With increasing the $VR_{H_2O:MeCN}$ from 1:14 to 6:9, the appearance of turbidity was gradually shifted from 10-30 seconds to approximately 90 seconds for the experiment with the highest water concentration, along with a simultaneous decrease of the mass yield. In all AqPC**PBS** experiments, the $MR_{S:P}$ was kept at 3 and the Et_3N concentration was 3.9 mmol while only the $VR_{H_2O:MeCN}$ was changed.

The morphologies of the AqPC**PBS**s synthesized in MeCN-H_2O solutions were investigated by SEM and the results are shown in **Figure 3.2.** At $VR_{H_2O:MeCN} = 1:14$, sub-micron spherical particles of Đ ≈ 570 ± 45 nm were observed, indicating an increase of the diameter by 150 nm compared to PC**PBS,** and a simultaneously decrease of the mass yield to 35 wt%. A

closer observation of the sample revealed the presence of a single pore/hole ((D ≈ 65 nm) on their surface of, as shown in **Figure 3.2 (b)**.
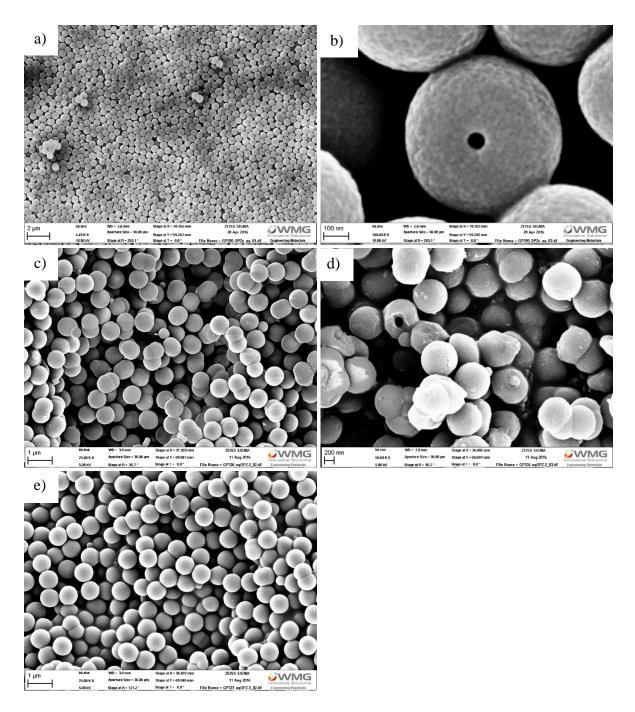
Figure 3.2 SEM images of the a,b) AqPCP**BS**-1, c,d) AqPCP**BS**-2, showing a broken nanosphere and the hollow structure. e) AqPCP**BS**-3 hollow nanospheres synthsised in MeCN/H$_2$O.

The pore/hole was not detected in all the particles because either it was hidden in non-visible planes or did not form during the synthesis. When $VR_{H_2O:MeCN}$ increased to 2:13 and 3:12 (samples AqPCP**BS**-2 and AqPCP**BS**-3) the particle size was further increased to Đ = 705 ± 35 nm and Đ = 740 ± 40, respectively, whilst the yield was slightly further decreased. The surface morphology also showed some differences compared to AqPCP**BS**-1; No pores/holes were observed on the surface while some agglomerated structures consisted of two or more nanospheres appeared, as shown in **Figure 3.2 (c, e)**. This difference indicated that the growth step is highly depended on the water concertation and a possibility of a different growth mechanism is suggested. The hollow core-structure was further confirmed by the presence of broken nanospheres as observed in **Figure 3.2 (d)**.

Moreover, **Figure 3.3 (a-c)** shows that a further increase of $VR_{H_2O:MeCN}$ ratio at 4:11, 5:10 and 6:9, resulted in the formation of AqPCP**BS** capsules with open shells. The occurrence of broken nanospheres and capsules was increased with the water concentration augmentation, while the shell thickness was continuously decreasing. It is highlighted that the term "capsules" is attributed to the appearance of partially inflated-ball structures due to the very thin shells that cannot maintain a mechanical integrity and spherical shape. AqPCP**BS**-7 synthesized at $VR_{H_2O:MeCN}$ = 1:1 did not show the presence of hollow nanospheres or capsules, however, the sample consisted of spherical-shaped random morphologies, as shown in **Figure 3.3 (d)**.
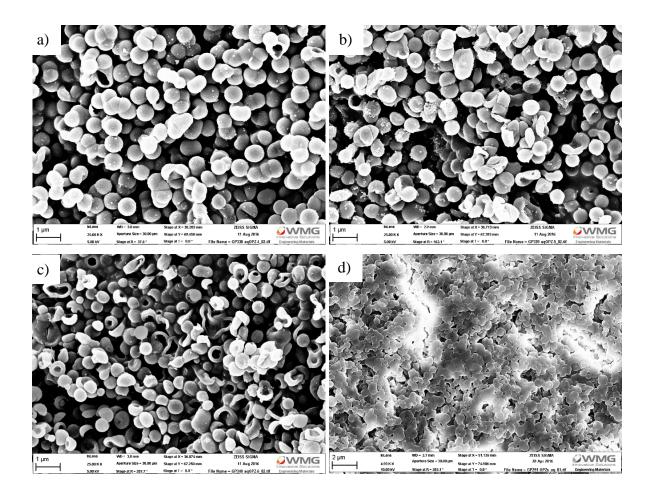
Figure 3.3 SEM images of the a) AqPCP**BS**-4, b) AqPCP**BS**-5, c) AqPCP**BS**-6 hollow nanospheres and nanocapsules synthsised in MeCN-H$_2$O. Magnification 25 k x. d) AqPCP**BS**-7.

Although the AqPCP**BS**-2 did not show any detectable surface pores as described above, an internal hollow structure was observed under TEM examination (**Figure 3.4 (a)**). Some aggregated particles were also present sharing the same hollow core, while their connected shells had a rather continous structure suggesting a reaction between two different particles. The single nanospheres had a shell thickness of aprroximetly 250 nm and hollow cicrcular structures of Đ ≈ 270 nm, while no secondary cavities were detected, as shown in **Figure 3.4 (b).** The AqPCP**BS**-4 also showed the presence of hollow structure with thinner shells of 180 nm and cavity size of Đ ≈450 nm.
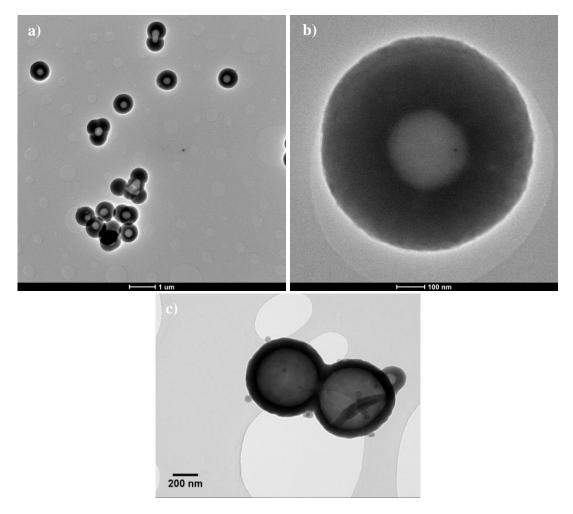
Figure 3.4 TEM micrographs of a, b) AqPC**PBS**-2 and c) AqPC**PBS**-4 hollow nanospheres.

3.5.1.1   Solubility of reactants in MeCN-H$_2$O

At this point, a question about the mechanism behind the hollow structure formation is raised, since no sacrificial template or emulsion system (surfactant) was used. It is important to mention that Hu et al., have reported a pink cloudy solution and the formation of vesicles when Et$_3$N was added to an MeCN solution of tetrahydroxyphenylporphyrin (TPP-(OH)$_4$), before the addition of HCCP.[28] In that work, the *in situ* vesicle formation was provided directly from the co-building block, and not from an external source (sacrificial nucleophile) as described by other groups[23] (see Introduction). To provide a solid answer to the aforementioned question, a series of solubility tests of the reactants was performed; HCCP and BPS, were fully miscible in all range of VR$_{H_2O:MeCN}$ solutions and no phase separation or

emulsion appearance was observed. The addition of Et$_3$N in MeCN/H$_2$O solutions of BPS (without adding HCCP) did not result in cloudy solutions as described before for (TPP-(OH)$_4$), however, a closer examination of the vial revealed a slightly noticeable light scattering. On the other hand the same addition in MeCN-H$_2$O solutions of PG resulted in transparent clear solutions. Next, Et$_3$N was added to MeCN-H$_2$O solution in the absence of BPS, PG or HCCP, and in all cases the solution showed a sense of scattering similar to the solution containing BPS, suggesting that the presence of the other reactants is irrelevant to the observation of scattering which is rather attributed to water clusters surrounded by Et$_3$N.[29] However, this hypothesis was eliminated by the fact that the same scattering observation was detected when Et$_3$N added in net MeCN (no water). The DLS analysis (dynamic light scattering) data of the above solutions were not sufficient enough to provide a solid conclusion, expect that a polymodal size distribution at around 500 nm with a second broad peak at 4 μm was detected. Nonetheless, any speculation of Et$_3$N-water clusters or Et$_3$N-BPS vesicle formation can be eliminated from the fact that the PCP**BS** nanospheres synthesized in MeCN, were solid and no hollow or large pores structures were detected (**Figure 3.1 (b)**). It is also noteworthy to clarify that the absence of scattering in MeCN-H$_2$O/PG/Et$_3$N solutions can be explained by the higher acidity of PG compared to BPS, which decreases the pH of the aqueous solution thus increases the solubility of Et$_3$N. To conclude with, there is no vesicle or other morphology related to the insolubility of the initial reactants and any detected scattering was completely different and significant lower compared to the already published findings.

3.5.1.2 Investigation of insoluble Et$_3$N·HCl crystals formation during reaction

As discussed in **Chapter 2**, the S$_N$2 reaction between HCCP and BPS in the presence of Et$_3$N, produces oligomers which further grow into particles, while the Et$_3$N·HCl is the by-product. The poor solubility of Et$_3$N·HCl in some solvents can induce the formation of stable

nanocrystals. Zhu et al., reported the *in situ* formation of $Et_3N \cdot HCl$ tubular nanocrystals originated from the reaction of HCCP and trace water in acetone. Hollow PCP**BS** microtubes were synthesized by adding BPS and then removing the $Et_3N \cdot HCl$ by washing the sample with water.[30] In the current study, the presence of stable $Et_3N \cdot HCl$ is not anticipated either for the MeCN or MeCN-H_2O solutions and this was confirmed by adding a few drops of aqueous HCl (37% w/w) in MeCN or acetone solutions of Et_3N (**Figure 3.5 (a)**). Indeed, $Et_3N \cdot HCl$ crystals were formed in acetone and were completely disappeared with a subsequent addition of small amount of water, while MeCN solution remained transparent in all stages (**Figure 3.5 (b)**).
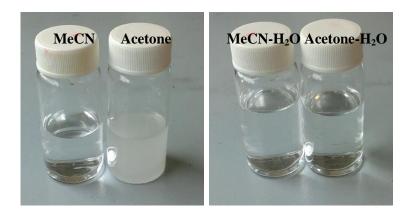
Figure 3.5 Optical images showing the stability behavior of $Et_3N \cdot HCl$ in a) dry and b) aqueous solutions of MeCN and acetone.

To further support the absence of insoluble $Et_3N \cdot HCl$ crystals in the obtained samples, FT-IR and XRD analysis were performed on AqPCP**BS**-4 (randomly selected) prepared in MeCN/H_2O but excluding the washing step. Additionally, AqPCP**BS** samples obtained in acetone or MeCN following Zhu's method (trace water) were prepared and the results are presented in **Figure 3.6**. As it was anticipated, no absorption peaks of aliphatic –CH_3 and –NH^+ were detected in the infrared spectra of the samples prepared in MeCN-H_2O or even in MeCN with trace water. Additionally, the XRD of that samples were in accordance to the

FT-IR results and did not show any presence of hexagonal Et$_3$N·HCl crystals as it was observed for those in acetone or THF[31] solutions.
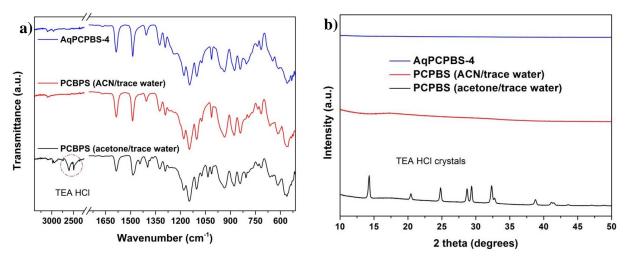
Figure 3.6 a) FT-IR spectra and b) XRD pattern of PCP**BS** samples synthesized in MeCN and acetone aqueous solutions showing the appearance of Et$_3$N ·HCl crystals in each case.

3.5.1.3   The nucleophilic nature of water in the presence of Et$_3$N

Up to this point it can be concluded that the presence of water in acetonitrile is critical in inducing the *in situ* formation of hollow AqPCP**BS** nanospheres and capsules. The results above might suggest a differentiation from the mechanisms of the self-templated hollow OPZs that have been reported so far. According to a study from Vapirov and Zaitzev[32], the hydrolysis of HCCP in MeCN-H$_2$O is negligible, but in the presence of organic bases, such as Et$_3$N, water becomes nucleophilic and induces the substitution reaction as proposed in **Scheme 3.3**.

Scheme 3.3 a) Proposed reaction scheme of water with hexachlorocyclotriphospazene in the presece of Et$_3$N. b) The two tautomers of the complete hydrolized cyclotriophospazene.[32]

In the presence of BPS, a simultaneously hydrolysis of HCCP by water, will reduce the number of available P-Cl bonds and consequently the substitution degree by BPS, which could lead to poor cross-linking of the initial oligomers. In this aspect, water should be considered as a third reactant and in competition against BPS in the reaction system. To investigate the above hypothesis, an experiment was performed by adding Et_3N to a MeCN-H_2O solution of HCCP and treated by sonication for 10 min, before BPS was added. The solution remained transparent even after 1 hour of continuous sonication. This result confirmed that water in the presence of organic base indeed reacted as nucleophile and fully hydrolysed HCCP, so as no further substitution from BPS was possible. Furthermore, the FT-IR spectra of AqPCP**BS** showed that, along with the stretch vibration of P-O-C_{ph} at 936 cm^{-1}, a new peak appeared at 955 cm^{-1} (shoulder) which was associated with the P-O stretch vibrations (**Figure 3.7**). Additionally, the appearance of a peak at 1238 cm^{-1} was associated with the asymmetric P=N ring vibrations[33] which are more evident compared to PCP**BS,** due to the presence of the new P-O bond.
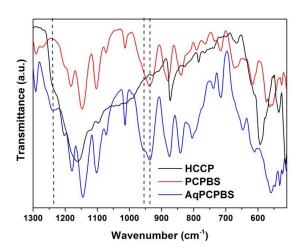
Figure 3.7 FT-IR comparison spectra of HCCP, PCP**BS** and AqPCP**BS** showing the appearance of the new P-O bond.

3.5.1.4   Further investigations: AqPCPBS synthesis under stirring conditions

Due to the synthesis of the AqPCP**BS** under sonication conditions, a reasonable hypothesis of the acoustic cavitation occurrence was raised. The acoustic cavitation has been reported

before for the formation of various hollow nanospheres [34,35,36]. The mechanism is explained by the instant and continuous formation/disappearance of small bubbles in the micron- and nano- range, incurred by the localized high temperature and pressure in a liquid under ultra-sonication conditions.[37] In order to investigate the previous hypothesis of the acoustic cavitation phenomenon, experiments under the same chemical conditions (solvents, concentration, and base) were performed under magnetic stirring with a medium stirring rate in order to avoid vortex and bubbles formation in the solution. The samples AqPCP**BS**-1, AqPCP**BS**-2 and AqPCP**BS**-5 synthesized at 1:14, 2:13 and 5:10 VR$_{H_2O:MeCN}$ respectively, are shown in **Figure 3.8**.
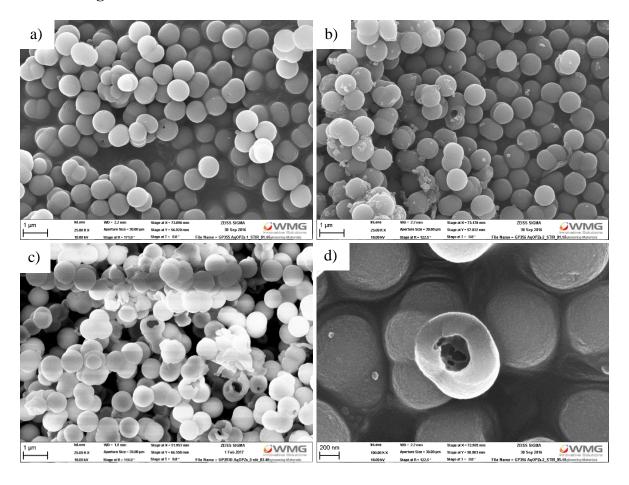
Figure 3.8 SEM images of a) AqPCP**BS**-1, b) AqPCP**BS**-2 and c) AqPCP**BS**-5 hollow nanospheres synthesised in MeCN-H$_2$O under magnetic stirring. Mag. 25 k x. d) Higher magnification (100 k x) of AqPCP**BS**-2, showing a broken hollow sphere.

It is clear that nanospheres with hollow structures were formed also under stirring conditions, thus the possibility of the acoustic cavitation can be disregarded. An increase of 100-150 nm on the particles' diameter was observed only by switching from sonication to stirring, while the size distribution of the dominant particles remained at the same level as with the sonication method. Eventually, the mechanical energy is proved to have negligible contribution on the hollow structure mechanism.

3.5.1.5   Further investigations: AqPCPBS synthesis under sonication in cold bath

The relationship between the particles' morphology and the reaction kinetics of HCCP substitution by BPS and water, were studied by performing the initial sonochemical experiment at low temperature (2 °C). In **Chapter 2**, the particle size – solvent relationship was discussed and the connection with the reaction kinetics was confirmed. In order to observe any possible structural changes, the experiments with high water amounts were chosen as references. The experiment was performed in a vial placed in the sonicator water-bath filled with ice and the MeCN-H_2O solution was left to cool down before any other reactant was added. Under low temperature conditions, the particle formation was observed after up to 1 min of reaction and the solution was less turbid than any other experiment indicating a low precipitation yield. **Figure 3.9** shows a comparison between the AqPCP**BS**-5 synthesized at 25 °C and 2 °C under the same sonochemical conditions.
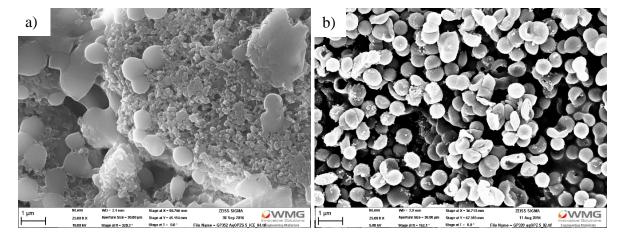
Figure 3.9 SEM images of AqPCP**BS**-5 synthsised at) 2°C and b) 25 °C. Magnification 25 k x.

The topography of the sample synthesized at 2 °C consisted of spherical particles of very high size dispersity and some random undefined structures while no capsules or broken hollow nanospheres were present. A similar topography was observed for the AqPCP**BS**-7 sample prepared at 25 °C (see **Fig. 3.2(d)**). When the synthesis of AqPCP**BS-7** was performed at 2 °C the particle formation was hard to detect and it was impossible to collect any solid sample after centrifugation of the solution. These results, along with the previous discussion, enhance the idea of poor cross-linking degree oligomers with high solubility in the MeCN-H_2O solution. These oligomers form unstable clusters which redissolve in the solution and leave behind a hollow core.

3.5.2   Thermogravimetric analysis

The carbonisation profile of the AqPCP**BS** samples was obtained by the TG analysis at 1000 °C under N_2 and the resulted thermograms are shown in **Figure 3.10**. Likewise solid PCP**BS**, a two-step mass loss behavior was observed for the AqPCP**BS** with an initial decomposition onset temperature located at $T_{on.}1 \approx 480$ °C and a second one at $T_{on}2 \approx 805$ °C.
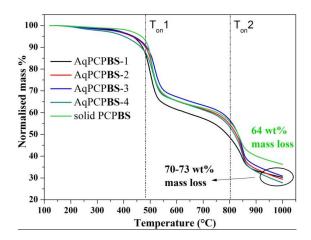
Figure 3.10 TGA thermograms of the AqPCP**BS** hollow and PCP**BS** solid nanospheres.

 The decomposition of the cross-linked structure of the phopshazene-*co*-BPS and its conversion to carbon material is taking place on the first mass loss step along with the loss of

the heteroatoms (P, S, N,O) while a further gasification of the carbon materials resulted to the second mass loss step. The total mass loss calculated at the range 150-1000 °C was 64 wt% for the dense PCP**BS** nanospheres and 70-73 wt% for the AqPCP**BS** samples with the difference mainly emanated from the second mass loss step as the curves at the first mass loss step follow the same pathway. A possible explanation could be given by the less compact and cross-linked structure of the AqPCP**BS** nanospheres which were more unstable at high temperatures compared to solid PCPBS, as well as at to the presence of more oxygen atoms in the AqPCP**BS** structure due to the previous P-O bonds from the reaction with water.

3.5.2.1 Morphological characterization of the carbonized AqPCPBSs TGA traces

The carbon residue material (c-AqPCP**BS**) from the TG analysis was examined by SEM in order to investigate the formation of carbon nanospheres and the representative SEM images are shown in **Figure 3.11**. The c-AqPCP**BS**-1 nanospheres were found slightly shrunken to ~ 540 nm (from 600 nm) and the presence of a broken particle revealed the existence of the initial cavity, as illustrated in **Figure 3.11 (a)**. Many of the particles from the samples (c-AqPCP**BS**-2, 3 and 4) had a "ghost" like appearance under the SEM beam (**Figure 3.11 (b, c)**) due to the thin carbon shells and well-defined hollow-core structures were clearly visible. Nevertheless, not all the particles had this appearance which suggest that either not all the particles are hollow or some of them have thick enough shells for the beam to penetrate. The samples synthesized at high $VR_{H_2O:MeCN}$ solutions were completely decomposed to a hard carbon material with no defined structure (**Figure 3.11 (e, f)**).
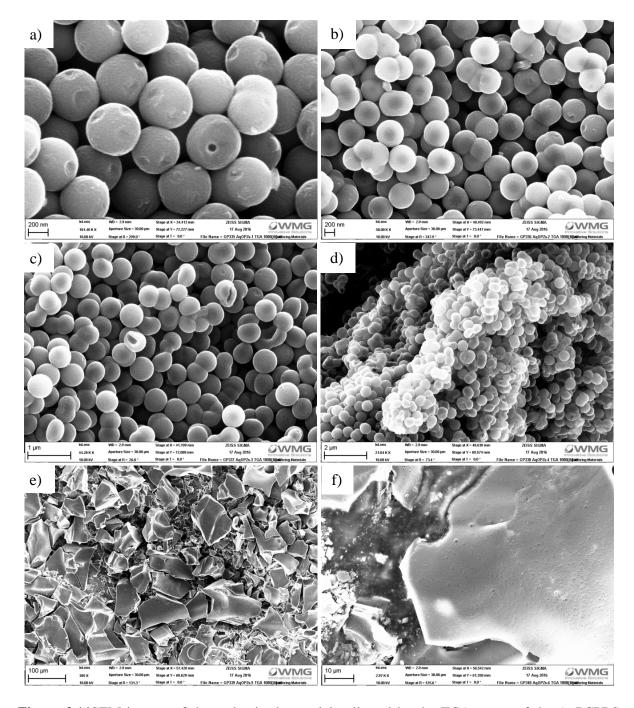
Figure 3.11 SEM images of the carbonized material collected by the TGA traces of the AqPCPBS samples. a) c-AqPCP**BS**-1, b) c-AqPCP**BS**-2, c) c-AqPCP**BS**-3, d) c-AqPCP**BS**-4, e) c-AqPCP**BS**-5 and f) c-AqPCP**BS**-6.

3.5.3 N₂ sorption isotherms

The pore textural properties were analysed through N_2 adsorption - desorption isotherms. The aim of this experiment was to highlight the major differences compared to the dense PCP**BS** nanospheres and not to perform a complete study of the different AqPCP**BS** structures. For

this purpose, the AqPCP**BS**-1 and the derived HCNS-1 nanospheres carbonized at 850 °C were examined and compared to the solid PCP**BS** and CNS nanospheres, respectively. **Figure 3.12 (a)** shows the representative isotherms of the samples before carbonization. Both samples show a Type-II isotherm with a slow N_2 uptake at low relative pressure and a steep increase at 0.95 P/P_0, which is characteristic of non-porous powder materials.
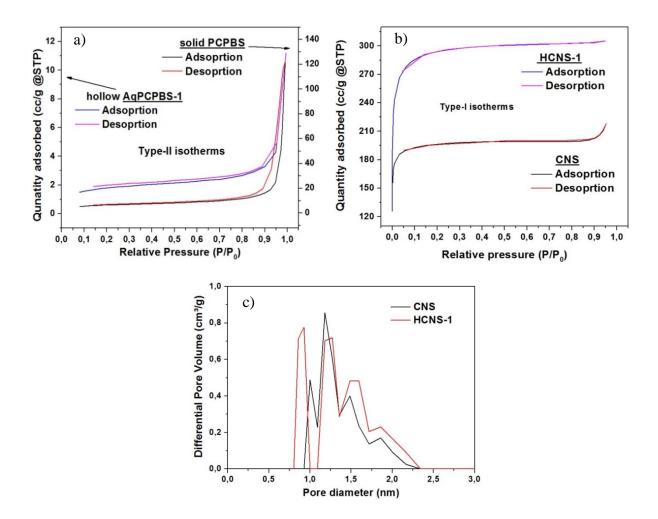
Figure 3.12 N_2 sorption isotherms of the PCP**BS** and AqPCP**BS**-1 a) before and b) after carbonization. c) The DFT pore size distribution of the same samples after carbonization.

The steep N_2 uptake at the saturation pressure (> 0.90 P/P_0) as well as a small hysteresis at the desorption branch, were attributed to the N_2 condensation into the intra-particle free space due to the nanospheres random packaging. A desorption hysteresis originated from the presence of surface single pore, was not detected as its size was larger than the detection ability of the method and mercury porosimetry is suggested. The B.E.T specific surface area

of the PCP**BS** and AqPCP**BS**-1 was 19.2 m^2/g and 6.5 m^2/g, respectively, attributed to the external surface of the particles since the pore size distribution did not show any structural porosity. The lower surface area of the AqPCP**BS**-1 nanospheres was attributed to their increased diameter compared to the much smaller PCP**BS**. For this reason, the contribution of the inner surface cavity was not detectable. After the carbonization of the samples the N$_2$ uptake was significantly increased from the low relative pressures, already. Both isotherms had the typical behavior of microporous materials which was also confirmed by the pore size distribution, showing pores smaller than 2 nm (**Figure 3.12 (c)**). The specific surface area for the CNS was 840 m^2/g and increased to 1156 m^2/g for the sample prepared in MeCN-H$_2$O. The de Boer t-plot method showed that the high specific area was mainly originated from the micropores surface which was calculated at 740 m^2/g and 1000 m^2/g for CNS and HCNS-1, respectively. Furthermore, the DFT pore size distribution showed the shifting of the pores to smaller diameters indicating that the water had an important role in the internal and chemical structure of the organophosphazene shell.

3.5.4 Synthesis of poly (cyclophospazene-*co*-phloroglusinol) submicron capsules in MeCN-H$_2$O (AqPCPPG)

In order to investigate the versatility of the synthetic route, a series of experiments were performed by selecting PG as the co-building block. In contrast to the bi-functional and non-planar BPS, PG is also a strong nucleophile but with a planar structure which comprises one benzene ring and three phenol groups as shown in **Scheme 3.4**.

Scheme 3.4 Chemical structure of a) PG and b) BPS.

The synthetic conditions (dispersion method, concentrations, building blocks ratio and base type) were kept the same as for the synthesis of hollow AqPCP**BS** nanospheres and a control experiment was also performed where PCP**PG** nanospheres were prepared in MeCN; a much slower particle formation rate and lower mass yield were observed for the reactions in both MeCN-H_2O and dry MeCN as compared to the BPS experiments. Consequently, it is anticipated that the HCCP-PG oligomers formed in MeCN-H_2O solutions will have low cross-linking degree and less stable initial nuclei. Another significant observation was the appearance of a purple colour during the reaction which its intensity increased with increasing amounts of water as shown in **Figure 3.13**. It is known that PG·HCl is used as a dye for the lignin detection in plants since it displays a red-violet colour upon reaction.[38] Here, the appearance of colour could be explained as follows; water promotes the solubilisation of Et_3N·HCl to afford free HCl acid which subsequently reacts with the phosphazene –PG oligomers resulting into a coloured supernatant solution. It is also important to highlight that the obtained AqPCP**PG** particles did not show any colour indication enhancing this way the hypothesis of a self-templated mechanism for the hollow structure formation. Moreover, such phenomenon was not observed for the supernatant solutions of the AqPCP**BS** experiments since BPS is not acting as a dye like PG.

Figure 3.13 Optical image showing the appearance of a purple color from PG·HCl in the AqPCPPG experiments with increasing amounts of water (from left to right).

3.5.4.1 Morphological characterization of AqPCPPG and PCPPG microspheres

In MeCN, PCP**PG** microspheres of Đ = 1 ~ 3 µm were obtained and the presence of some broken microspheres showed a cavitated core (**Figure 3.14**). As previously discussed, for the PCP**PG** microspheres, the hollow structure was formed *ex situ* and during the washing step with acetone.[24] Correspondingly, when dense PCP**BS** nanospheres were washed with acetone, no change of the core structure was observed. This result indicated that the initial formed oligomers and nuclei are chemically stable towards acetone when BPS is used as a co-linker to phosphazene. On the contrary, the same species formed by the reaction of PG with HCCP are less stable and can be solvated in acetone resulting in hollow structures. The increased solubility of the HCCP-PG oligomers in acetone could be due to the similarity of their structure (planar) which may provide less random cross-linking compared to HCCP-BPS oligomers, thus more unstable material.
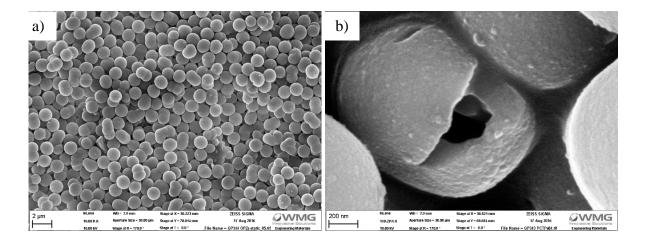
Figure 3.14 SEM iamges of PCP**PG** synthsized in pure acetonitrile; a) 10k x magnification and b) an opened PCPPG microsphere reaveling the hollow structure at 100 k x magnification.

Figure 3.15 shows the morphology of the AqPCP**PG**-1 after washing with acetone. Compared to AqPCP**BS**-1, the topography of the sample consisted of sub-micron capsules with very thin and open shells which had the appearance of inflated balls as well as some semi-shells and amorphous areas (raw material). The thin shells induced diversity in the

morphology, which made the measurement of the diameter size difficult; however, some spherical capsules were measured at ~ 550 nm. Surprisingly, when AqPCP**PG**-2 microspheres were washed with acetone -after the synthesis- the solution almost instantly became transparent, indicated that all the formed structures were dissolved.
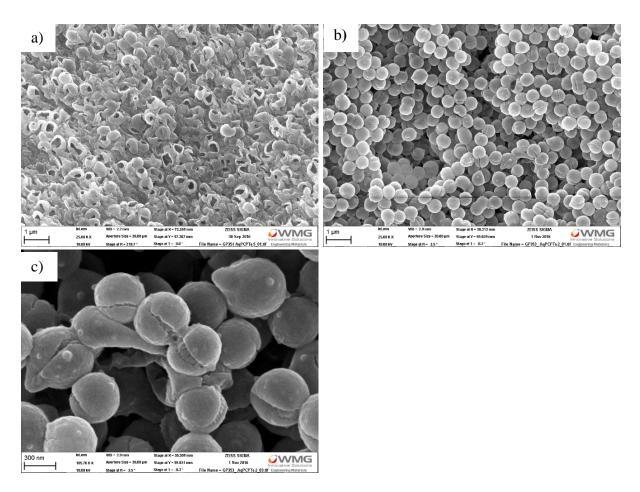
Figure 3.15 SEM images of a) AqPCP**PG**-1 after washing with acetone and b) AqPCP**PG**-2 after washing with MeCN only. Mag. 25 k x. c) AqPCP**PG**-2 at mag. 100 k x.

The same observation was recorded for all the experiments with $VR_{H_2O:MeCN}$ = 2:13 or higher an only AqPCP**PG-1** was stable. In order to study the structure of AqPCP**PG**-2, the sample was washed only with MeCN after the synthesis. In this attempt, nanospheres of ~ 550 nm were obtained and almost all the particles had cracks located on the equator of the nanospheres (**Figure 3.15 (a)**). Meanwhile, no evident hollow structures were observed and instead, some material with different texture to the surface was detected as a "filler" of the core structure (**Figure 3.15 (b)**). It is important to highlight that the smaller size of the

AqPCP**PG** compared to the PCP**PG**, is in contrast to what was observed for the PCP**BS** and AqPCP**BS** where in that case the water induced an increase of the mean particle size.

At higher water concentrations only hollow spherical capsules structures were predominant. More specifically, AqPCP**PG**-3 consisted of spherical particles of D> 600 nm and the holes on the shells of various sizes (**Figure 3.16 (a)**). At $VR_{H_2O:MeCN}$ = 4:11 (AqPCP**PG**-4) two different morphologies were present in a mixed order: semi-shells of ~ 600 nm and capsules of <300 nm with fine shells, as shown in **Figure 3.16 (b)**. This result indicated that at higher $VR_{H_2O:MeCN}$ the particle formation took place at two different stages. Similar morphologies were observed for the AqPCC**PG**-5; however, the semi-shells were more evident with large opening and their topography suggested a honeycomb structure. The topography examination showed the presence of a second family of small capsules which were located at different areas of the sample and not as a mixture like in AqPCP**PG**-4 (**Figure 3.16 (c, d)**).
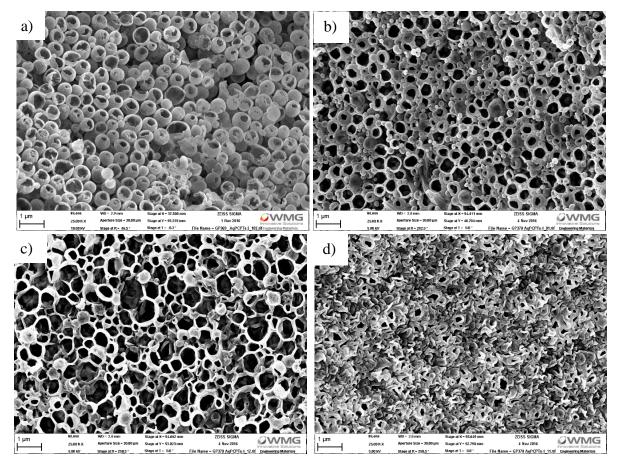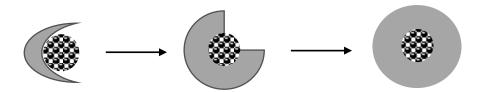
Figure 3.16 SEM images of a) AqPCP**PG**-3, b) AqPCP**PG**-4 and c, d) AqPCP**PG**- 5. Mag. 25 k x.

3.6 Proposed self-template-direct mechanism

The results of this work along with the previously reported publications suggest that the formation of hollow cyclomatrix organophosphazene nanospheres in MeCN-H_2O solutions follows a complicated mechanism of self-template-direct formation instead of the Ostwald ripening, since either no crystals structures were present in OPZs or mass diffusion through the shell and self-growth was realised. Here, the hydrolyzed and poorly cross-linked initial HCCP-BPS oligomers form unstable primary nucleation clusters where growth takes place. A simultaneous *in situ* dissolution of the clusters along with the inner-wall degradation, lead to the formation of hollow spherical particles. In parallel, the presence of aggregated particles with shared and diffused cores suggests a shell growth evolution mechanism from crescent-shaped structures to open hemispheres and finally complete spherical structures. A similar mechanism has been reported before for the synthesis of silica hollow spheres with a precipitation-phase separation method,[39] in the presence of surfactant of water-ethanol mixtures,[40] or in polystyrene monoporous microspheres synthesized under microwave conditions.[41] A schematic representation of the shell and final sphere evolution is shown in **Scheme 3.5**.

Scheme 3.5 Proposed self-template-direct mechanism

3.7   Conclusions

Continued from **Chapter 2**, another factor related to the effect of the solvent in the reaction between HCCP and BPS was presented. Here, hollow cyclomatrix organophosphazene nanospheres were successfully prepared in mixtures of MeCN-H$_2$O solutions without the need of a sacrificial template. The presence of water was proved to be an important factor on the reaction kinetics and consequently the final morphology of the samples. At VR$_{H_2O:MeCN}$ = 1:14 monoporous spherical particles were formed while at higher VR$_{H_2O:MeCN}$ hollow and open-shell capsules started to form. The BPS-contained samples showed good chemical stability towards acetone, while the PG-contained samples were unstable showing thus showing the importance of the nucleophile structure on the integrity of the particles and shells. A simplified overview of the major findings of this study is given in **Table 3.2**. The investigation of the reaction parameters showed that the particular self-templated mechanism is unique for this category of materials since it is not following exactly the already reported methods. Here, a combination of self-formed clusters consist of hydrolysed oligomers and a continuous dissolution of the inner wall of the particles, takes place simultaneously, therefore a self-template-direct formation of the hollow organophosphazenes is proposed.

Table 3.2 The structural stability of OPZs in MeCN, acetone and their aqueous solutions.

Solvent and washing	Bisphenol S	Phloroglucinol
MeCN	Solid	Solid
Washed with acetone	Solid	Hollow
MeCN-H$_2$O	Hollow	Hollow
Washed with acetone	Hollow	Unstable

A careful examination of electron microscopy micrographs suggested an evolution of particles growth from crescent structures to hollow spheres. The thermal stability of the AqPCP**BS** led to the formation of hollow carbon nanospheres under pyrolysis conditions. Thus, this method could be utilised for an easy and facile production of nanostructured carbon materials for the needs of electrical energy storage applications, as discussed in **Chapter 4**.

Finally, the results of this Chapter shade more light on the understanding of the factors govern the basic chemical reaction as described in **Chapter 2**. It was shown that by controlling these factors, more sophisticated structures can be obtained expanding this way the potential of the organophosphazene chemistry.

3.8   References

1.   M. A. Mahmoud, D. O'Neil and M. A. El-Sayed, *Chemistry of Materials*, 2014, **26**, 44-58.

2.   C. E. Mora-Huertas, H. Fessi and A. Elaissari, *Int J Pharm*, 2010, **385**, 113-142.

3.   L. Zhou, Z. Zhuang, H. Zhao, M. Lin, D. Zhao and L. Mai, *Adv Mater*, 2017, DOI: 10.1002/adma.201602914.

4.   J.-H. Lee, *Sensors and Actuators B: Chemical*, 2009, **140**, 319-336.

5.   X. Wang, J. Feng, Y. Bai, Q. Zhang and Y. Yin, *Chemical reviews*, 2016, **116**, 10983-11060.

6.   W. H. Suh, A. R. Jang, Y. H. Suh and K. S. Suslick, *Advanced Materials*, 2006, **18**, 1832-1837.

7.   F. Liang, J. Liu, C. Zhang, X. Qu, J. Li and Z. Yang, *Chemical communications*, 2011, **47**, 1231-1233.

8.   M. Mandal Goswami, *Scientific reports*, 2016, **6**, 35721.
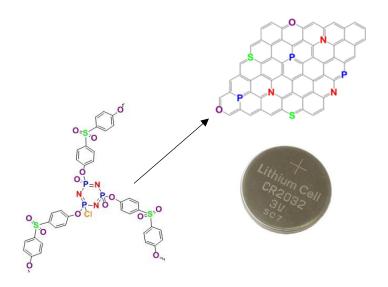
9.   M. Mozafari, F. Moztarzadeh, A. M. Seifalian and L. Tayebi, *Journal of Luminescence*, 2013, **133**, 188-193.

10.   H. Chun Zeng, *Current Nanoscience*, 2007, **3**, 177-181.

11.   Y. Yin, R. M. Rioux, C. K. Erdonmez, S. Hughes, G. A. Somorjai and A. P. Alivisatos, *Science*, 2004, **304**, 711-714.

12.   M. H. Oh, T. Yu, S. H. Yu, B. Lim, K. T. Ko, M. G. Willinger, D. H. Seo, B. H. Kim, M. G. Cho, J. H. Park, K. Kang, Y. E. Sung, N. Pinna and T. Hyeon, *Science*, 2013, **340**, 964-968.

13.   H. C. Zeng, *Journal of Materials Chemistry*, 2011, **21**, 7511.

14.   S. Jung, W. Cho, H. J. Lee and M. Oh, *Angewandte Chemie*, 2009, **48**, 1459-1462.

15.   J. Huo, L. Wang, E. Irran, H. Yu, J. Gao, D. Fan, B. Li, J. Wang, W. Ding, A. M. Amin, C. Li and L. Ma, *Angewandte Chemie*, 2010, **49**, 9237-9241.

16.   S. Kandambeth, V. Venkatesh, D. B. Shinde, S. Kumari, A. Halder, S. Verma and R. Banerjee, *Nature communications*, 2015, **6**, 6786.

17.   A. Carne-Sanchez, I. Imaz, K. C. Stylianou and D. Maspoch, *Chemistry*, 2014, **20**, 5192-5201.

18.   W. Liu, X. Huang, H. Wei, K. Chen, J. Gao and X. Tang, *Journal of Materials Chemistry*, 2011, **21**, 12964.

19.   F. Chang, X. Huang, H. Wei, K. Chen, C. Shan and X. Tang, *Materials Letters*, 2014, **125**, 128-131.

20.   L. Sun, T. Liu, H. Li, L. Yang, L. Meng, Q. Lu and J. Long, *ACS applied materials & interfaces*, 2015, **7**, 4990-4997.

21.   X. Wang, J. Fu, Z. Chen, Q. Li, X. Wu and Q. Xu, *RSC Advances*, 2015, **5**, 33720-33728.

22.   C. Shan, X. Huang, H. Wei, W. Wei, H. Sun and X. Tang, *RSC Advances*, 2014, **4**, 11216-11218.

23.   K. Chen, X. Huang, C. Wan and H. Liu, *Electrochimica Acta*, 2016, **222**, 543-550.

24.   T. Pan, X. Huang, H. Wei and X. Tang, *Macromolecular Chemistry and Physics*, 2012, **213**, 2606-2610.

25.   T. Pan, X. Huang, H. Wei, W. Wei and X. Tang, *Macromolecular Chemistry and Physics*, 2012, **213**, 1590-1595.

26.   H. R. Allcock, J. E. Gardner and K. M. Smeltz, *Macromolecules*, 1975, **8**, 36-42.

27.   D. G. Gabler and J. F. Haw, *Macromolecules*, 1991, **24**, 4218-4220.

28.   Y. Hu, L. Meng and Q. Lu, *Langmuir : the ACS journal of surfaces and colloids*, 2014, **30**, 4458-4464.

29.   M. A. Muñoz, C. Carmona and M. Balón, *Chemical Physics*, 2007, **335**, 37-42.

30.   L. Zhu, X. Huang and X. Tang, *Macromolecular Materials and Engineering*, 2006, **291**, 714-719.

31.   L. Zhu, Y. Xu, W. Yuan, J. Xi, X. Huang, X. Tang and S. Zheng, *Advanced Materials*, 2006, **18**, 2997-3000.

32.   V. V. Vapirov and D. O. Zaitsev, *Russian Journal of General Chemistry*, 2006, **76**, 1232-1235.

33.   A. Sassi, R. Milani, A. Venzo and M. Gleria, *Designed Monomers and Polymers*, 2006, **9**, 627-647.

34.   R. K. Rana, Y. Mastai and A. Gedanken, *Advanced Materials*, 2002, **14**, 1414-1418.

35.   I. Uzcanga, I. Bezverkhyy, P. Afanasiev, C. Scott and M. Vrinat, *Chemistry of Materials*, 2005, **17**, 3575-3577.

36.   C. Deng, H. Hu, X. Ge, C. Han, D. Zhao and G. Shao, *Ultrasonics Sonochemistry*, 2011, **18**, 932-937.

37.   K. S. Suslick, Y. Didenko, M. M. Fang, T. Hyeon, K. J. Kolbeck, W. B. McNamara, M. M. Mdleleni and M. Wong, *Philosophical Transactions of the Royal Society A: Mathematical, Physical and Engineering Sciences*, 1999, **357**, 335-353.

38.   E. O. Speer, *Stain Technol*, 1987, **62**, 279-280.

39.   X. Fu, X. He and X. Hu, *Colloids and Surfaces A: Physicochemical and Engineering Aspects*, 2012, **396**, 283-291.

40.   H. Zhang, J. Wu, L. Zhou, D. Zhang and L. Qi, *Langmuir : the ACS journal of surfaces and colloids*, 2007, **23**, 1107-1113.

41.   M. Q. Zhu, G. C. Chen, Y. M. Li, J. B. Fan, M. F. Zhu and Z. Tang, *Nanoscale*, 2011, **3**, 4608-4612.

Chapter 4 Ternary-heteroatom-doped carbon nanospheres: Synthesis, characterisation and electrochemical performance in Li-ion batteries

Long cycle performance is a crucial requirement in energy storage devices. New formulations and/or improvement of "conventional" materials have been investigated in order to achieve this target. Here, ternary-heteroatom-doped carbon nanospheres (CNS) obtained from the carbonisation of cyclomatrix OPZ nanospheres at 700, 850 and 1000 ° are tested as anodes in Li-ion half-cells. A detailed characterisation of the carbon structure doped with O, N, P and S, showed an evolution of doping at% with temperature which not only affected the specific surface area of the CNS, but also had an impact in the specific capacity of the electrodes. The XPS analysis showed high at% of pyridinic-N species for the CNS-850 which demonstrated a remarkable stability and Coulombic efficiency (99.9999 %) in a long charge–discharge cycling up to 1100 cycles, delivering 130 mA h g^{-1} at high current rate of 1C. The combination of high surface area with abundant micropores for the Li storage along with the multiple-doping, proved to be important for the performance of these materials as electrodes in energy storage applications. Part of the results here were published under the title: Heteroatom Doped-Carbon Nanospheres as Anodes in Lithium Ion Batteries.[1]

4.1 Introduction

4.1.1 Synthesis of porous hard carbon nanospheres

The term carbon spheres (CS) refers to micron and sub-micron sized particles which have solid, core-shell or hollow structures and are mainly prepared by carbonisation of aromatic-based polymers which are thermally stable and are able to form carbon residue after high-temperature treatment under inert atmosphere. Chemical vapour deposition (CVD), hydrothermal carbonisation, and pyrolysis of organic/polymer spherical particles are the main synthetic routs, while Friedel - Crafts reaction and the Stöber method have also been reported recently. The carbon sources cover a wide range of precursors such as carbon-containing gases, phenolic resins, poly (furfuryl alcohol), sugars, biomass, cyclodextrins, and resorcinol-formaldehyde are some examples that can be found in some recent reviews on the field.[2, 3] Various surfactants, block-copolymers, hard and soft templates can be also employed in combination with the precursors to modify the size/porosity of CS and to generate nano-engineered architectures.[4]

In the same manner heteroatom-doped CS are obtained by selecting the appropriate heteroatom-contained monomer. The most reported kind of such CS is the nitrogen-doped CS due to the large availability of N-containing monomers (aniline, pyrrole, dopamine, melamine *etc*.), low cost and easy synthesis. The last years an increasing interest driven by the developments ORR carbon catalysts[5] and, Li-S and Na-ion batteries, has been noticed for the synthesis of sulphur-doped carbon materials. The presence of S lowers the band gap and brings the positive charge towards the C atoms thus increasing their redox reactivity.[6] Additionally, the large atomic radius induces distortion in the carbon network giving rise to nano-microporosity and interlayer spacing between graphene sheets.[7] Although, many

publication have been reported for S-doped sp^2 carbons and hard carbon materials, the reports for S-doped CSs are rare and are based on post S-doping of the material.[8, 9]

The one-step synthesis of highly cross-linked cyclomatrix organophosphazenes (OPZs) and their unique molecular-level hybrid structure, is an excellent and highly efficient method to prepare intrinsic multi-heteroatom doped carbons, such as various micro- nanospheres, nanotubes, core-shell and hollow particles. Phosphazene provides the P and N doping while, the desired co-dopants (O, S, F, etc.) can be selected by the appropriate co-building block, as shown in **Table 2.1** (see Introduction of Chapter 2). The presence of multiple heteroatoms in the carbon structure alter the electronic properties of the carbon material and at the same time induce microporosity by escaping the carbon structure as part of the gasification during pyrolysis[10]. The ambient conditions, the fast rate of reaction and the low cost are the main advantages of this synthetic method. This intrinsic presence of multi-heteroatoms in the precursor carbon source the OPZ is the key to stand out the carbons derived from OPZ precursors, from the rest reported methods. In the **Table 4.1**, a brief list of OPZ-derived carbons and their main characteristics are presented.

Table 4.1 Heteroatom-doped carbon materials derived from OPZs and their applications.

Carbon Structure	Co-building block	Doping	Application/Properties	Ref
Metal decorated Nanotubes	BPS	P,N,S	ORR catalyst	[11]
Microporous hollow nanospheres	BPS	P,N,S	Macroporous/microporous structure	[12]
Metal-decorated hollow nanospheres	ODA	P,N	Fire retardant	[13]
Mesoporous nanospheres	BPS	P,N,S	H$_2$ storage	[14]

4.1.2 Porous carbon nanospheres as anodes in Li-ion batteries

Carbon nanospheres (CNS) of high surface area, porosity and electrical conductivity, have been demonstrated as active materials in various energy storage and conversion applications such as alkali metal-ion batteries[15-17], supercapacitors[18-21], catalysis[5, 22-24] and hydrogen storage cells. [25, 26] As regards the LIBs, the last years research attention has turned to carbons as supportive coatings in Li-alloy-core/carbon-shell structures, in order to limit the main issues of the alloy anodes namely, pulverization and low electrical conductivity.[27, 28] In this aspect, porous carbon shells provide enhanced electrical conductivity and connectivity with the binder and the current collector, improve the wettability of the anode/electrolyte while at the same time act as buffer to accommodate the volume changes of the active material during lithiation/ delithiation.[29, 30] Nevertheless, alloy-free disordered carbon electrodes are still attractive owing to their porous structure which gives rise to high theoretical capacity (nominal composition Li_xC_6, $2 < x < 3$)[31], the long term cycling stability due to negligible volume changes, and the low cost and weight, thus an attempt to replace graphite in conventional LIBs is ongoing.[2] In the 90's some initial studies showed that the lithiation process in hard carbons significantly differentiated from the intercalation mechanism of graphitic (soft carbon) materials. The works from Sato[32] and Dahn[33] showed that the increased Li storage in disordered hard carbons was attributed to: i) the increased graphene sheet interlayer spacing ii) occupation of both sides of single layer graphene and defected sites and iii) insertion of solvated Li^+ ions ducted through the mesopores and stored in the narrow micropores forming Li clusters.

In order to further increase the storage capacity and shorten the pathway length of Li^+ diffusion, many groups have explored more sophisticated structures such as hierarchically porous and hollow CNS and doped CNS. Hierarchically porous CNS with single or even

double hollow architecture are prepared via a hard template method followed by chemical etching of the inorganic template. Compared to the dense CNS, the hollow CNS provide extra surface for the lithium accommodation thus increased gravimetric specific capacity but at the same time lower volumetric energy density, a significant parameter for most of the LIBs applications.[34] Apart from the multistep synthesis methodology the major issue of these engineered CNS is the high irreversible capacity loss at the first electrochemical cycle and the initial low Culombic efficiency. However, scientists have been able to achieve remarkable electrochemical performance in some cases of hollow CNS, showing this way the potential of these materials for the future developments. Zhang et al., prepared double shelled N-doped CNS and showed their better electrochemical performance than the un-doped nanospheres when tested both in lithium ion and sodium ion cell.[35] Xiao et al., synthesized hydrogenated CNS[36] by a low temperature solvothermal method using chloroform ($CHCl_3$) as carbon source and compared to other work[37] with similar CNS textural characteristics (particle size and specific area), the H-doped CNS showed enhanced discharge capacity due to Li-H binding. These examples show that not only the control over the textural structure but also the substitution of carbon by heteroatoms has a significantly positive effect in the performance of carbon materials in LIBs. Some recent development of porous doped-CNS as anodes in LIBs is summarized in **Table 4.2**. It is noteworthy to mention that the hard carbon materials shown below, outperform the theoretical gravimetric capacity of graphite since they provide more lithiation sites rather the single intercalation process which is characteristic of the pure graphitic materials.

Table 4.2 Recent highlights in porous N-doped CNS as anodes in LIBs.

Structure	Carbon source	Electrochemical performance	Ref
Macro-mesoporous hollow spheres	dopamine	530 mA h g^{-1} @ 2.5 A g^{-1}/1000 cycles	[38]
Double-shelled hollow spheres	glycose	512 mA h g^{-1} @ 1.5 C /500 cycles	[35]
Mesoporous hollow spheres	pitch	616 mA h g^{-1}@ 0.5 A g^{-1} / 250 cycles	[39]
Hollow nanoflowers	dopamine	528 mA h g^{-1} @ 2C/1000 cycles	[40]
Hollow nanospheres	ZIF-8	879 mA h g^{-1}@ 5 A g^{-1} / 1000 cycles	[41]
Graphite (theor.)		372 mA h g^{-1}	

4.1.3 Organophosphazene-derived carbons in energy storage applications

Multi-heteroatom-doped microporous CNS prepared by pyrolysis of their organophosphazene precursors have been applied as electrode materials in supercapacitor and LIBs electrochemical cells. The first related work in LIBs was released in 2009 by Gao et al, who applied a thin (~10 nm) microporous carbon coating on Si nanoparticles (50-100 nm) in order to deal with the usual volume expansion issues of Si during Li charge/discharge cycles. The obtained C@Si test in Li-ion half cells and achieved a discharge capacity of 1200 mA h g^{-1} at 0.5C over 40 cycles.[42] The same organophosphazene approach was also adopted by others; Xue et al. achieved a performance of 700 mA h g^{-1} at 100 mA g^{-1} after 40 cycles in a C@Si-MWCNTs system[43] and Caili et al. reported for C@Si, a discharge capacity of 740 mA h g^{-1} at 0.05C after 100 cycles.[44] In these reports, different sizes of Si nanoparticles and electrode formulations were utilized and on top of that, the differences on the electrochemical testing parameters would make a straightforward comparison unfair. Nevertheless, the applied OPZ-derived carbon coating had a positive effect on the Si performance, although the limited cycling test can give only some indication about the electrochemical properties of the materials, but fail to extract a solid result valuable for real applications.

As for the application of OPZ-derived carbons in metal-free supercapacitors, three types of morphologies have been reported so far; microporous microspheres[45], microporous hollow microspheres[46] and mesoporous carbon nanofibers.[47] The reported capacitance reached values up to 316 F g^{-1} at current rate of 0.2A g^{-1} thus placing these materials among the carbon candidates for EDLCs (electric double layer capacitors). Moreover, Wei et al., carbonised PC**PBS** nanospheres in order to prepare microporous Mn$_2$O/CNS by a chemical co-precipitation method and a relatively high specific capacitance of 3.13 F cm^{-2} was reported.[48] In the above attempts, the long cycle stability and high specific capacitances were attributed to the high surface area, meso- microporous structure and high level of heteroatom doping.

4.2   Aim of this Chapter

Herein, a comprehensive characterisation of CNS obtained after carbonisation of PC**PBS** nanospheres at various temperatures is presented. The motivation was based on the need to of understanding the intrinsic multi-heteroatom-doped and microporous carbon structure and the electrochemical evaluation of these CNS as anodes in Li-ion half cells as it was never reported before. The aim of this Chapter is to provide a solid description of the CNS structure and highlight the preliminary results of their electrochemical properties and how they are affected by the textural and chemical properties of the CNS. Although the nitrogen-doped carbons have been well studied in energy storage applications (see references herein), there is limited knowledge for other heteroatoms' effect and even less for dual or ternary heteroatom doped carbons.

4.3 Experimental

4.3.1 Materials

Hexachlorocyclotriphosphazene (98%), *4,4′*-sulphonyl diphenol (BPS, Fisher) triethylamine (Et$_3$N, Fisher) and analytical grade acetonitrile (MeCN, Fisher) were used as received. Acetone and deionized water were used for the washing steps.

4.3.2 Synthesis of organophosphazene nanospheres and CNS

The synthesis of the PCP**BS** nanospheres was performed according to the scale up procedure described in **Chapter 2**. The conversion of the PCP**BS** nanospheres to CNS took place in a tube furnace from 25 °C to 700, 850 or 1000 °C under N$_2$ gas flow ~100 mL min^{-1} and a heating rate of 2.5 °C min^{-1}. An isothermal step at each target temperature was maintained for 2 h and then the furnace left naturally to cool down to room temperature.

4.3.3 Characterisation
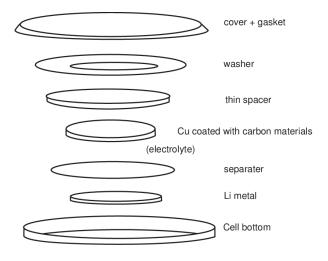
Field emission scanning electron microscopy (FE-SEM) and X-ray electron dispersive spectroscopy analysis (EDS) were performed on a Zeiss SIGMA SEM. Gold-Palladium (AuPd) sputtering was applied to the samples before observation. Carbonised samples did not need sputtering. FT-IR spectra were recorded on a Brucker Tensor 27 spectrometer equipped with an ATR cell. Raman spectra were recorded on a Renishaw inVia Confocal Raman Microscope equipped with 532 nm and 785 laser-lines, and a 0.75 NA (50 x) lens was used. Thermogravimetric analysis curves were obtained with a Mettler Toledo instrument in the temperature range 25–1000 °C at a heating rate of 10 °C min^{-1} under gas N$_2$ flow. The molecular fragment ions of the gases during TGA were analysed by a mass spectrometer connected to the exhaust of the TGA instrument. Specific surface area and pore size

distribution were calculated from the nitrogen adsorption-desorption isotherm curves obtained with a Micromeritics ASAP 2020 Physisorption Analyzer. CNSs were degassed at 200 °C and OPZ at 60 °C for 16 h before measurements and the specific surface area was calculated from an updated B.E.T method. The X-ray diffraction (XRD) patterns were recorded on a Panalytical Empyrean diffractometer with a CoK$_a$ radiation source (1.7902 Å) operated at 40 kV and 40mA. X-ray Photoelctron spectroscopy (XPS) characterization was carried out with a Kratos Axis Ultra DLD spectrometer (using monochromatic Al Kα source (hv = 1486.6 eV). Survey spectra were collected with a pass energy of 160 eV over a binding energy (BE) range of 1200–0 eV. High-resolution spectra were obtained using a 20 eV pass energy (resolution approximately 0.4 eV) and an analysis area of ~300 × 700 μm. The spectrometer was calibrated using the Fermi edge position of a polycrystalline Ag sample immediately prior to the experiments reported below. Peak fitting was performed by using CasaXPS software, using mixed Gaussian-Lorentzian (Voigt) line shapes and Shirley backgrounds.

4.3.4   Electrode Preparation and Electrochemical Characterisation

To prepare the electrode, a slurry was made by mixing the carbon nanospheres with carbon black (Super P 65, TIMCAL) and poly (vinylidene fluoride) (PVDF, Solvay) in *N*-methyl-2-pyrrolidone (NMP, Aldrich,) with a weight ratio of 80:20:10. The obtained suspension was sonicated for one hour, then mixed on a magnetic stirrer for four hours and spread on a copper current collector by using a draw-down coater and a stainless steel applicator (bird applicator) with a 70 μm gap. The solvent was let to completely evaporate in a vacuum oven overnight and the foils were then transferred to a dry-room (humidity less than 1%, −45°C dew point, Munters,). All cell components were dried in a vacuum oven (Binder Vacuum Drying Ovens with integrated vacuum pump system) at 50 °C overnight before assembly. The

galvanostatic cycling were performed using 2032 coin cells (**Scheme 4.1**) from MTI; lithium metal was used as the counter electrode, and Celgard 2325 was used as the separator. To assemble the 2032 coin cells, the electrode foils were cut into disks of 1.2 cm diameter with a loading of about 3.5 mg/cm^2 of active material. The electrolyte was 1M LiPF$_6$ in Ethylene Carbonate/ Ethyl methyl Carbonate (EC/EMC) 3:7 v/v and 1 wt% VC (PuriEl, Soulbrain). The cell were cycled at current rate (from C/20 to 5C) in the 0.005–2V range by using a Maccor Series 4000 battery cycler. Swagelok cells with Li as reference electrode were also assembled for the cyclic voltammetry (CV) test. The CV was performed at a scan rate of 0.1 mV/s in the potential range 0.005–3.0 V using a Biologic VMP3. The cells were tested at ambient temperature.

Scheme 4.1 Schematic of the set-up of a Li-ion (half) cell.

4.4 Results and Discussion

4.4.1 SEM and EDS analysis

PCP**BS** nanospheres were successfully prepared by the scaled-up method described in **Chapter 2**. The procedure was repeated 2 more times in order to collect enough material for the subsequent carbonisation process and characterisation. The accumulated sample was carbonised at 700, 850 and 1000 °C under N_2 and at the same heating rate followed by an isothermal step for 2 hours and a natural cooling back to r.t. The PCP**BS** had a relatively narrow size distribution with diameters of Đ ≈ 330 ± 30 nm and smooth surfaces, accompanied by some smaller nanospheres of Đ < 170 nm (**Figure 4.1 (a)**).

After the carbonisation step, the morphology of the derived CNS remained intact without showing any structural defects, while a decrease of Đ was noticed for the CNS-850 and CNS-1000 due to the gasification of the material and transformation of the organophosphazene the chemical structure to hard carbon material (**Figure 4.1 (c, d)**). On the other hand, the CNS-700 did not show any significant change of Đ. The elemental analysis (EDS) of the bulk CNS, showed the coexistence of carbon with nitrogen, phosphorous, sulfur and oxygen atoms, demonstrating in this way the advantage of the method to facially produce multiple-heteroatom-doped carbon materials. The atomic weight percentages of the elements on each sample are summarized in **Table 4.3**. Initially, the PCP**BS** nanospheres showed a P:S at% ratio close to 1 indicating that the cyclophosphazene ring was connected with 3 BPS. Additionally, a small Cl amount was detected, which is attributed to the unreacted P-Cl and some trapped or surface bounded $Et_3N \cdot HCl$ from the reaction. The overestimation of N at% and the declination from the theoretical stoichiometric 1:1 ratio to P was attributed to two reasons: i) overlapping energies with C which was in excess and ii) to the detection/separation ability of the detector for low atomic number (Z) elements.
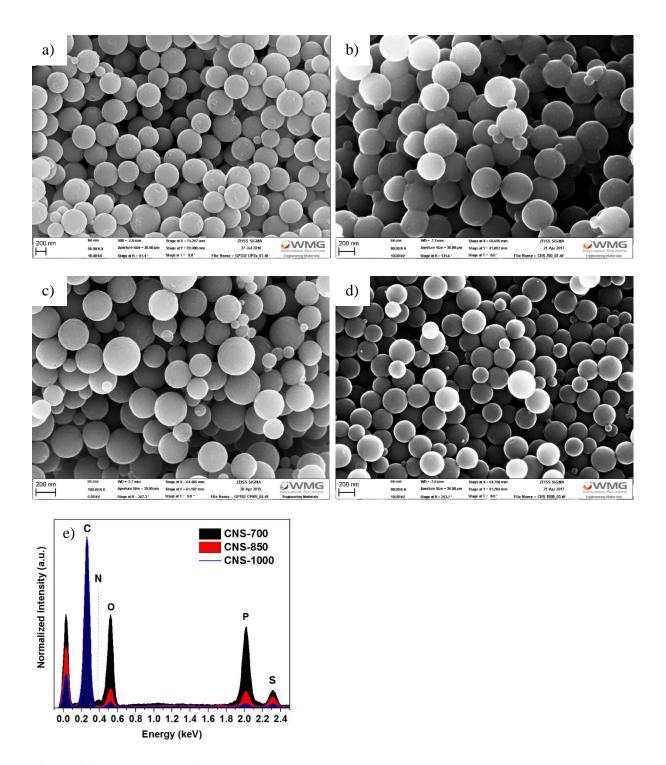
Figure 4.1 SEM images of a) the initial PCPBS nanospheres, b) CNS-700, c) CNS-850 and d) CNS-1000. Scale bar at 200 nm. e) Characteristic EDX spectra of the CNSs samples.

Table 4.3 Atomic weight % of the heteroatoms obtained from the EDS and XPS analysis.

Element	PCBPS	CNS-700	CNS-850	CNS-1000
at% EDS (XPS)				
C	68.50	66.29	81.98	90.34
C 1s	(68.49)	(66.45)	(74.98)	(90.78)
O	17.25	20.13	9.79	4.05
O 1s	(21.21)	(20.22)	(14.45)	(5.50)
N	6.41	3.22	3.42	3.73
N 1s	(2.78)	(4.81)	(4.04)	(1.59)
P	3.68	8.49	2.72	0.93
P 2p	(3.55)	(8.51)	(5.54)	(1.21)
S	3.21	1.87	2.09	0.95
S 2p	(3.65)	(1.01)	(0.99)	(0.92)
Cl	0.95	-	-	-
Cl 2p	(0.32)	-	-	-
Total	100.00	100.00	100.00	100.00

It is important to mention that since the majority of the examined elements have low Z their direct quantitative analysis with EDS would be inaccurate. Therefore, the at% reported here should be taken into account only for the comparison of the samples presented in this work. The comparison and at% evolution with carbonisation temperature was better demonstrated by calculating the heteroatom/C at% as summarized in **Table 4.4** and visualized in **Figure 4.2a**. After pyrolysis, the CNS-700 showed an increased at% for O and P, while N was slightly decreased and the highest heteroatom loss was detected for S. At 850 °C the P and O at% were significantly reduced while the N and S at% remained constant indicating that the mass diffusion of these heteroatoms is almost completed at 700 °C while the P is gasified at higher temperatures. Furthermore, the P and S decreased to 1 at% for CNS-1000 and were almost visible in the EDS spectra while O was further decreased just below 5 at% indicated the reduction of the oxidized species.

Table 4.4 Heteroatom atomic weight % to C

Element	O/C	N/C	P/C	S/C	Cl/C
at% EDS (XPS)					
PCPBS	25.18 (30.96)	9.36 (4.06)	5.37 (5.18)	4.68 (5.33)	1.38 (0.46)
CNS-700	30.3 (30.42)	4.86 (7.24)	12.8 (12.8)	2.82 (1.52)	-
CNS-850	11.9 (19.27)	4.17 (5.39)	3.3 (7.39)	2.55 (1.32)	-
CNS-1000	4.48 (6.06)	4.12 (1.75)	1.02 (1.33)	1.05 (1.01)	-
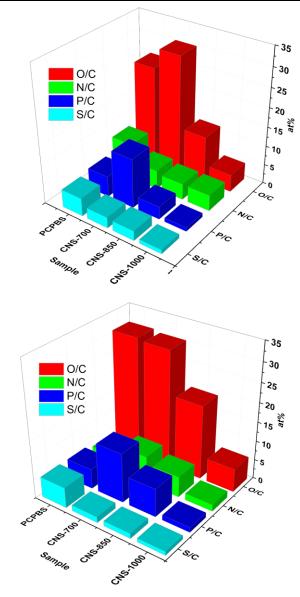
Figure 4.2 a) EDS and b) XPS heteroatom/C at% shown in a 3D bar graph.

4.4.2 XPS analysis

XPS analysis was performed on the CNS in order to investigate in detail the chemical bonding configurations and elemental at% concentration of their surface. The survey spectrum of the samples (**Figure 4.3 (a)**) evidenced the peaks of the expected doping elements, N 1s, S 2p, P 2p along with C 1s and O 1s, and the absolute and heteroatom/C at% are summarized in **Table 4.1** and **Table 4.2**, respectively. Likewise EDS, the XPS analysis showed as similar trend on the at% with the P, O and N increase after carbonisation at 700 °C while at% decreased at higher temperatures due to the gasification of C and the release of more material from the structure.[49] The variation between the at% obtained by XPS and EDS suggested a different surface to bulk chemical environment.

The high resolution spectra of the CNS samples showed an evolution of the major peaks shape and appearance with the temperature increase, showing that various process were taking place during carbonisation of the highly cross-linked **PCPBS** nanospheres. **Figure 4.3 (b)** shows the C 1s spectra of the CNS-700 with the typical graphitic carbon asymmetric peak-shape centered at 284.5 eV, and an associated shake-up feature just above 290 eV originating from the pi - pi* transition.[50] Furthermore, the peaks at 285.6, 286.8, 288.2 and 289.5 eV were assigned to C-O/C-N/C-S[51], C=O/C=N, aromatic N-C=N[52] and O-C=O/N-C=O, respectively. Due to the large amount of various carbon bonds the sp^3 carbon peak did not resolved from the spectra, instead was included to the main graphitic sp^2 peak as its deconvolution was difficult due to the overlap with other peaks. In many publications where the sp^3 peak is resolved in order to calculate the graphitic/amorphous carbon ratio, the examined materials have simpler structures (less dopants) however, the sp^2 peak is mistakenly fitted with a symmetric mixed Lorenzian/Gaussian peak which gives inaccurate results since an asymmetric peak towards higher eV must be selected.[53]

Here, the deconvolution of the sp^3 peak was avoided in order to minimize the error and the same component (peak shape) was used for the resolution of all the carbonised samples. Nevertheless, a narrower FWHM of the graphitic peak and the larger pi-pi* transition peak indicated a trend to more graphitized structure as the temperature raised.
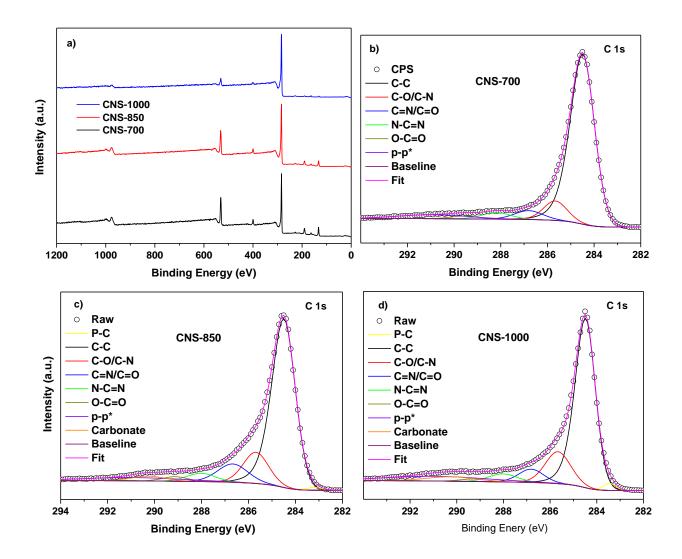
Figure 4.3 a) XPS survey spectrum and fitted high resolution spectra of C 1s; b) CNS-700, c) CNS-850 and d) CNS-1000

At 850 °C the higher peak areas of the oxygenated-nitrogenated species along with the simultaneous decrease of O 1*s* at% was suggested that the increase of these peaks is associated with the increase of C-N/C=N bonding rather than an oxidation of the carbon. This

is in accordance to other reports were the presence of O-containing carbon groups (carbonyl, carboxyl *etc*.) and their importance for the incorporation of other heteroatoms is highlighted.[54, 55] This was further proved by the appearance of the P-C peak[56] (283.2 eV) in the CNS-850 while its intensity was slightly increased and shifted to 283.5 eV for the CNS-1000.

The O 1s spectral envelope of CNS-700 contained the peaks from NO, PO_4^-(P=O)/C=O_{arom} , C-O/C-O-P[57], SO_4^-/S=O and C-O groups at 530.4, 530.9, 531.9 and 532.2 eV, respectively, while the broad peak at higher energy (535.5 eV) was associated with various organic oxygen species (**Figure 4.4 (a)**). Moreover, the CNS-850 and CNS-1000 samples showed an extra peak at 534.2 eV, ascribed to chemisorbed atmospheric H_2O and O_2.[58] The transformation of the O 1s peak from a doublet (CNS-700) to a shoulder-shape peak (CNS-1000) was associated with the changes of the intensity, position and FWHM of the resolved peaks thus indicated a change in the oxidation state of the heteroatoms which is in accordance with the C1s analysis. Specifically, a significant reduction of the oxygen peaks associated with C and P was noticed while the corresponding S-O/O-H peak was decreased and shifted to lower binding energy along with the NO peak due to less oxidized states.

An examination of the N 1s spectrum shown in **Figure 4.4 (b)**, revealed three major components assigned to pyridinic (397.8 eV), pyrrolic (399.9 eV) and substitutional (quaternary) (401.3 eV) nitrogen while a small contribution from N-O species was located at higher energy (404.3 eV). Interestingly, the sample CNS-850 showed an increased pyridinic peak which was then reduced in CNS-1000. It is known, mainly from the research contacted in graphene, that the incorporation of N is important for electrochemical applications since the contribution of its lone pair electrons to the carbon atom change the electronic properties of graphene thus improve the electrochemical

performance.[59, 60] Especially the pyridinic N has been proved theoretically and experimentally that interacts with Li^+ and an enhanced the Li uptake of the active material has been reported. [61]
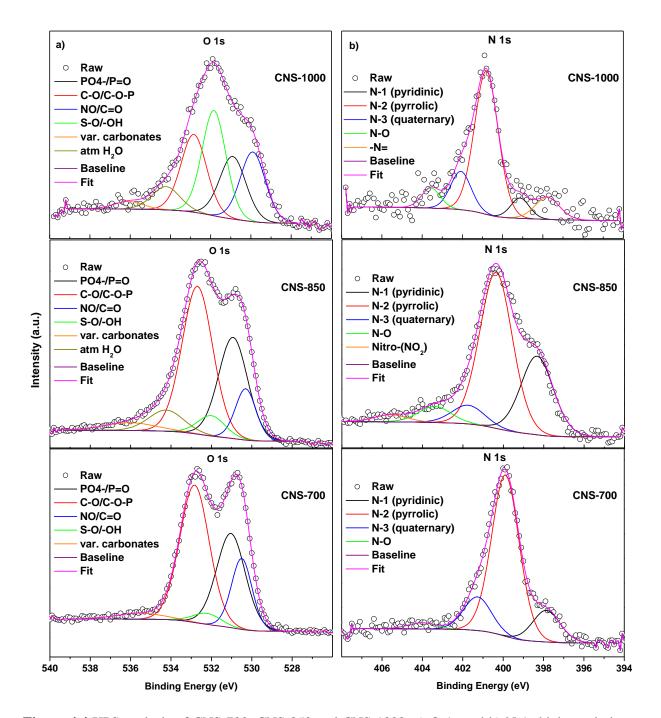
Figure 4.4 XPS analysis of CNS-700, CNS-850 and CNS-1000. a) O 1*s* and b) N 1*s* high resolution spectra.

The obtained P 2*p* and S 2*p* spectra were fitted using multiple components and taking into account the spin-orbit splitting of the main 2p peaks to $2p_{3/2}$ and $2p_{1/2}$ components of 2:1 area ratio. Additionally, the orbital splitting was constrained with a peak separation of 1.18 and 0.86 eV for the P 2p and S 2p, respectively. For clarity, the $p_{1/2}$ peaks are shown with a dashed line and were excluded from the peak list shown in the graphs. Compared to the other heteroatoms, phosphorous has been rarely studied because of its insulating nature thus P-doped carbons have been reported in a relatively small number of studies.[62] Only the last 5 years it began to be studied as a new dopant in carbon materials, since it was found that interacts electrochemically with Li.[63, 64] For this reason, the knowledge of the P bonding in carbon nanomaterials is limited [65]. The P 2*p* spectrum of CNS-700 in **Figure 4.5 (a)** showed the existence of three $2p_{3/2}$ peaks at 130.3, 133.0 and 134.0 eV assigned to P-C$_{arom}$ (phenyl phosphine), P-O (aromatic) and oxidize P-O , respectively, and a smaller peak at 135.6 eV attributed to pure P_2O_5. At 850 °C the oxygen contained species were more evident (indicated also from the P_2O_5 peak) and a further increase of temperature resulted in their reduction and a more intense P-C peak. Sulfur was also successfully incorporated in the CNS as confirmed by XPS analysis; the S 2*p* spectrum of CNS-700 (**Figure 4.5 (b)**) showed the S $2p_{3/2}$ and S $2p_{1/2}$ peaks at 163.6 and 164.8and, which are consistent with C-S-C and C_4S-H bonds such as in thiophene, while the sulfone C-SO$_2$-C group at 167.4 eV (detected for **PCPBS** shown in Chapter 2) reappeared for CNS-850 and CNS-1000 showing that not only the target temperature but also the carbonisation profile (heating ramp, isothermal step) have an impact on the final carbon structure.

From the results above and in agreement with the EDS analysis, it can be concluded that the incorporation of N, S and P atoms within the carbon structure was successful and their bonding environment was rather complicated and significantly varied with carbonisation temperature. Apart from O, P had the highest at%, while S was present in approximately 1

at%. A possible and reasonable explanation of the high P at% of P could be given by: (i) the higher bonding degree of P in the initial **PCPBS** nanospheres structure, (ii) the lower "diffusion" ability of P through the carbon structure due to the larger atomic radius (98 pm) compared to N (56 pm) or S (88 pm), and (iii) the oxidation of P during carbonisation which resulted in solid P_2O_5.
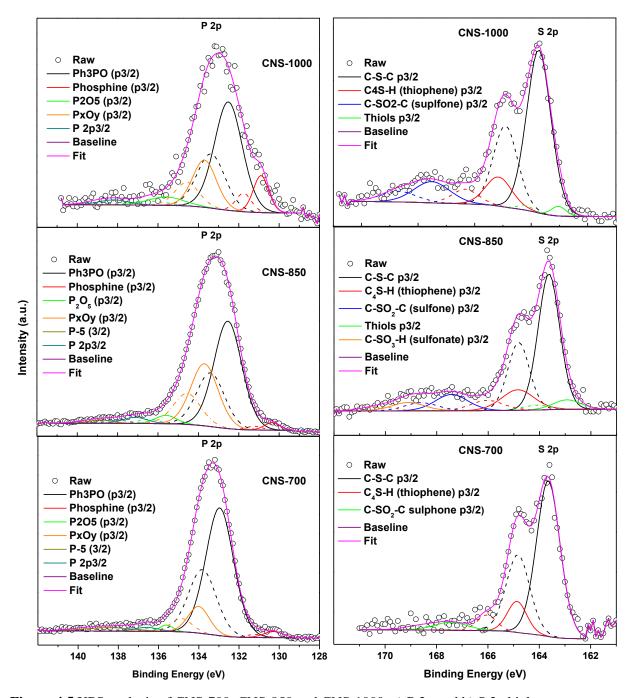
Figure 4.5 XPS analysis of CNS-700, CNS-850 and CNS-1000. a) P 2*p* and b) S 2*p* high res. spectra.

4.4.3 TGA-Mass spectrometry analysis

As discussed in **Chapter 2**, the TGA of PCP**BS** nanospheres showed two major mass losses when heated up to 1000 °C. In order to investigate the decomposition process that took place at each step, the released volatile gases and their evolution during carbonisation was analyzed by mass spectrometry. The overall mass spectrum shown in **Figure 4.6 (a)** compiled several peaks ranged from 1 to 96 m/z highlighting again the complexity of the transformation process to a doped-carbon as showed above in the XPS analysis. By plotting the ion current density of major fragments *versus* the TGA curve of the PCP**BS** nanospheres, a clear visualization of the carbonisation process was achieved. Before the first mass loss step, the evaporation of the atmospheric absorbed H_2O (18 m/z) along with OH^+ (17 m/z) took place. Then a large amount of small molecules with wide m/z range was detected between 420-580 °C which was corresponded to a mass loss of 32%. It can be seen that in this step , CH_4/O^+ (16 m/z), CO_2 (44 m/z), SO (48 m/z) and SO_2/HO_2P^+ (64 m/z) were predominating, while in less extend NO (30 m/z), C_3H_4 (40 m/z), C_5H_6 or C_4H_5N (66 m/z) and phenoxy cation $C_6H_5O^+$ (93 m/z) were also appeared.[66] Additionally, an increase of monoatomic H and N was observed which was not detected on the subsequent step. It is important to mention that the peak of carbon monoxide at 28 m/z was not detectable due to instrumentation limitation reasons. The 2nd mass loss step located at 800 °C was mainly originated from the further hydrocarbon gasification showed by the release of CO_2 and H_2[67] along with a small amount of NO, which resulted in a -16% mass loss at the end of that step. This second mass loss step has never been reported before for this family of materials since in majority of the publications the reported TGA curve is up to 800 °C screening that way the important information.
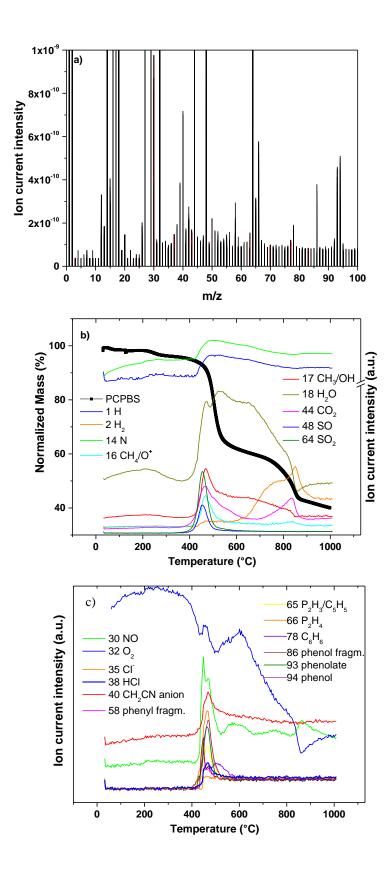
Figure 4.6 a) Total mass spectrum of the fragments released during carbonisation up to 1000 °C and b, c) overlay of TG curve and the main characteristic fragments gas evolution during analysis.

4.4.4 Raman and XRD analysis

Complementary to infrared spectra discussed in **Chapter 2**, the Raman spectra of the PC**PBS** nanospheres before and after carbonisation was recorded. The NIR laser (785 nm) was selected to record the spectra of PC**PBS** since the visible laser (532 nm) produced significant fluorescence and the vibration peaks were not visible. The spectrum in **Figure 4.7(a)** showed the main peaks of BPS at 730, 1154 and 1588 cm^{-1} attributed to C-S, O=S=O, and aromatic C-C stretching, respectively.
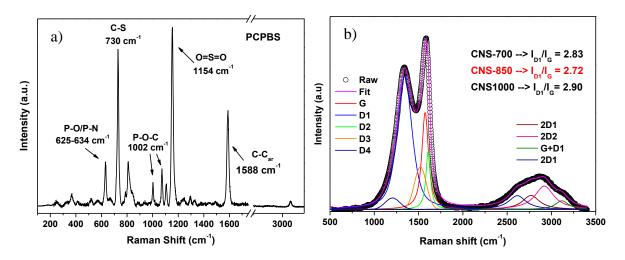
Figure 4.7 Raman spectra of a) PCPBS nanospheres and b) CNS nanospheres carbonised at 850°C.

The bonding between HCCP and PBS was confirmed from the peak at 1002 cm^{-1} assigned to P-O-C stretch vibration. After carbonisation, the peaks arising from HCCP and BPS were transformed to two broad peaks centered at 1597 cm^{-1} (G band) and 1347 cm^{-1} (D band), which belong to carbon sp^2 and sp^3 electronic configurations, respectively. In order to extract an estimation of the amorphous to graphitized carbon content a detailed deconvolution of the broad peaks was performed by selecting a combination of Gaussian, Lorentian and mixed fitting curves[68] as shown in **Figure 4.7(b)**. The calculated intensity peak area ratio I_{D1}/I_G was representative for pyrolized amorphous or partially graphitized carbons and to some extent of defected turbostratic graphitic structure. From the XPS results it was shown that the main C

1s peak was originated from sp^2 carbon therefore the large I_{D1}/I_G values are consequence of the very small graphene sheets with random orientation and abundant exposed edges which give rise to the D1 peak.

The results from Raman spectroscopy were further supported by the XRD pattern of the carbon nanospheres (**Figure 4.8**). For the CNS-700 a single broad peak centered at 26.7° 2θ was assigned to the (002) diffraction planes of hexagonal carbon layers (JCPDS, No. 75-1621).
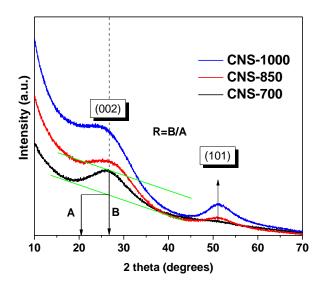
Figure 4.8 XRD pattern of the CNS samples.

Further increase of the temperature resulted to the appearance of a second peak at 51° 2θ assigned to the (101) diffraction of graphene sheets with turbostratic orientation.[37] Similar to the Raman results, the broadening of the peaks is due to the disordered and highly defected structure of the material. A measure of the population of parallel graphene sheets in the carbon structure can be given by calculating the R ratio of the peak height (B) divided by the height of the background (A) as proposed by Dahn et al.[69] Additionally, the interlayer spacing between the graphene sheets was calculated from the Bragg equation applied in the first diffraction peak and the results are listed in **Table 4.5**. From the low R values a single or few

layer parallel graphene sheets are expected while their interlayer spacing is higher than the graphite (0.335 nm).[70]

Table 4.5 Interlayer d spacing and R values obtained by the XRD peaks of the CNS

Sample	(002) (°)	(101) (°)	$d_{(002)}$ (nm)	R
CNS-700	26.7	-	0.387	1.665
CNS-850	27.8	50.8	0.372	1.468
CNS-1000	26.7	51.3	0.388	1.433

4.4.5   N$_2$ sorption analysis

The textural properties of the PCP**BS** and CNS were obtained by the analysis of N$_2$ sorption isotherms. A type-II isotherm -characteristic of non-porous materials- was observed for the PCP**BS** nanospheres with a corresponding BET surface area (S$_{BET}$) of 19 m^2/g. The pore size distribution did not show signs of microporosity except from some wide pores assigned to inter-particle void spaces since no desorption hysteresis loop was evident and intra-particle meso-or macrostructures were detected under TEM or SEM observation as shown before in **Chapter 2**. Similar sorption behavior was observed for the CNS-700 sample while, the S$_{BET}$ decreased to 9 m^2/g due to the shrinkage of the structure and the smoother surface of the carbon nanospheres. However, this result was unusual since most of the precursor materials used for carbon spheres production show increased surface areas and microporosity even at lower carbonisation temperature. A higher specific area would be expected since the previous results from TGA-Mass spec. revealed the extensive release of dopants and carbon material from the initial structure above 480 °C. A possible explanation is the blockage of the pores from small fractions that are not gasified yet and/or the re-deposition of some gasified heavy fractions at this temperature. The NLDFT pore size distribution of CNS-700 showed the presence of mesopores ~ 3 nm, but of very small volume which made their detection in the isotherm

impossible. Eventually, at higher carbonisation temperatures the isotherms showed a totally

different behavior. The CNS-850 and CNS-1000 showed a mixed type of isotherm curves. The

initial high N_2 uptake at low $P/P_0 < 0.1$ with the characteristic "knee" followed by a long

plateau was indicative of type-I isotherm found in microporous materials (**Figure 4.9 a).**
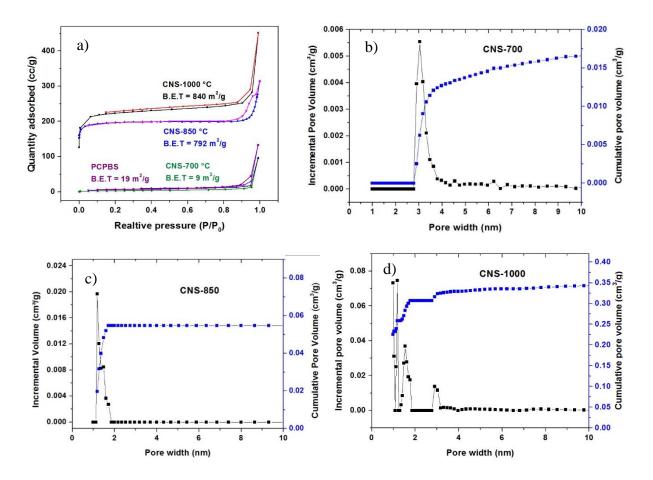
Figure 4.9 a) N_2 adsorption-desorption isotherms of PC**PBS** and CNS samples. Pore size distribution
and cumulative pore volume of b) CNS-700, c) CNS-850 and d) CNS-1000.

The adsorbed volume remained almost constant (only CNS-1000 showed a small increase) up

to 0.9 P/P_0 where a steep increase of the adsorbed N_2 took place due to the capillary

condensation of N_2 into the intra-particle spacing. Furthermore, the desorption branch of CNS-

850 formed a H1-type hysteresis loop which was closed just below 0.8 P/P_0 indicating the

presence of a wide range of mesostructures which again were attributed to interparticle void

spaces of the CNS packaging. Additionally, the hysteresis loop was not so evident for the CNS-

1000 implying that an aggregation could be possible for the CNS-850. The S_{BET} was dramatically increased to 792 and 840 m^2 g^{-1} for the CNS-850 and CNS-1000, respectively. The NLDFT pore size distribution of CNS-850 showed the presence of micropores just below 2 nm which were shifted to lower diameters and higher pore volumes as the carbonisation temperature increased to 1000 °C. Interestingly, the pores at 3 nm detected for CNS-700 were absent in CNS-850 and reappeared in CNS-1000 indicated a continuous transformation of the carbon structure as the temperature increased. The CNS-1000 showed an incomplete size distribution for pores below 0.9 nm which was attributed to the limitation of the analysis method and CO_2 sorption analysis is suggested as more appropriate for a detailed microporous analysis [71]. The V-t method calculations performed on the software showed that the micropores had the major contributor to the total specific surface area for CNS-850 and CNS-1000 while it was negligible for CNS-700 (**Table 4.6**). The high micropore surface area is a result of "defected" carbon structure due to the presence of heteroatoms. Additionally, the presence of the small quantity of Cl in the initial **PCPBS** nanospheres, could also affect the textural structure during carbonisation.[72]

Table 4.6 Textural properties of the PCPBS nanospheres and the carbonised derivatives

Sample	S_{BET} m^2 g^{-1}	Micropore area m^2 g^{-1}	Micropore Volume $cm^3 g^{-1}$	Total pore volume $(cm^3 g^{-1})$
PCPBS	19	-	–	-
CNS-700	9	1	-	0.02
CNS-850	792	691	0.19	0.42
CNS-1000	840	739	0.29	0.57

In summary, the morphological, textural and chemical structure analysis of **PCPBS** discussed in **Chapter 2** and the analysis of the derived CNS, have led to the following conclusions:

- A decrease of the CNS diameter compared to the parent **PCBPS** is noticeable only for temperatures above 850 °C, where a further gasification of the carbon content takes place.

- The heteroatom at% shows variation depending on the atom size, the degree of atomic bonding on the initial **PCPBS** structure and carbonisation temperature.

- CNS showed a different surface to bulk at% concentration of heteroatoms.

- The mass spectrum of the gaseous the molecular fragments along with the XPS analysis of the surface functional groups revealed a dramatic evolution of the O and N over the whole range of temperatures. However, the evolution of P dictated the textural properties of the CNS.

- A high specific surface area and microporous structure was detected only for the samples carbonised at 850 and 1000°C. The textural properties are strongly related to the at% and binding state of the heteroatoms.

4.4.6 Electrochemical behaviour

The lithium storage properties of the CNS were evaluated in Swagelok and coin lithium half-cells by cyclic voltammetry and galvanostatic cycling for their potential application as anode material for lithium batteries. The cyclic voltammetry (CV) test recorded at 0.1 mV s^{-1} and the initial cycle behaviour is shown in **Figure 4.10**. The first cycle showed a cathodic peak at about 0.8 V that was assigned to the electrolyte reduction (decomposition) and the formation of the solid electrolyte interface (SEI) layer.[73] The second cathodic broad peak from about 0.2 V to 0.005 V was assigned to the insertion of the Li ions into the micropores.[74] On the charge cycle, a very

broad anodic peak was detected just above 1.0 V which indicated a reversible oxidation of some SEI components. For the subsequent cycles no other relevant reduction/oxidation peaks were observed, while all samples showed the same behaviour and no other peaks or shifting were detected. The voltammogram was in full agreement with previous reports in which SEI formation and Li insertion peaks were reported in the initial cycles and were absent on the rest of the testing.[75]
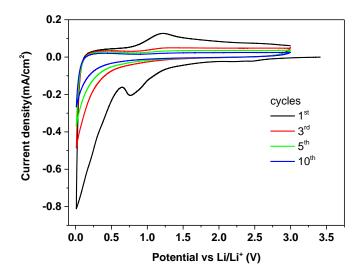
Figure 4.10 Cyclic voltammetry (CV) test of the CNS-850. The graph shows some selected cycles between 5 mV and 3 V at a scan rate of 0.1 mV s^{-1}.

The galvanostatic discharge/charge results of CNS-850 at a current rate C/20 are shown in **Figure 4.11 (a)**. The plateau just below 1.0 V observed in the first discharge branch is originated to the electrolyte decomposition, confirmed also by the peak in the CV shown above. The charge branch showed to distinguished regions; a slope at 0-1.0 V corresponding to Li extraction from the carbon structure and a curve from 1.0 to 2.0 V which is associated with the Li extraction from other sites (dopants, functional groups *etc*.) The disappearance of the discharge plateau on the subsequent cycle, along with the steep charge/discharge curves is characteristic a pseudocapacitance behaviour usually found in hard carbon materials and more particular in pyridinic-doped carbons due to the improved charge mobility.[76] The above findings were in agreement with the XPS analysis, where the CNS-850 showed the presence of abundant pyridinic

species. Moreover, the presence of C=O groups also contribute to the phenomenon, since they stores and release electrons without the need of ion-exchange, thus promote pseudocapacitance.[77] The CNS-850 showed a high initial discharge capacity (C_{in}) of 1126 mA h g^{-1} followed by a large irreversible capacity loss (C_{irr}) of 440 mA h g^{-1} after the first cycle. The large C_{in} is a consequence of the Li consumption during the electrolyte decomposition and the corresponding large C_{irr} indicates a thick SEI formation on the anode.[78] The CNS-1000 showed a lower initial capacity of C_{in} = 870 mA h g^{-1} and a corresponding C_{irr} = 523 mA h g^{-1}, while a C_{in} = 808 mA h g^{-1} and C_{irr} = 191 mA h g^{-1} was found for CNS-700. Considering the different textural characteristics between CNS-700 and the CNS-850 (or CNS-1000) it can be concluded that: i) the specific surface area has much less significant contribution to the Li storage ability than expected and ii) the specific area is proportional to C_{irr}. Therefore, the focus is turned on the surface chemical groups and heteroatom doping. Dahn et al., showed that an increasing chalcogen doping (S, O) resulted in a higher C_{irr} due to irreversible trap of Li from the surface functional groups.[79] In the current work the S content was very low and should have a minor effect on the capacity loss while, the O-containing species were abundant for all the samples. A comparison between CNS-700 and CNS-850 (See Table 4.4 and Figure 4.2) of the O-contained showed a much higher relative at% surface O than the bulk for CNS-850 which could explain the higher C_{irr} compared to CNS-700. At the same time, the slightly higher surface to bulk O along with the high B.E.T area resulted to the highest C_{irr} for the CNS-1000. A further contribution to the high capacity of CNS-850 should be attributed to the high relative P at% which is participating in the lithiation process as discussed in the XPS paragraph.

The cycling stability of the anodes was tested at different current rates up to 1C after the initial formation cycles (3) at a current of C/20 (the theoretical capacity was considered 372 mA h g^{-1} as for a graphite electrode), as shown in **Figure 4.11 (b)**. The CNS-850 showed a revervisble discharge capacity (C_{rev}) of 170 mA h g^{-1} at the end of the 38th cycle while, CNS-1000

delivered 139 mA h g^{-1} and the performance of CNS-700 dropped significantly and delivering only 75 mA h g^{-1}. The subsequent electrochemical testing was carried on with the CNS-850 since it showed the best performance and no other information could be extracted from the CNS-700 and 1000 sample coin cells. The CNS-850 was cycled for a further 100 cycles at the medium-low C/5 current rate (**Figure 4.11 (c)**). After an initial recovery of the capacity that reached 300 mA h g^{-1}, a continuous decline was observed with an overall loss of 7% in the discharge capacity at the end of the 100th cycle. However, a remarkable Coulombic efficiency approaching 100% even from the early cycles was achieved.
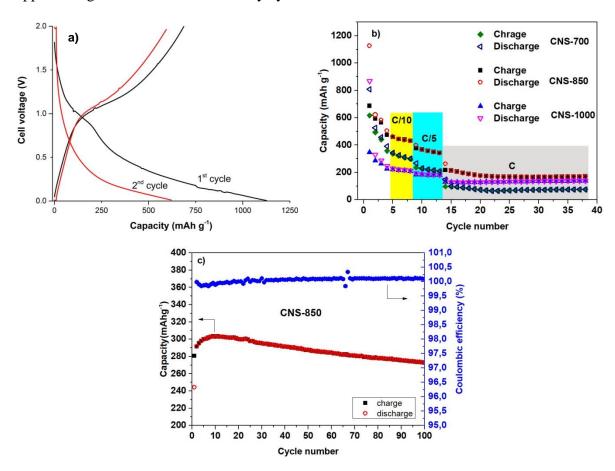
Figure 4.11 a) Charge and discharge voltage profile of of CNS-850 showing the first and second cycles at C/20 , b) capacity vs. cycle number at C/20 (3 cycles), C/10 and C/5 (5 cycles each) and 1C current rate (25 cycles), c) capacity vs. cycle number at C/5 current for 100 cycles.

In order to test the rate capability, the CNS-850 anode was tested at C, 2C and 5C rates for 50 cycles of each current rate. At the end of 140 cycles and at high current rate of 5C the discharge

capacity was still around 90 mA h g^{-1} and the Columbic efficiency close to 100% (**Figure 4.12 (a)**). The long cycling stability was performed at 1C for more than 1000 cycles (**Figure 4.12 (b)**) which is well beyond the generally reported cycling for this type of materials for which no more than few hundreds of cycles are usually reported. The importance of this test has to be underlined since a novel anode material should be able to sustain a prolonged cycling for being considered competitive with the graphite anodes currently in use in commercial devices. The first few formation cycles confirmed the behaviour previously observed of an initial large irreversible capacity. A stable capacity value of about 180 mA h g^{-1} was reached and maintained for about 300 cycles, then a constant decay led to the final discharge value of 125 mA h g^{-1} for the last cycle.
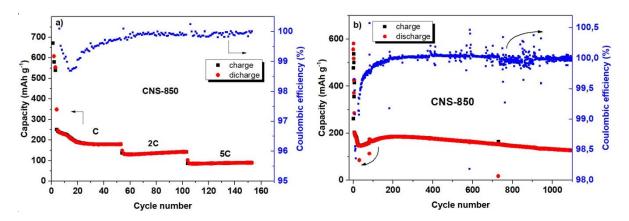
Figure 4.12 Capacity vs. cycle number at: a) at 1C, 2C and 5C current rate for 50 cycles each and b) 1C rate for 1100 cycles.

The Coulombic efficiency, although showed some fluctuation due to the experimental conditions, was definitely high with an average value of 99.992% (calculated over the whole cycling) that is the ideal efficiency required for a real application. The heteroatom-doped CNS showed efficiency among the highest reported in the literature so far highlighting this way their excellent cycle stability. The remarkable cycle performance could be attributed to the unique porous structure which favoured strain relaxation during Li^{+} insertion/extraction and to the presence of heteroatoms possessing enhanced charge mobility. The

electrochemical advantage of the presented CNS-based battery over the structures summarised in **Table 4.2** is based on: a) the relatively low irreversible capacity and b) the very high initial Coulombic efficiency. In those systems, the gravimetric capacity reached impressive values, however, more than 50 % of the initial capacity is lost after the first cycle while, the initial Coulombic efficiency is as low as 55-73 %. The CNS-850 showed a relatively limited loss of 39 % of the initial capacity, while the Coulombic efficiency was > 98% even from the first cycle. Although other hard carbon systems have shown higher rate capabilities[75], the CNS characterized herein for Li-ion cells, doped with O, N, P and S showed an interesting electrochemical performance and could represent a promising material concept. A synergetic effect between structure and heteroatom doping should be responsible for the observed high cycle stability. Heteroatoms are known to affect the electronic properties of carbon, the textural structure (porosity, disorder degree, crystal size) and also increase the active sites of the anode material.[64] All these effects are concomitant thus making it complicated to interpret the single contribution of all those factors to the electrochemical behaviour of the CNS.

4.5   Conclusions

Ternary-heteroatom-doped carbon nanospheres were successfully prepared by carbonisation process of PCP**BS** nanospheres. As discussed in **Chapter 2**, the initial chemical composition of the PCP**BS** cannot be controlled by the synthesis conditions; consequently, the hetroatom-doping level of the derived CNS can only be adjusted by the carbonisation process. Indeed, the carbonisation profile had a significant effect both in the chemical structure and the textural properties of the CNS. At 700°C the microporous structure was not completed thus providing a specific surface area lower even than the parent PCP**BS** nanospheres. On the other hand a heat treatment at 850 and 1000 °C increased the carbon gasification and induced

the heteroatom rearrangement and release as showed by the XPS analysis. This had an dramatic effect in the textural properties and a specific surface area as high as 840 m^2/g was measured for the CNS-1000. This achievement was attributed to the presence of abundant micropores which formed by the heteroatom bonding breakage and realise of gaseous material. The XPS analysis showed a rather complicated carbon chemical structure and an evolution of all the surface species with the temperature. The as-prepared CNS tested as anodes in LIBs and the CNS-850 with the highest at% of pyridinic-N and P, showed a remarkable cycling stability for more than 1000 cycles, delivering a capacity of about 130 mA h g^{-1} at a current rate of 1C. In addition, a remarkable Coulombic efficiency higher than 98% even from the first cycle and as high as 99.99% at the end of 1100 cycles was maintained thereby showing a great promise for the application in LIBs. The high specific surface area, the porous structure and multi-heteroatom doping all contributed to the electrochemical performance of the CNS. These multi-heteroatom-doped CNS are potential materials for various important applications in catalysis, supercapacitors and hydrogen storage and the synergistic effects of dopant atoms could be key to advanced technology. The results here suggest that the organophosphazene chemistry is an efficient method with a true potential for the scale up production of hard carbon materials with multiple heteroatom doping.

4.6   References

1.   G. Pappas, S. Ferrari, X. Huang, R. Bhagat, D. Haddleton and C. Wan, *Materials*, 2016, **9**, 35.

2.   A. D. Roberts, X. Li and H. Zhang, *Chemical Society reviews*, 2014, **43**, 4341-4356.

3.   P. Zhang, Z.-A. Qiao and S. Dai, *Chemical communications*, 2015, **51**, 9246-9256.

4.   J. Liu, N. P. Wickramaratne, S. Z. Qiao and M. Jaroniec, *Nature materials*, 2015, **14**, 763-774.

5.   C. You, S. Liao, H. Li, S. Hou, H. Peng, X. Zeng, F. Liu, R. Zheng, Z. Fu and Y. Li, *Carbon*, 2014, **69**, 294-301.

6.   W. Kiciński, M. Szala and M. Bystrzejewski, *Carbon*, 2014, **68**, 1-32.

7.   L. Qie, W. Chen, X. Xiong, C. Hu, F. Zou, P. Hu and Y. Huang, *Advanced Science*, 2015, **2**, n/a-n/a.

8.   A. Manthiram, Y. Fu, S. H. Chung, C. Zu and Y. S. Su, *Chemical reviews*, 2014, **114**, 11751-11787.

9.   H. Tang, D. Yan, T. Lu and L. Pan, *Electrochimica Acta*, 2017, **241**, 63-72.

10.   J. Zhou, R. Xu, C. Yin, Z. Li, W. Wu and M. Wu, *RSC Adv.*, 2016, **6**, 62005-62010.

11.   K. Chen, X. Huang, C. Wan and H. Liu, *RSC Adv.*, 2015, **5**, 92893-92898.

12.   J. Fu, Q. Xu, J. Chen, Z. Chen, X. Huang and X. Tang, *Chemical communications*, 2010, **46**, 6563-6565.

13.   S. Qiu, W. Xing, X. Mu, X. Feng, C. Ma, R. K. Yuen and Y. Hu, *ACS applied materials & interfaces*, 2016, **8**, 32528-32540.

14.   J. Fu, M. Wang, C. Zhang, P. Zhang and Q. Xu, *Materials Letters*, 2012, **81**, 215-218.

15.   H. Wang, T. Abe, S. Maruyama, Y. Iriyama, Z. Ogumi and K. Yoshikawa, *Advanced Materials*, 2005, **17**, 2857-2860.

16.   G. Zhou, Y. Zhao and A. Manthiram, *Advanced Energy Materials*, 2015, **5**, 1402263.

17.   R. R. Gaddam, D. Yang, R. Narayan, K. Raju, N. A. Kumar and X. S. Zhao, *Nano Energy*, 2016, **26**, 346-352.

18.   Y. Zhao, M. Chen and L. Wu, *Nanotechnology*, 2016, **27**, 342001.

19.   S. Liu, X. Chen, X. Li, P. Huo, Y. Wang, L. Bai, W. Zhang, M. Niu and Z. Li, *RSC Adv.*, 2016, **6**, 89744-89756.

20.   G. Zhu, T. Chen, Y. Hu, L. Ma, R. Chen, H. Lv, Y. Wang, J. Liang, X. Li, C. Yan, H. Zhu, H. Liu, Z. Tie, Z. Jin and J. Liu, *Nano Energy*, 2017, **33**, 229-237.

21. F. Sun, J. Gao, X. Pi, L. Wang, Y. Yang, Z. Qu and S. Wu, *Journal of Power Sources*, 2017, **337**, 189-196.

22. D. S. Su, S. Perathoner and G. Centi, *Chemical reviews*, 2013, **113**, 5782-5816.

23. J. Tang, J. Liu, C. Li, Y. Li, M. O. Tade, S. Dai and Y. Yamauchi, *Angewandte Chemie*, 2015, **54**, 588-593.

24. T. Zhou, Y. Zhou, R. Ma, Z. Zhou, G. Liu, Q. Liu, Y. Zhu and J. Wang, *Carbon*, 2017, **114**, 177-186.

25. C. Zhang, J. Li, E. Liu, C. He, C. Shi, X. Du, R. H. Hauge and N. Zhao, *Carbon*, 2012, **50**, 3513-3521.

26. F. Bottger-Hiller, P. Kempe, G. Cox, A. Panchenko, N. Janssen, A. Petzold, T. Thurn-Albrecht, L. Borchardt, M. Rose, S. Kaskel, C. Georgi, H. Lang and S. Spange, *Angewandte Chemie*, 2013, **52**, 6088-6091.

27. N. S. Choi, Z. Chen, S. A. Freunberger, X. Ji, Y. K. Sun, K. Amine, G. Yushin, L. F. Nazar, J. Cho and P. G. Bruce, *Angewandte Chemie*, 2012, **51**, 9994-10024.

28. S. Xin, Y.-G. Guo and L.-J. Wan, *Accounts of chemical research*, 2012, **45**, 1759-1769.

29. D. Li, C. Feng, H. k. Liu and Z. Guo, *J. Mater. Chem. A*, 2015, **3**, 978-981.

30. H. Park, S. Choi, S.-J. Lee, Y.-G. Cho, G. Hwang, H.-K. Song, N.-S. Choi and S. Park, *Nano Energy*, 2016, **26**, 192-199.

31. H. Zhou, S. Zhu, M. Hibino, I. Honma and M. Ichihara, *Advanced Materials*, 2003, **15**, 2107-2111.

32. K. Sato, M. Noguchi, A. Demachi, N. Oki and M. Endo, *Science*, 1994, **264**, 556-558.

33. J. R. Dahn, T. Zheng, Y. Liu and J. S. Xue, *Science*, 1995, **270**, 590-593.

34. J. Xu, Y. Lin, J. W. Connell and L. Dai, *Small*, 2015, **11**, 6179-6185.

35. K. Zhang, X. Li, J. Liang, Y. Zhu, L. Hu, Q. Cheng, C. Guo, N. Lin and Y. Qian, *Electrochimica Acta*, 2015, **155**, 174-182.

36. J. Xiao, M. Yao, K. Zhu, D. Zhang, S. Zhao, S. Lu, B. Liu, W. Cui and B. Liu, *Nanoscale*, 2013, **5**, 11306-11312.
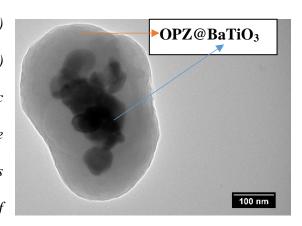
37.   Y. Wang, F. Su, C. D. Wood, J. Y. Lee and X. S. Zhao, *Industrial & Engineering Chemistry Research*, 2008, **47**, 2294-2300.

38.   X. Yue, W. Sun, J. Zhang, F. Wang, Y. Yang, C. Lu, Z. Wang, D. Rooney and K. Sun, *Journal of Power Sources*, 2016, **331**, 10-15.

39.   Q. Ma, L. Wang, W. Xia, D. Jia and Z. Zhao, *Chemistry*, 2016, **22**, 2339-2344.

40.   C. Qian, P. Guo, X. Zhang, R. Zhao, Q. Wu, L. Huan, X. Shen and M. Chen, *RSC Adv.*, 2016, **6**, 93519-93524.

41.   Y. Yang, S. Jin, Z. Zhang, Z. Du, H. Liu, J. Yang, H. Xu and H. Ji, *ACS applied materials & interfaces*, 2017, **9**, 14180-14186.

42.   P. Gao, J. Fu, J. Yang, R. Lv, J. Wang, Y. Nuli and X. Tang, *Physical chemistry chemical physics : PCCP*, 2009, **11**, 11101-11105.

43.   L. Xue, G. Xu, Y. Li, S. Li, K. Fu, Q. Shi and X. Zhang, *ACS applied materials & interfaces*, 2013, **5**, 21-25.

44.   C. Zhang, A. Song, P. Yuan, Q. Wang, P. Wang, S. Zhang, G. Cao and J. H. Hu, *Materials Letters*, 2016, **171**, 63-67.

45.   J. Jiang, H. Chen, Z. Wang, L. Bao, Y. Qiang, S. Guan and J. Chen, *J Colloid Interface Sci*, 2015, **452**, 54-61.

46.   K. Chen, X. Huang, C. Wan and H. Liu, *Electrochimica Acta*, 2016, **222**, 543-550.

47.   K. Chen, X. Huang, C. Wan and H. Liu, *Materials Chemistry and Physics*, 2015, **164**, 85-90.

48.   W. Wei, X. Huang, Y. Tao, K. Chen and X. Tang, *Physical chemistry chemical physics : PCCP*, 2012, **14**, 5966-5972.

49.   G. Hasegawa, T. Deguchi, K. Kanamori, Y. Kobayashi, H. Kageyama, T. Abe and K. Nakanishi, *Chemistry of Materials*, 2015, **27**, 4703-4712.

50.   M. C. Hsiao, S. H. Liao, M. Y. Yen, P. I. Liu, N. W. Pu, C. A. Wang and C. C. Ma, *ACS applied materials & interfaces*, 2010, **2**, 3092-3099.

51.   W. K. Shin, A. G. Kannan and D. W. Kim, *ACS applied materials & interfaces*, 2015, **7**, 23700-23707.

52.   A. P. Dementjev, A. de Graaf, M. C. M. van de Sanden, K. I. Maslakov, A. V. Naumkin and A. A. Serov, *Diamond and Related Materials*, 2000, **9**, 1904-1907.

53. J. Díaz, G. Paolicelli, S. Ferrer and F. Comin, *Physical Review B*, 1996, **54**, 8064-8069.

54. H. L. Poh, P. Šimek, Z. Sofer and M. Pumera, *ACS nano*, 2013, **7**, 5262-5272.

55. W. Shen and W. Fan, *Journal of Materials Chemistry A*, 2013, **1**, 999-1013.

56. H. Hou, L. Shao, Y. Zhang, G. Zou, J. Chen and X. Ji, *Advanced Science*, 2017, **4**, 1600243-n/a.

57. D. Hulicova-Jurcakova, M. Seredych, G. Q. Lu, N. K. Kodiweera, P. E. Stallworth, S. Greenbaum and T. J. Bandosz, *Carbon N Y*, 2009, **47**, 1576-1584.

58. A. M. Puziy, O. I. Poddubnaya and A. M. Ziatdinov, *Applied Surface Science*, 2006, **252**, 8036-8038.

59. H. Wang, T. Maiyalagan and X. Wang, *ACS Catalysis*, 2012, **2**, 781-794.

60. H. Wang, M. Xie, L. Thia, A. Fisher and X. Wang, *The journal of physical chemistry letters*, 2014, **5**, 119-125.

61. M. Hankel, D. Ye, L. Wang and D. J. Searles, *The Journal of Physical Chemistry C*, 2015, **119**, 21921-21927.

62. J. P. Paraknowitsch and A. Thomas, *Energy & Environmental Science*, 2013, **6**, 2839.

63. J. Qian, D. Qiao, X. Ai, Y. Cao and H. Yang, *Chemical communications*, 2012, **48**, 8931-8933.

64. Y. Zhou, Y. Zeng, D. Xu, P. Li, H.-g. Wang, X. Li, Y. Li and Y. Wang, *Electrochimica Acta*, 2015, **184**, 24-31.

65. T. Susi, T. Pichler and P. Ayala, *Beilstein J Nanotechnol*, 2015, **6**, 177-192.

66. S. Wang, F. Xin, Y. Chen, L. Qian and Y. Chen, *Polymer Degradation and Stability*, 2016, **129**, 133-141.

67. Z. Yue and J. Economy, in *Activated Carbon Fiber and Textiles*, Woodhead Publishing, Oxford, Editon edn., 2017, pp. 61-139.

68. A. Sadezky, H. Muckenhuber, H. Grothe, R. Niessner and U. Pöschl, *Carbon*, 2005, **43**, 1731-1742.

69. J. R. Dahn, W. Xing and Y. Gao, *Carbon*, 1997, **35**, 825-830.

70.   X. Chen, F. Tian, C. Persson, W. Duan and N. X. Chen, *Scientific reports*, 2013, **3**, 3046.

71.   D. Cazorla-Amorós, J. Alcañiz-Monge, M. A. de la Casa-Lillo and A. Linares-Solano, *Langmuir : the ACS journal of surfaces and colloids*, 1998, **14**, 4589-4596.

72.   Y. Zhu, H. Cui, X. Meng, J. Zheng, P. Yang, L. Li, Z. Wang, S. Jia and Z. Zhu, *ACS applied materials & interfaces*, 2016, **8**, 6481-6487.

73.   Y.-S. Han, J.-H. Jung and J.-Y. Leec, *Journal of The Electrochemical Society*, 2004, **151**, A291.

74.   F. Wang, R. Song, H. Song, X. Chen, J. Zhou, Z. Ma, M. Li and Q. Lei, *Carbon*, 2015, **81**, 314-321.

75.   K. Tang, R. J. White, X. Mu, M. M. Titirici, P. A. van Aken and J. Maier, *ChemSusChem*, 2012, **5**, 400-403.

76.   J. Zhou, J. Lian, L. Hou, J. Zhang, H. Gou, M. Xia, Y. Zhao, T. A. Strobel, L. Tao and F. Gao, *Nature communications*, 2015, **6**, 8503.

77.   Y. Fang, B. Luo, Y. Jia, X. Li, B. Wang, Q. Song, F. Kang and L. Zhi, *Adv Mater*, 2012, **24**, 6348-6355.

78.   S.-X. Wang, S. Chen, Q. Wei, X. Zhang, S. Y. Wong, S. Sun and X. Li, *Chemistry of Materials*, 2015, **27**, 336-342.

79.   D. Larcher, C. Mudalige, M. Gharghouri and J. R. Dahn, *Electrochimica Acta*, 1999, **44**, 4069-4072.

Chapter 5 Structuring BaTiO$_3$ Nanoparticles with Electron Insulating and Conducting Organophosphazene-based shells

Core-shell structured organophosphazene (OPZ) coated BaTiO$_3$ nanoparticles (OPZ@BaTiO$_3$) were produced via a rapid one-step nucleophilic substitution reaction at ambient conditions. The thickness of the cross-linked OPZ shell was readily tailored by varying the weight ratio of the OPZ monomers to BaTiO$_3$, which in turn affected the relative permittivity and the frequency dependence of the OPZ/BaTiO$_3$ particles. A subsequent carbonisation treatment of the OPZ@BaTiO$_3$ at 700 °C transformed the polymeric OPZ shell to a microporous carbonaceous shell, which dramatically increased the electrical conductivity of the particles. The organophosphazene chemistry offers a facile route to functionalise BaTiO$_3$ nanoparticles without any pre-treatment, and generate a range of core-shell BaTiO$_3$ nanoparticles with tailored dielectric and electrically conductive properties which can be used as active fillers for polymer based nano-composites and energy storage applications.

The results of this work were published under the title "*Functionalization of BaTiO$_3$ nanoparticles with electron insulating and conducting organophosphazene-based hybrid materials*" and the version of the manuscript is presented.[1]

5.1 Introduction

Ferroelectric poly(vinylidenefluoride) (PVDF) and its copolymers, such as poly (vinylidenefluoride-co-trifluoroethylene) (PVDF-co-TrFE), are attractive materials for applications in dielectric devices due to their high dielectric strength ($E_b \sim 4$ MV/cm) and convinient processability. However, the energy storage is limited by their low relative dielectric constant ($e_r \sim 10$).[2, 3] In order to further enhance the relative permittivity and energy density of PVDF-based composites, ferroelectric ceramics, such as $BaTiO_3$, with a significantly higher relative permittivity ($\varepsilon_r \sim 1700$) has been utilised as a dielectric additive.[4, 5] The incorporation of $BaTiO_3$ nanopsrticles into a polymer matrix, usually involves a surface modification procees in order to prevent agglomeration and phase separation, and to increase their interfacial interaction with the polymers. A variety of surface-treatment approaches have been investigated which include: introduction of surface hydroxyls by chemical etching of $BaTiO_3$ particles with H_2O_2[6], chemical modification with pentafluorobenzyl phosphonic acid[7] or fluorosilane[8], and polymeric coatings such as polydopamine[9] and polyaniline[10]. Furthermore, polymer brushes grafted on $BaTiO_3$ nanoparticles, have been synthesized by controlled free radical surface-initiated polymerization techniques such as the reversible addition-fragmentation chain transfer (RAFT)[11, 12], and the atom transfer radical polymerization (ATRP).[13] Despite the promising results, the methods employed above involve extensive pre-treatment of the surface of $BaTiO_3$ particle prior to further functionalisation. The existing processing routes therefore require multi-step reaction and purification procedures which leads to low production yield and high cost.

In addition to dielectric and ferroelectric ceramics, electrically conductive carbons can be used to enhance the relative permittivity of PVDF/ $BaTiO_3$ composites while maintaining a low dielectric loss.[14, 15] Furthermore, the presence of $BaTiO_3$ in these composite systems can also facilitate the dispersion of carbons in the polymer matrix, resulting in a higher interfacial

interaction with the PVDF matrix.[16] In such systems, the increased relative permittivity by the addition of conductive fillers, is attributed to the interfacial polarization resulting from the Maxwell-Wagner-Sillars (MWS) effect.[17] Recently, the decoration of $BaTiO_3$ with conductive graphitic carbon via a chemical vapour deposition (CVD) process, showed its beneficial role in the energy storage of PVDF-HFP composites.[18]

Here, a facile core-shell method was utilised in order to functionalise $BaTiO_3$ nanoparticles through the organophosphazene (OPZ) chemistry described in Chapter 2 . A highly cross-linked OPZ shell is formed on the $BaTiO_3$ surface via one-step reaction at room temperature and ambient conditions. The formation mechanism of OPZ based on the S_N2 nucleophilic substation reaction, generates numerous primary oligomers and their simultaneous aggregation forms a stable and highly cross-linked OPZ network.[19,20,21] The reaction takes place in the presence of an aprotic polar solvent (acetonitrile, tetrahydrofuran, etc.) and an excess amount of triethylamine (Et_3N) which traps the Cl^- released from the substitution on the P atoms of the HCCP. The nature of the above reaction provides an efficient route for producing core-shell nanostructures by applying the same chemistry in the presence of a template.[22] Furthermore, the OPZ shell can be transformed to an electrically conductive carbon shell by carbonisation under inert atmosphere at high temperatures (**Figure 5.1**)
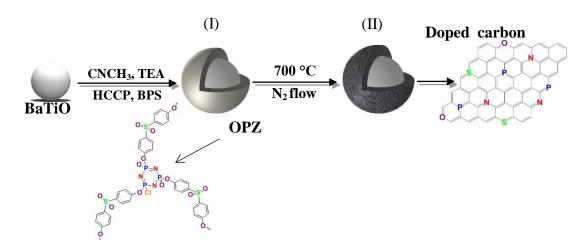
Figure 5.1 Schematic illustration of the synthetic route for the production of (I) OPZ-coated $BaTiO_3$ and (II) carbon-coated $BaTiO_3$ particles after a carbonization process.

The produced carbon structure is highly microporous with small graphitic crystals in a "house of cards" arrangement and with a relatively high degree of heteroatom-doping provided from the monomers.[23, 24] The core-shell nanoparticles can readily serve as a dielectric or conductive additives for polymer-based nanocomposites and energy storage applications. In this context, core-shell OPZ/BaTiO$_3$ nanoparticles with tailored shell structure are studied. The structure and properties of the dielectric OPZ@BaTiO$_3$ and the electrically conducting carbon coated BaTiO$_3$ (C@BaTiO$_3$) are discussed.

5.2 Experimental

5.2.1 Materials

Hexachlorocyclotriphosphazene (HCCP, Sigma-Aldrich, UK), *4,4'*-sulphonildiphenol (BPS, Sigma-Aldrich, UK), triethylamine (Et$_3$N, Fisher Sci, UK), and acetonitrile (MeCN, CH$_3$CN) were used as received. BaTiO$_3$ (Sigma-Aldrich UK, cubic, <50 nm) particles were dispersed in MeCN and sonicated for at least three hours before experiments. Acetone and distilled water were used for the purification of the products.

5.2.2 Synthesis of core-shell OPZ@BaTiO$_3$ and C@BaTiO$_3$

Organophosphazene coated BaTiO$_3$ nanoparticles were successfully prepared by the polycondensation reaction of HCCP and BPS in the presence of BaTiO$_3$ nanoparticles. In a typical synthesis (OPZ@ BaTiO$_3$-1), 0.5 g of BaTiO$_3$ were dispersed in 333 mL of MeCN by sonication for at least 3 hours. HCCP (203 mg) and BPS (463 mg) (BPS: HCCP molar ratio = 3.2) were added to the above mixture and left under sonication for 10 min before the flask was transferred on a magnetic stirrer. Under mild stirring, 5 mL of Et$_3$N was added and the reaction mixture left for 20 hours. The solids were collected by centrifugation, washed once with acetone and twice with acetone/water mixture (1/1 v/v) and then dried in a vacuum oven

at 50°C for 24 hours. Carbon coated $BaTiO_3$ nanoparticles were obtained by carbonization of the as prepared $OPZ@BaTiO_3$ nanoparticles in a tube furnace at 700 °C under N_2 flow. The heating rate was 2.5 °C min^{-1} and an isothermal step at 700 °C was maintained for 2 hours before the furnace physically let to cool down at room temperature. $OPZ@BaTiO_3$ with various shell thicknesses and their carbon derivatives were prepared in the same manner and the synthesis conditions are summarised in **Table 5.1**.

Table 5.1 Concentrations of BPS, HCCP and $BaTiO_3$ for forming $OPZ@BaTiO_3$

Sample name [Shell@Core]	$BaTiO_3$ to monomers weight ratio	BPS (mg/mL)	HCCP (mg/mL)	$BaTiO_3$ (mg/mL)
$OPZ@BaTiO_3$-0.25	0.25:1	0.81	0.36	4.65
$OPZ@BaTiO_3$-0.5	0.5:1	1.45	0.64	4.15
$OPZ@BaTiO_3$-1	1.33:1	1.39	0.61	1.50
$OPZ@ BaTiO_3$-4	4:1	4.17	1.83	1.50
OPZ nanospheres	-	1.13	2.57	-

5.2.3   Synthesis of dense PCPBS nanospheres

Dense poly (cyclotriphosphazene-*co*-sulphonyl diphenol) nanospheres where synthesized in similar manner as the $OPZ@BaTiO_3$ core-shell particles. In a 250 mL round bottom flask containing 150 mL of acetonitrile, HCCP (170 mg) and BPS (387 mg) were dissolved by sonication. The flask was transferred on a magnetic stirrer and Et_3N was added under a mild stirring speed (400 rpm, 3 cm stirring bar). The particle formation was observed in less than 10 seconds after the addition of the base and the mixture was left under continuous stirring for 3 hours. The OPZ nanospheres were collected by centrifugation at 8000 rpm, washed once with acetone and twice with acetone/water mixture and then dried in vacuum oven at 50 °C. This sample was used for the TGA comparison with the $OPZ@BaTiO_3$.

5.2.4 Characterization

Field emission gun-scanning electron microscopy (FEG-SEM) and X-ray electron dispersive spectroscopy analysis (EDS) were performed on a Zeiss SIGMA SEM. AuPd sputtering was applied to the samples before observation. The carbonized samples did not require any preparation due to their high electrical conductivity. Transmission electron microscopy (TEM) micrographs were obtained on JEOL 2000FX operated at 200kV. Raman spectra were recorded on Renishaw inVia spectrometer equipped with 514 nm and 633 laser-lines. Thermogravimetric analysis curves were obtained with a Mettler Toledo instrument in the temperature range 25-700 °C at a heating rate of 10 °C min^{-1} under N_2 gas flow (100 mL min^{-1}). The weight percentage of the carbon shell was calculated from TGA measurements under air flow. Nitrogen adsorption-desorption isotherms were obtained on a Quadrasorb Evo Analyser (Quantachrome). The specific surface area of the OPZ@BaTiO$_3$ samples was calculated by the Brunauer-Emmett-Teller (BET) equation applied on the linear part of the adsorption branch (0.05-0.30 P/P$_0$) and the pore size distribution was obtained by the Barrett-Joyner-Halenda (BJH) method applied on the desorption branch data. For the C@BaTiO$_3$ samples the specific surface area was calculated by the t-plot method and the pore size distribution by Nonlocal Density-Functional Theory (NLDFT) and applying the 'slit-like pores' model of carbon. The samples were degassed at 100°C for 19 hours under high vacuum before measurements. The X-ray diffraction (XRD) patterns were recorded on a Panalytical Empyrean diffractometer with a CoKα radiation source (1.7902 Å) operated at 45 kV and 40 mA. The scanning step width was 0.013° 2θ. X-ray Photoelectron Spectroscopy measurements (XPS) were contacted on a Kratos Axis Ultra DLD spectrometer using monochromatic Al Kα source (hv = 1486.6 eV). Survey spectra (1200-0 eV) were collected with a pass energy of 160 eV, while the high-resolution spectra were obtained using a 20 eV pass energy with a resolution approximately 0.4 eV. Peak fitting was performed on CasaXPS

software, using mixed Gaussian-Lorentzian (Voigt) line shapes and Shirley backgrounds. For electrical measurements, pressed and electroded pellets of the powders were characterised; samples were 5mm in diameter and typically 1-2mm thick. Samples were dried for 24h prior to electrical measurement to remove any adsorbed moisture. Electrical characterisation was undertaken by measurement of the real and imaginary impedance using a Solatron 1260 impedance analyzer with a Solatron 1296 dielectric interface at $0.1V_{rms}$ at frequencies from 1Hz to 1MHz. The ac conductivity, σ, was calculated using,

$$\sigma = \frac{Z'}{Z'^2 + Z''^2} \cdot \frac{t}{A} \qquad \text{(Eq. 5.1)}$$

where Z' and Z'' are the real and imaginary parts of the impedance, A is the area of the sample and t is the sample thickness. The relative permittivity (dielectric constant), ε, was calculated using,

$$\varepsilon = -\frac{Z''}{Z'^2 + Z''^2} \cdot \frac{t}{\omega.A.\varepsilon_0} \qquad \text{(Eq. 5.2)}$$

where ω is the angular frequency ($2\pi f$), f is frequency and ε_0 is the permittivity of free space. The phase angle (θ) between current and voltage and loss tangent (tan δ) was determined from,

$$\theta = tan^{-1}(Z''/Z') \qquad \text{(Eq. 5.3)}$$

$$\tan\delta = -Z'/Z'' \qquad \text{(Eq. 5.4)}$$

5.3   Results and Discussion

5.3.1   Morphology and microstructure characterization

Poly (organophosphazene)-coated dielectric nanoparticles (OPZ@BaTiO$_3$) were synthesised via a nucleophilic substitution reaction between HCCP and BPS in the presence of BaTiO$_3$ nanoparticles. Before the synthesis, the as-purchased commercial BaTiO$_3$ powders consisted of micron-sized (~20μm) spherical agglomerates were broken down and dispersed under extensive sonication in MeCN. The high polarity index of solvent was beneficial for: i) assisting the dispersion and stabilization of the BaTiO$_3$ nanoparticles in the solution, and ii) promoting the nucleophilicity and therefore the reactivity of the BPS towards the P atoms of the HCCP. The previously described reaction mechanism for the formation of OPZ materials, can be also extended to the synthesis of core-shell particles; In the presence of BaTiO$_3$ nanoparticles (or any other sub-micron particles), the primary HCCP-BPS oligomers formed the initial nuclei, which subsequently adsorbed on the surface of the BaTiO$_3$ driven by the tendency to minimize their high free energy. Thus, there is no requirement for functional groups on the surface of the template nanoparticles, which is one of the advantages of the current chemical method. After this stage, more HCCP and BPS monomers and/or HCCP-BPS oligomers were diffused onto the coated BaTiO$_3$ surface where the substitution reaction further took place and led to the growth of a cross-linked OPZ shell.

OPZ@BaTiO$_3$ nanoparticles with different shell-thicknesses were prepared by varying the weight ratio of the monomers to BaTiO$_3$ from 0.25:1 to 4:1, while maintaining a constant molar ratio of the monomers of BPS to HCCP at 3:1. **Figure 5.2** shows the SEM images of the bare BaTiO$_3$ nanoparticles and the core-shell OPZ@BaTiO$_3$ particles prepared at different [HCCP-BPS]/[BaTiO$_3$] weight ratios. The shell thickness increased with an increase of the monomer concentration, and the shape of the particles became more regular as they grow to the sub-micron scale. The EDS spectrum revealed the elements existed in the core-shell

structure (**Figure 5.2(f)**) and the chemical composition of all the samples is summarized in **Table 5.2**.

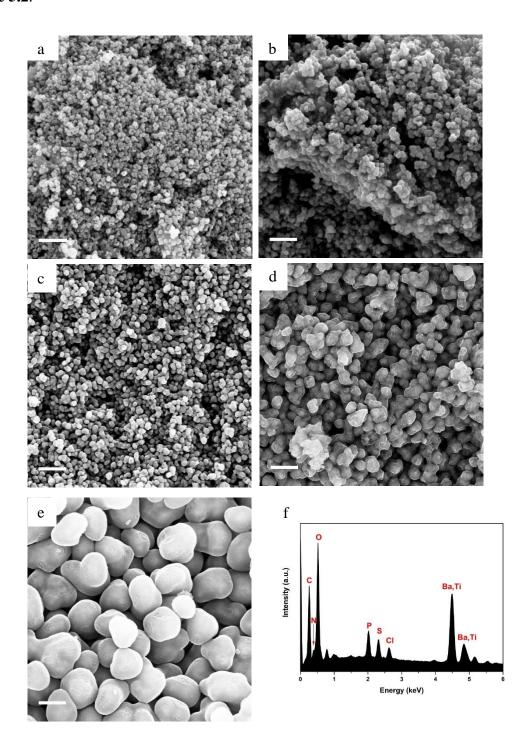

Figure 5.2 SEM images of a) the commercial BaTiO$_3$ particles after sonication, b) OPZ@BaTiO$_3$-0.25, c) OPZ@BaTiO$_3$-0.5, d) OPZ@BaTiO$_3$-1, e) OPZ@BaTiO$_3$-4. Scale bar at 500 nm. f) Representative spectra from EDX elemental analysis.

Table 5.2 Weight percentages as calculated from EDS analysis.

	C	O	S	P	N	Cl	Ba	Ti
Sample	wt %							
OPZ@BaTiO$_3$-0.25	9.4	19.2	1.0	1.3	0.3	0.5	51.0	17.3
OPZ@BaTiO$_3$-0.5	20.0	25.5	1.8	2.1	0.5	0.6	39.1	13.5
OPZ@BaTiO$_3$-1	25.1	31.9	2.1	2.8	1.4	1.3	26.5	8.9
OPZ@BaTiO$_3$-4	36.0	18.5	4.1	4.6	3.8	1.3	24.6	7.0
C@BaTiO$_3$-0.25	2.7	6.7	0.3	1.3	0.1	0.2	65.5	23.4
C@BaTiO$_3$-0.5	4.8	6.6	0.3	1.2	0	0.2	56.5	20.3
C@BaTiO$_3$-1	29.0	16.7	1	5.5	0.4	0	36.0	10.7
C@BaTiO$_3$-4	54.6	14.0	2.1	8.5	4.1	0	12.6	4.1

The ability to modify the BaTiO$_3$ surface was confirmed for all the samples and no free BaTiO$_3$ particles or dense OPZ spheres were noticed in the SEM and TEM images; this result demonstrates that the presented OPZ chemistry can be applied to a wide range of [monomers]/[template] ratios and template concentrations without the need of extensive synthesis optimization. The absence of BaTiO$_3$-free OPZs particles indicated that the nucleation and growth steps followed the "LaMer mechanism" where the initial fast nucleation lowered the monomers' concentration below a critical point and no further formation of new primary nuclei took place.[25] In addition, the HCCP concentration was relatively low in order to prevent any secondary OPZ-particle formation.

By taking advantage of the capability of the In-lens detector to collect secondary electrons (SE) over a wide range of energies, even at relatively low primary beam energy (10 kV), the core-shell structure can be identified from the materials density difference ("Z contrast").[26] The core-BaTiO$_3$ nanoparticles are almost visible under SEM observation and this is more

readily observed in the case of carbonized samples in **Figure 5.3** where the carbon shell has a more "transparent" appearance than the OPZ shell, giving the appearance of "TEM-like" images. This phenomenon is attributed to the conductivity of the carbon shell as well as to a lower density, compared to the OPZ shell, which allows the excited photoelectrons to escape from the structure more easily. **Figure 5.3** shows the morphology of the carbonized samples C@BaTiO$_3$, with shells of different thickness. The cross-linked OPZ shell was directly converted to a carbon shell doped with phosphorus, nitrogen, sulfur and oxygen as shown in the characteristic EDX spectrum (**Figure 5.3 (c), inset**).
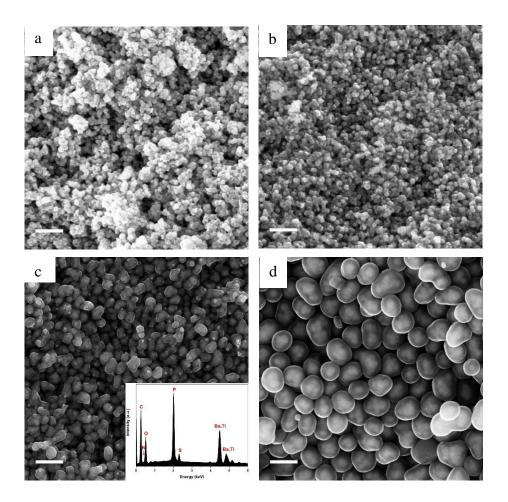
Figure 5.3 SEM images after carbonization at 700 °C of a) C@BaTiO$_3$-0.25, b) C@BaTiO$_3$-0.5, c) C@BaTiO$_3$-1, and d) C@BaTiO$_3$-4. Scale bar at 500 nm.

5.3.2   TG analysis under N_2 and air

After the carbonization process the overall size of the $C@BaTiO_3$ particles decreased, since the conversion of the OPZ shell to carbon under N_2 is followed by a significant mass loss, as shown from the TGA curves (**Figure 5.4 (a)**).
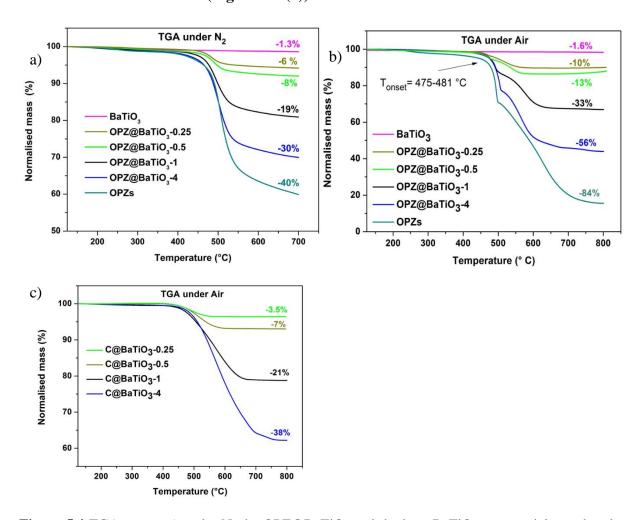
Figure 5.4 TGA curves a) under N_2 the $OPZ@BaTiO_3$ and the bare $BaTiO_3$ nanoparticles and under air of b) $OPZ@BaTiO_3$ the bare $BaTiO_3$ nanoparticles and b) $C@BaTiO_3$.The mass loss was calculated at the range 120-700°C.

The onset decomposition temperature ($T_{on)}$ for all the $OPZ@BaTiO_3$ samples is located approximately at 465 °C. It is important to note that the TGA curves have a negative slope at 700 °C, therefore the mass loss during carbonization in the furnace (2 hrs at 700 °C) should be slightly higher than calculated from the TGA curves. The mass loss percentage of the shell

content of the OPZ@BaTiO$_3$ and C@BaTiO$_3$ core-shell structures was calculated from the TGA$_{air}$ curves shown in **Figure 5.4 (b, c)** and all the results are summarized in **Table 5.3**.

Table 5.3 Summary of the TGA results of different samples tested under Nitrogen and Air.

Sample name [Shell@Core]	Nitrogen Mass loss (%)	Air Mass loss (%)	BaTiO$_3$ wt.%
BaTiO$_3$	1.3	1.6	100
OPZ@BaTiO$_3$-0.25	6	10	88
OPZ@BaTiO$_3$-0.5	8	13	84.5
OPZ@BaTiO$_3$-1	19	33	61
OPZ@BaTiO$_3$-4	30	56	33
OPZ nanospheres	40	84	0
C@BaTiO$_3$-0.25	-	3.5	96.5
C@BaTiO$_3$-0.5	-	7	93
C@BaTiO$_3$-1	-	21	79
C@BaTiO$_3$-4	-	38	62

The TGA$_{air}$ of the OPZ@BaTiO$_3$ showed an initial steep mass loss at 475 °C due to the decomposition of the organic part (BPS) of the nanospheres and the process continued at a slower rate above 500 °C. In order to understand the thermal degradation behaviour, dense OPZs nanospheres were also evaluated under the same conditions; see OPZs in **Figure 5.4 (b)**. Above 500 °C, a similar behaviour to the OPZ@BaTiO$_3$ samples was observed, which attributed to the slower decomposition of the inorganic part of the nanospheres with some oxidation (mainly the P) taking place simultaneously and resulting in a residual mass of 16 wt.%. The TGA under air of the bare BaTiO$_3$ particles did not show any oxidation stage, as would be expected since BaTiO$_3$ is already in an oxidized state. However, the OPZ@BaTiO$_3$-0.25 and OPZ@BaTiO$_3$-0.5 showed a slight mass increase at high temperatures which was attributed to the oxidation of the P atoms. In contrast, the P oxidation was not evident for the

samples with thicker OPZ shells due to the ongoing organic content decomposition at 800 °C, which resulted to negative slopes. Additionally, the OPZs nanospheres analysed under air did not show a complete mass loss (84 %), which was also evident by the observation of some remaining white/grey powder in the crucible. Thus, for the OPZs there is a 16 % of residue oxidized material. In order to calculate the net mass % of BaTiO$_3$ in each sample, the inorganic residue from the hybrid OPZ shell should be subtracted from the obtained results of TGA under air. The mass % of residue subtraction should be calculated according to the OPZ shell thickness. For example, the OPZ@BaTiO$_3$-025 should have less residue compared to the 16 % of the bare OPZ nanospheres, since there is less OPZ material. The mass % of the BaTiO$_3$ in OPZ@BaTiO$_3$ can be calculated from **Eq. 5.6** where the OPZ residue is 16 wt% , OPZ mass loss is 84 wt% and OPZ@BaTiO$_3$-X is the mass loss of the examined sample.

$$BaTiO_3 \, wt\% = 100\% - \left(OPZ@\text{BaTiO}_3 - X \, wt\% \; + \; \frac{OPZ@\text{BaTiO}_3 - X \, wt\% \, loss \, * \, OPZ \, residue \, wt\%}{OPZ \, wt\% \, loss} \right) \quad (Eq.5.5)$$

5.3.3   TEM micrographs and EDX mapping

More detailed information for the morphology and structure of the core-shell particles was provided by the TEM micrographs (**Figure 5.5).** The OPZ@BaTiO$_3$ samples consisted of multiple BaTiO$_3$ nanoparticles cores covered with the cross-linked OPZ shell of thickness proportional to the monomers'concetration. Thus, the thinnest OPZ shell (~ 4 nm) was observed for the OPZ@BaTiO$_3$-0.25 (**Figure 5.5 (b)**), while the OPZ@BaTiO$_3$-4 had a shell thickness of 40-70 nm (**Figure 5.5 (d)**). The shell thickness distribution was observed for all the samples which was attributed to the shape irregularity of the BaTiO$_3$ particles and the multiple-nanoparticle core structure as well. A representative morphology of the core-shell structure after carbonization is shown in **Figure 5.5 (e)**. As expected, no graphitic carbon was observed since the OPZ shell, due to its high cross-linking degree, could not undergo

graphitization and resulted to a "hard carbon" structure, instead. Additionally, the diffusive diffraction rings shown in the selected area of diffraction (SAED) (**Figure 5.5 (f)**), confirmed the amorphous nature or low crystallinity of the carbon shell, while the "spotty" diffraction peaks indicated a polycrystalline $BaTiO_3$ core.
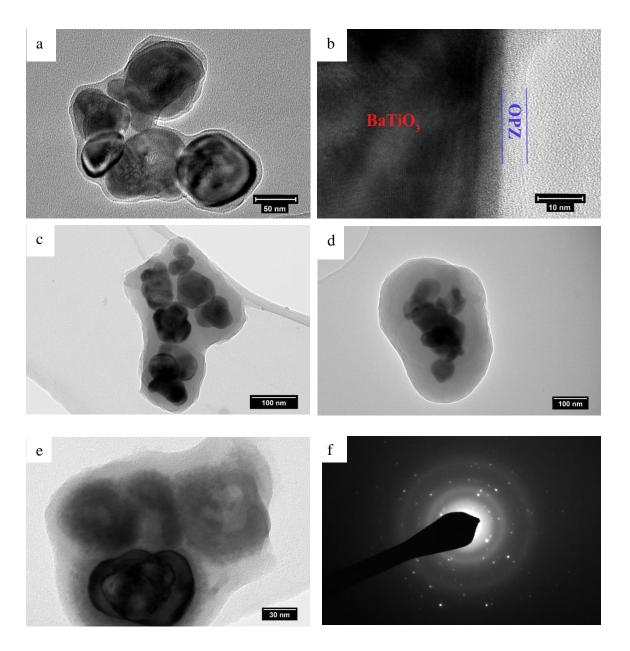
Figure 5.5 TEM micrographs of OPZ@BaTiO$_3$ with a,b) 0.25:1, c) 1.33:1 and d) 4:1 feed ratio. e) C@BaTiO$_3$-1 and b) the corresponding SAED pattern of the same sample.

A representative TEM-EDX mapping of the OPZ@BaTiO$_3$-4 showed a uniform distribution of all the elements originating from the cross-linked HCCP-BPS network around the BaTiO$_3$ particles (**Figure 5.6**).
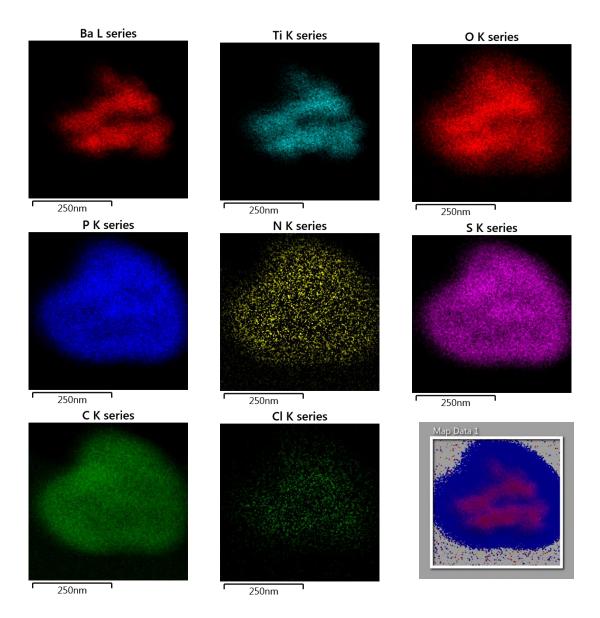
Figure 5.6 TEM-EDX elemental mapping of the OPZ@BaTiO$_3$-4 a) individual mapping of all the elements and the overlay mapping of the Ba (core) and P (shell).

5.3.4   Raman and XRD characterisation

The representative Raman spectra of the OPZ@BaTiO$_3$ is shown in **Figure 5.7 (a)**. The characteristic peaks at 729, 1154, 1588 and 3070 cm^{-1} were assigned to the C-S, symmetric

O=S=O, aromatic C-C and aromatic C-H stretch vibrations, respectively. Additionally, peaks from the $BaTiO_3$ core particles were observed at lower Raman shifts (514, 304, 248 and 185 cm^{-1}) of the spectrum. For all the samples the intensities of the OPZ and $BaTiO_3$ peaks were proportional and inversely proportional, respectively, to the shell thickness.
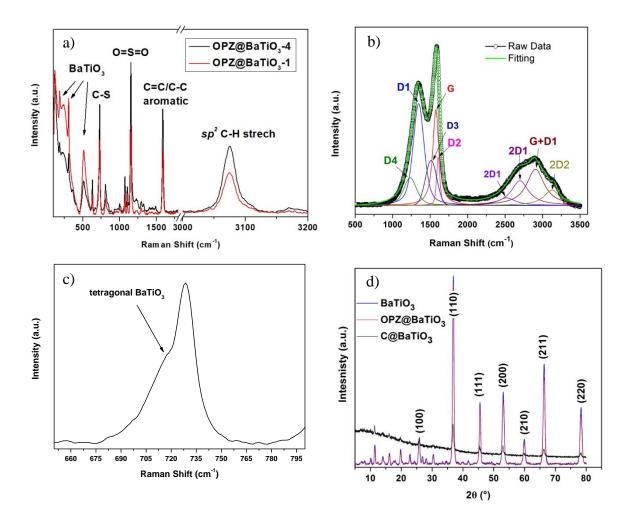
Figure 5.7 Characteristic Raman spectra of a) OPZs@ $BaTiO_3$-1 and b) C@ $BaTiO_3$-1, c) OPZ@$BaTiO_3$ highlighting the presence of the tetragonal structure of $BaTiO_3$, d) XRD patterns of $BaTiO_3$, OPZ@$BaTiO_3$ and C@$BaTiO_3$.

The C@$BaTiO_3$ samples (**Figure 5.7 (b)**) showed the presence of the characteristic broad peaks at 1588 cm^{-1} (G band), 1344 cm^{-1} (D band), and their second order vibrations at the higher frequency range of the spectra, of hard carbons derived from high temperature pyrolysis. The broadening of the peaks suggested that they consisted of a combination of other peaks and a deconvolution process was required in order to reveal the true carbon

structure. The first-order Raman peaks consists of a combination of mixed Gaussian and Lorentzian distributions while the second-order peaks were fitted with Lorentzian-shaped bands. The extent of graphitization was calculated from the I_{D1}/I_G ratio, resulting in a value of 1.08 which is representative of carbonaceous materials with a relatively low degree of graphitization (hard carbons) and small graphene sheets with a "house of cards" arrangement.[27, 28] As discussed in Chapter 4, a I_{D1}/I_G = 2.83 was calculated for the carbon nanospheres treated at 700 °C. The large difference of the I_{D1}/I_G between the bare CNS and the C@BaTiO$_3$ indicated that, in the latter case the substrate (BaTiO$_3$) had a significant impact on the graphitization degree of the carbon shell. Further investigation is necessary for the future development of these OPZ-based materials.

The XRD patterns of the OPZ@BaTiO$_3$ showed sharp peaks assigned to the cubic crystal structure (paraelectric) of BaTiO$_3$ while the C@BaTiO$_3$ showed additionally a broad and intensity below 2θ =25° which was attributed to the hard carbon shell (**Figure 5.7(d)**). Although, the higher dielectric constant of BaTiO$_3$ is originated from the tetragonal crystalline phase usually formed at sintering temperatures > 800°C [29], here, the OPZ@BaTiO$_3$ were heat treated as fine powders (not pressed pellets) in order to prevent breakage of the hybrid shell and aggregation at high temperatures.[30] It is worth noting that, despite the findings from the XRD analysis, the Raman spectra showed a peak at 304 cm^{-1} which is characteristic of the tetragonal phase of BaTiO$_3$, indicated the mixed crystal structure of the as-received commercial material.[31,32] The second characteristic peak at ~715 cm^{-1} of the tetragonal structure, appeared as a shoulder due to the overlapping with the C-S vibration at 729 cm^{-1} (**Figure 5.7 (c)**).

5.3.5   Textural properties

N_2 adsorption-desorption isotherms were used to determine the textural properties of the materials and the representative isotherms from each group of samples are shown in **Figure 5.8 (a),** since all the related samples had similar sorption behaviour. The OPZ@BaTiO$_3$ exhibited a Type-III isotherm, typical of non-porous powder materials with a characteristic steep adsorption close to the saturation pressure (> 0.9 P/P$_0$) due to the capillary condensation that takes place in the inter-particle space.
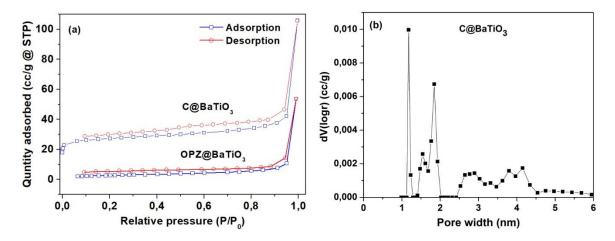
Figure 5.8 Representative a) N_2 adsorption-desorption isotherms of the core-shell particles before and after carbonization and b) pore size distribution of the C@BaTiO$_3$ samples based on NLDFT calculation.

The BET specific surface, calculated at the range 0.05-0.30 P/P$_0$, decreased from 34 to 7 m^2/g area as the shell thickness increased and was attributed to the transformation of the thin-shelled irregular particles to more regular thick-shelled particles at a higher monomer feeding ratio. As the OPZ shell transformed to high disordered and heteroatom-doped carbon, a "knee" appeared at the low P/P$_0$ region and the N_2 adsorbed amount was significantly increased. The isotherm could be assigned as a mixed Type-I isotherm (micropores) and Type IV (mesopores) Due to the presence of micropores in the carbon shell, the pore filling took place before or at the same P/P$_0$ range where the multilayer adsorption is usually taking place and a calculation with the BET method, in the traditional range of 0.05-0.35 P/P$_0$, resulted in negative C constant. For this reason, an updated BET method was used where the P/P$_0$ points

are selected in the range of continuously increasing $V(1-P/P_0)$ values.[33] The contribution of the micropores in the total specific surface area was determined by the t-plot method (Carbon Black model) applied in the range 0.01-0.05 P/P_0. The textural properties of all the samples are summarized in **Table 5.4**. The pore size distribution of the $C@BaTiO_3$ samples was obtained from the NLDFT method and selecting a model for carbons with a slit pore geometry. As shown in **Figure 5.8 (b)**, there are two major peaks at 1.3 and 2.1 nm (micropores) and a small number of suprapores at 3.3-4.3 nm and mesopores at 4.4-6.4 nm. The microporous structure of the carbon shell was attributed to: i) degradation and transformation of the organic part of OPZ shell to carbon, ii) the presence of heteroatoms that escape the shell during carbonization and leave gaps behind, iii) the size and concentration variety of heteroatoms which introduced more defected structure, and iv) the "hard-carbon" nature of the formed material. The porous structures were difficult to observe or identify with TEM analysis, due to the high mixed and disorder structure consisted of with amorphous carbon and small graphitic crystals of random orientations.

Table 5.4 Textural properties of the samples calculated from N_2 sorption isotherms

Sample name [Shell@Core]	Specific surface area m^2/g	Micropore area m^2/g
OPZ@BaTiO$_3$-0.25	34	0
OPZ@BaTiO$_3$-0.5	19	0
OPZ@BaTiO$_3$-1	10	0
OPZ@BaTiO$_3$-4	9	0
C@BaTiO$_3$-0.25	34	5
C@BaTiO$_3$-0.5	65	13
C@BaTiO$_3$-1	105	21
C@BaTiO$_3$-4	183	153

5.3.6 XPS analysis

XPS analysis was performed in order to examine in more detail the composition of the nanostructures. The survey wide scans of the OPZ@BaTiO$_3$-4 and C@BaTiO$_3$-4 in **Figure 5.9,** which are representative for all the samples, show the presence of the all the elements that are expected to be observed in the OPZ shell and the carbon shell after the pyrolysis process. The atomic weight percentages were calculated from the core-level scanning of each element and the results are presented in **Table 5.5**.
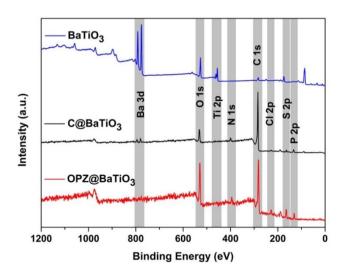
Figure 5.9 XPS survey scans of the as received BaTiO$_3$ and the core-shell particles before and after carbonization.

Table 5.5 Percentage atomic concentrations as calculated from high resolution XPS analysis.

	C 1s	O 1s	S 2p	P 2p	N 1s	Cl 2p	Ba 3d	Ti 2p
Sample				at%				
OPZ@BaTiO$_3$-1	63.05	21.94	5.13	5.81	3.72	0.58	0.34	0.37
OPZ@BaTiO$_3$-4	63.12	21.30	5.16	5.24	4.37	0.81	-	-
C@BaTiO$_3$-1	82.43	10.59	0.89	2.21	1.82	-	1.71	0.35
C@BaTiO$_3$-4	82.93	9.86	1.24	3.01	2.69	-	0.28	-

The P/S ratio (~1) indicated that the monomeric unit of the cross-linked OPZ structure consisted of one phosphonitrilic trimer connected with three BPS molecules which is in agreement with the initial molar ratio of the monomers (3:1). It is known from previous reports that nucleophiles with a relative large and non-planar structure take part only in non-geminal substitution of the P-Cl, thus each P atom is bonded with only one BPS molecule.[34] The remaining P-Cl could be substituted by any H_2O molecules that are present in the commercial chemicals (monomers, solvents) and in the atmosphere, forming P=O or P-OH bonds. A small amount of Cl (< 1 at%) mainly originated from unreacted P-Cl and some Cl with ionic character ($Et_3N•HCl$) that may be trapped in the structure and its presence, even in a small percentage here, contributed in the formation of the microporous carbon structure during pyrolysis.[35] The resolved spectra of the high-resolution scans also showed a multi-binding state for all the elements before and after carbonization (**Figure 5.10**). In particular, the O 1s peak of the $OPZ@BaTiO_3$ was resolved in three different peaks with the most significant, at 531.4 eV, assigned to the surface aromatic C-OH which is important property for a good dispersion in organic solvents and high interaction of these materials in dielectric polymer matrices (*e.g.* PVDF). The absence of Ba 3d and Ti 2p peaks in the $OPZ@BaTiO_3$-4 sample is attributed to the thick OPZ shell which is much larger than the penetration depth of the incident beam (~ 10 nm). After the pyrolysis process the converted carbon structure doped with O, P, N and S, showed a significant change of the elements binding states and it is well known that the presence of heteroatoms in carbons significantly alter their electronic as well as their textural properties.[36,37] The analysis of the N 1s peak showed the presence of three different components at 398.2, 400.2 and 402.6 eV assigned to pyrridinic, pyrolic/quaternary and oxidized nitrogen which contribute to the electronic properties of the carbon. P and S showed a decrease in the number of the different components which is explained by their presence mainly as oxides in the structure that contributes to the formation of the extended microporous structure of the carbon shell[24] (**Figure 5.10 (c-e)**).
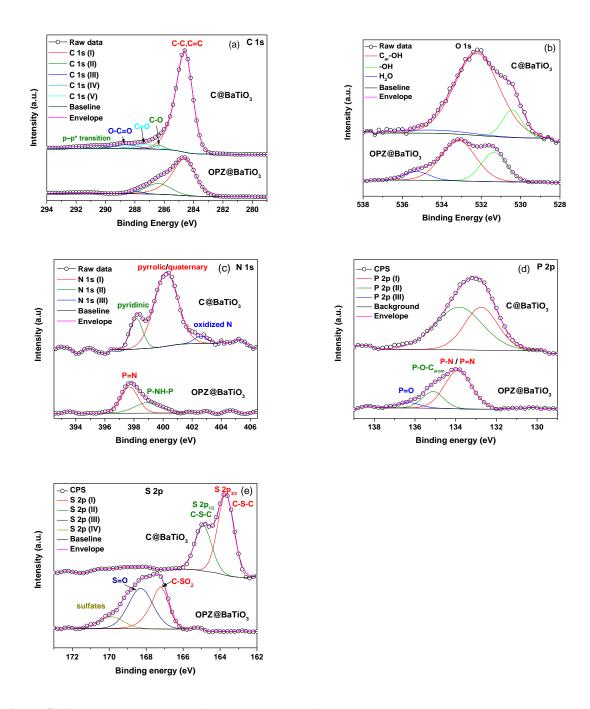
Figure 5.10 Core-level XPS scanning and deconvolution of the peaks of the core-shell particles before and after carbonization.

Among the heteroatoms, S had the lowest at% while the highest was for O due to some oxidation that took place during carbonization in the furnace. In contrast to OPZ@BaTiO$_3$, the survey spectrum of the carbonized samples clearly showed the peaks from the BaTiO$_3$ core particles. Specifically, the spin-orbital splitting of the Ba 3d peak was observed in the C@BaTiO$_3$-4 despite the fact that its shell was thicker than the non-carbonized

OPZ@BaTiO$_3$-1 (thin shell). This observation was related with two factors: i) the difference in electronic conductivity between the OPZ (insulator) and C (conductor) shell so that the exited photoelectrons can "travel" easier through the C shell. ii) the lower density of the C shell allows for deeper penetration of the incident X-ray beam and decreased inelastic energy loss of the extracted photoelectrons.

5.3.7 Dielectric properties of the core-shell particles

Figure 5.11 shows the frequency dependent ac conductivity, permittivity, phase angle and dielectric loss for the core-shell powders along with impedance measurements on dense OPZ nanospheres.
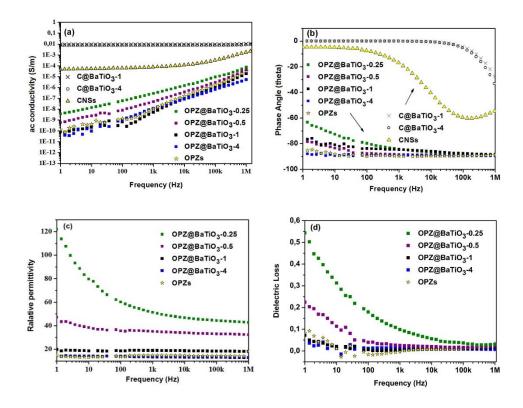
Figure 5.11 a) AC conductivity of the OPZ@ BaTiO$_3$ and C@BTO samples and comparison with the dense OPZ, b) Phase angle of OPZ@ BaTiO$_3$ and C@BTO samples. Phase angle approaching 0 deg indicates conductive behavior, approaching 90deg indicates capacitative behavior, c) Relative permittivity of the OPZ@BaTiO$_3$ samples and comparison with the dense OPZ nanospheres. d) Dielectric loss of the OPZ@BaTiO$_3$ samples and comparison with the dense OPZ nanospheres.

The OPZ@BaTiO$_3$ samples exhibited low ac conductivity and the linear relationship with frequency in **Figure 5.11 (a)** was a result of the frequency dependences of the admittances of the capacitive regions ($i\omega C$) that contributed to the conduction paths in these highly insulating materials. This can also be observed in **Figure 5.11 (b)**, whereby in these purely capacitive materials the ac current lagged the ac voltage by 90°; this is a further indication of the dielectric and capacitive nature of the OPZ@ BaTiO$_3$ samples. The dense OPZ nanospheres and the OPZ@BaTiO$_3$-4 core-shell particles with the thicker OPZ shells exhibited the lowest ac conductivities and the highest phase angle due to the insulating nature of the OPZ shell. In the contrary, the C@ BaTiO$_3$ samples had much higher conductivity at low frequencies (DC conductivity) and the conductivity in these core-shell particles was frequency independent. Such a response is indicative of conductive behaviour since the admittance of a resistor is simply *1/R* and this can also be seen from the phase angle approaching 0° where current and voltage are in phase. **Figure 5.11 (c)** shows the frequency dependent relative permittivity of the OPZ@ BaTiO$_3$ materials. The relative permittivity increased as the OPZs shell becomes thinner and the contribution of BaTiO$_3$ to the relative permittivity is more effective; this can also be seen in **Table 5.6**. The observed frequency dependence of the permittivity in **Figure 5.11 (c)**, at low frequencies, was more pronounced in the samples with a thin OPZ layer and has been shown to be related to the presence of conductivity in the material.[38] This can be seen in **Figure 5.11 (d)** where the samples with higher dielectric loss exhibited the stronger frequency dependence at low frequencies (**Figure 5.11 (c)**). At higher frequencies the admittance of the capacitive regions ($i\omega C$) increased and ac currents flowed through the capacitative (insulating) regions of the material and the influence of conductivity on permittivity and dielectric loss was therefore reduced; see **Figure 5.11 (c,d)** where the responses are almost frequency independent above 10^{3}Hz. The C@ BaTiO$_3$ samples are not shown since they exhibit high ac conductivity and the permittivity is not relevant.

Table 5.6 Relative permittivity and loss at 1k Hz.

Sample name [Shell@Core]	Relative permittivity ε'	Dielectric loss	BaTiO₃ wt.%
OPZ@BaTiO$_3$-0.25	51	0.098	88
OPZ@BaTiO$_3$-0.5	35	0.025	85
OPZ@BaTiO$_3$-1	19	0.005	61
OPZ@BaTiO$_3$-4	13	0.015	33
OPZ nanospheres	15	0.006	0

Since the bare OPZ nanospheres showed very low conductivity and frequency independent permittivity, the conductivity was likely to originate from the BaTiO$_3$. Indeed, the high resolution XPS of the "as received" BaTiO$_3$ showed the presence of BaCO$_3$ as it can be seen from the deconvolution of the C 1s, Ba3d$_{5/2}$ and O 1s peaks (**Figure 5.12**). The presence of carbonate, which contributes to the conductivity, is common for the perovskite materials and it is originated from the synthetic procedures as well as from the reaction with the atmospheric CO$_2$.[39-41] Therefore, the nanoparticles with thin shell showed higher dielectric losses compared to the thick OPZ shells which provide more insulating characteristics. A decreasing permittivity and dielectric loss with increasing frequency, has been observed for thin films of BaTiO$_3$-polymer core-shell particles with even lower ac conductivities than reported here.[42, 43] In this work the measurements were conducted on pressed powders and the presence of low-permittivity air between the inter-particle spaces can lower the measured effective permittivity and give some inaccuracy. However, the dielectric losses for all the OPZ@BaTiO$_3$ were surprisingly low. The above results suggest that the electrical properties of organophosphazene-decorated BaTiO$_3$ particles, can therefore be readily tailored from highly insulating (capacitive) and low dielectric loss (OPZ@BaTiO$_3$) to electrically

conducting (C@BaTiO$_3$), by varying the shell thickness and chemical structure. The above properties could make these materials good candidates as hybrid fillers (OPZ@BaTiO$_3$) in ferroelectric polymer nanocomposites for the improvement of the high dielectric loss of the polymer matrix, as well as active fillers (C@BaTiO$_3$) in dielectric percolative composites.
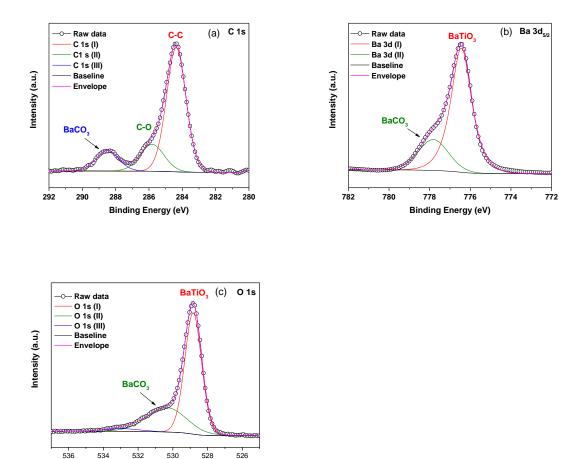

Figure 5.12 Examination of BaTiO$_3$. XPS core-level spectra of a) C 1s, b) Ba 3d$_{5/2}$ and c) O 1s indicating the presence of BaCO$_3$.

5.4   Conclusions

This Chapter presented a facile route to functionalise BaTiO$_3$ nanoparticles with an organophosphazene insulating shell at ambient conditions and within a short timescale. It was demonstrated that the OPZ shell thickness can be readily controlled by adjusting the feeding ratio of the monomers to BaTiO$_3$. The electrically insulating core-shell OPZ@BaTiO$_3$ nanoparticles could also be transformed into electrically conducting carbon coated BaTiO$_3$ nanoparticles with well-preserved morphologies by a simple carbonization treatment. This work provides a facile and cost-effective route to generate novel core-shell nanoparticles with well-defined shell structures and properties that range from electrically insulating (OPZ) to highly conductive (carbon). As shown both in **Chapters 4 and 5**, the resultant products of the organophosphazene chemistry can be readily applied as active materials in electrochemical energy storage applications such as lithium batteries and capacitors.

5.5   References

1. G. S. Pappas, C. Wan, C. Bowen, David M. Haddleton and X. Huang, *RSC Adv.*, 2017, **7**, 19674-19683.

2. A. J. Lovinger, *Science*, 1983, **220**, 1115-1121.

3. Q. M. Zhang, *Science*, 1998, **280**, 2101-2104.

4. S. Cho, J. S. Lee and J. Jang, *Advanced Materials Interfaces*, 2015, **2**, 1500098.

5. K. Yang, X. Huang, M. Zhu, L. Xie, T. Tanaka and P. Jiang, *ACS applied materials & interfaces*, 2014, **6**, 1812-1822.

6. T. Zhou, J. W. Zha, R. Y. Cui, B. H. Fan, J. K. Yuan and Z. M. Dang, *ACS applied materials & interfaces*, 2011, **3**, 2184-2188.

7.   P. Kim, N. M. Doss, J. P. Tillotson, P. J. Hotchkiss, M. J. Pan, S. R. Marder, J. Li, J. P. Calame and J. W. Perry, *ACS Nano*, 2009, **3**, 2581-2592.

8.   X. Zhang, Y. Ma, C. Zhao and W. Yang, *Applied Surface Science*, 2014, **305**, 531-538.

9.   N. Jia, Q. Xing, X. Liu, J. Sun, G. Xia, W. Huang and R. Song, *J Colloid Interface Sci*, 2015, **453**, 169-176.

10.   X. Zhang, S. Wei, N. Haldolaarachchige, H. A. Colorado, Z. Luo, D. P. Young and Z. Guo, *The Journal of Physical Chemistry C*, 2012, **116**, 15731-15740.

11.   K. Yang, X. Huang, Y. Huang, L. Xie and P. Jiang, *Chemistry of Materials*, 2013, **25**, 2327-2338.

12.   M. Zhu, X. Huang, K. Yang, X. Zhai, J. Zhang, J. He and P. Jiang, *ACS applied materials & interfaces*, 2014, **6**, 19644-19654.

13.   L. Xie, X. Huang, Y. Huang, K. Yang and P. Jiang, *The Journal of Physical Chemistry C*, 2013, **117**, 22525-22537.

14.   A. C. Patsidis, K. Kalaitzidou, D. L. Anastassopoulos, A. A. Vradis and G. C. Psarras, *Journal of the Chinese Advanced Materials Society*, 2014, **2**, 207-221.

15.   Z. M. Dang, L. Wang, Y. Yin, Q. Zhang and Q. Q. Lei, *Advanced Materials*, 2007, **19**, 852-857.

16.   Z.-M. Dang, S.-H. Yao, J.-K. Yuan and J. Bai, *The Journal of Physical Chemistry C*, 2010, **114**, 13204-13209.

17.   J.-K. Yuan, S.-H. Yao, Z.-M. Dang, A. Sylvestre, M. Genestoux and J. Bai, *The Journal of Physical Chemistry C*, 2011, **115**, 5515-5521.

18.   Y. Feng, W. L. Li, J. P. Wang, J. H. Yin and W. D. Fei, *J. Mater. Chem. A*, 2015, **3**, 20313-20321.

19.   Y. Zhu, X. Huang, W. Li, J. Fu and X. Tang, *Materials Letters*, 2008, **62**, 1389-1392.

20.   L. Zhu, Y. Xu, W. Yuan, J. Xi, X. Huang, X. Tang and S. Zheng, *Advanced Materials*, 2006, **18**, 2997-3000.

21.   P. Zhang, X. Huang, J. Fu, Y. Huang, Y. Zhu and X. Tang, *Macromolecular Chemistry and Physics*, 2009, **210**, 792-798.

22.   S. Yang, C. Cao, Y. Sun, P. Huang, F. Wei and W. Song, *Angewandte Chemie*, 2015, **54**, 2661-2664.

23. J. Fu, Q. Xu, J. Chen, Z. Chen, X. Huang and X. Tang, *Chemical communications*, 2010, **46**, 6563-6565.

24. G. Pappas, S. Ferrari, X. Huang, R. Bhagat, D. Haddleton and C. Wan, *Materials*, 2016, **9**, 35.

25. V. K. LaMer and R. H. Dinegar, *Journal of the American Chemical Society*, 1950, **72**, 4847-4854.

26. J. B. Ledeuil, A. Uhart, S. Soule, J. Allouche, J. C. Dupin and H. Martinez, *Nanoscale*, 2014, **6**, 11130-11140.

27. A. Sadezky, H. Muckenhuber, H. Grothe, R. Niessner and U. Pöschl, *Carbon*, 2005, **43**, 1731-1742.

28. J. R. Dahn, W. Xing and Y. Gao, *Carbon*, 1997, **35**, 825-830.

29. P. K. Dutta, R. Asiaie, S. A. Akbar and W. Zhu, *Chemistry of Materials*, 1994, **6**, 1542-1548.

30. C. W. Beier, M. A. Cuevas and R. L. Brutchey, *Langmuir : the ACS journal of surfaces and colloids*, 2010, **26**, 5067-5071.

31. M. B. Smith, K. Page, T. Siegrist, P. L. Redmond, E. C. Walter, R. Seshadri, L. E. Brus and M. L. Steigerwald, *J Am Chem Soc*, 2008, **130**, 6955-6963.

32. M. El Marssi, F. Le Marrec, I. A. Lukyanchuk and M. G. Karkut, *Journal of Applied Physics*, 2003, **94**, 3307.

33. M. Thommes, K. Kaneko, A. V. Neimark, J. P. Olivier, F. Rodriguez-Reinoso, J. Rouquerol and K. S. W. Sing, *Pure and Applied Chemistry*, 2015, **87**.

34. R. G. De Jaeger, M., *Progress in Polymer Science*, 1998, **23**, 179-276.

35. C. Chen, X.-y. Zhu, Q.-l. Gao, F. Fang, L.-w. Wang and X.-j. Huang, *Journal of Molecular Catalysis B: Enzymatic*, 2016, **132**, 67-74.

36. X. Wang, G. Sun, P. Routh, D. H. Kim, W. Huang and P. Chen, *Chemical Society reviews*, 2014, **43**, 7067-7098.

37. G. Hasegawa, T. Deguchi, K. Kanamori, Y. Kobayashi, H. Kageyama, T. Abe and K. Nakanishi, *Chemistry of Materials*, 2015, **27**, 4703-4712.

38. D. P. Almond and C. R. Bowen, *Physical review letters*, 2004, **92**, 157601.

39.   C. Miot, E. Husson, C. Proust, R. Erre and J. P. Coutures, *Journal of the European Ceramic Society*, 1998, **18**, 339-343.

40.   M. Wegmann, L. Watson and A. Hendry, *Journal of the American Ceramic Society*, 2004, **87**, 371-377.

41.   M. d. C. B. López, G. Fourlaris, B. Rand and F. L. Riley, *Journal of the American Ceramic Society*, 1999, **82**, 1777-1786.

42.   L. Xie, X. Huang, C. Wu and P. Jiang, *Journal of Materials Chemistry*, 2011, **21**, 5897.

43.   L. Xie, X. Huang, Y. Huang, K. Yang and P. Jiang, *ACS applied materials & interfaces*, 2013, **5**, 1747-1756.

Chapter 6 Conclusions and suggestions for future development

6.1   Conclusions

This thesis was focused on the synthesis and characterisation of cyclomatrix organophosphazene nanospheres and their carbon-derivatives obtained by pyrolysis at high temperature. The morphology and physicochemical characterisation of the materials were analysed and discussed in-depth, in order to establish a better understanding of the cyclomatrix OPZs chemistry. Furthermore, the potential application of these materials in electrical energy storage systems, was evaluated by electrochemical Li-ion coin cells as well as dielectric nanopowders.

Firstly of all, the synthesis mechanism of OPZs was studied and proposed to follow a nucleophilic substitution reaction. For the first time, the factors including the polarity of the solvent, the basicity of the organic base and the geometry of the nucleophile that affect the reaction kinetics and the morphology of the OPZs have been studied in detail. The understanding of the unique synthesis procedure not only provided a better understanding of the relationship of the synthetic conditions and particle morphologies, but also enabled a design of a new synthetic setup for scale-up production.

Secondly, the facile adjustment of the structural diversity through the regulation of the synthetic conditions was highlighted through the production of hollow OPZs in a one-step approach. In the presence of MeCN/H_2O the nucleation and growth of OPZs was governed by a direct-self-templated mechanism and a simultaneously dissolution of the internal structure. This exciting phenomenon was further studied under different water/acetonitrile solutions and was extended to the synthesis of hollow OPZs based on a co-linker with planar geometry. The obtained hollow nanospheres and microcapsules showed a structural stability

dependence on the selected nucleophile. The non-planar BPS offered more rigid and chemically stable nanospheres than the planar PG.

Thirdly, CNS co-doped with O, N, P and S were obtained by carbonisation of the initial OPZs. The chemical and textural structures of the CNS were characterised by electron microscopy, elemental analysis, spectroscopy, XRD and N_2 physisorption. The properties of the CNS were correlated with the carbonisation temperature; a detail analysis of the gas evolution during the carbonisation process along with the XPS data showed the dependence of the carbon microporous structure with the carbonisation temperature which in turn affected the heteroatom at% concentration and binding state. The electrochemical properties of the CNS were tested in LIBs coin half cells. The sample prepared at 850 °C showed a remarkable stability and high Coulombic efficiency over 1100 charge/discharge cycles. This performance was attributed to both the combination of high surface area and the presence of beneficial pyridinic-N species. Moreover, the nature of surface functional groups had an impact on the irreversible capacity.

Finally, the organophosphazene chemistry was extended to the facile production of OPZ@BaTiO$_3$ and C@BaTiO$_3$ core-shell nanoparticles. The advantages of the applied method over others relied on two facts: i) a pre-treatment step of BaTiO$_3$ was eliminated since OPZ chemistry can be applied to almost any surface regardless of the surface physiochemical properties; and ii) the production of materials with two different electronic properties (insulators and conductors) by the same butch synthesis. The OPZ@BaTiO$_3$ showed that the relative permittivity was dependent of the shell thickness. However, most of the samples showed frequency independence of the relative permittivity and only the sample with the thinnest OPZ shell (4 nm) exhibited decreasing dielectric constant with increasing frequency. The low dielectric loss, stable dielectric constant (ε_r) vs. frequency and ability to control the shell-thickness by adjusting the synthetic parameters have placed the current core-shell

technology in a favourable position for further dielectrics development. Additionally, the facile conversion of the insulating OPZ@BaTiO$_3$ to electron conductive C@BaTiO$_3$ has offered more opportunities to tailor the electrical properties of the nanomaterials.

6.2 Future development

The results of Chapters 2 & 3 are expected to establish a new philosophy on the synthesis of cyclomatrix organophosphazene nanostructures. A careful combination of the nucleophile with the appropriate organic base and solvent is necessary not only for the exploration of new materials but also for the minimisation of time and cost of the production.

Despite the advantageous and facile fabrication of OPZ-derived heteroatom-doped carbons there is an intrinsic limitation: the estimation of the absolute effect of the heteroatom-doping on the electronic properties of the carbon structure are hindered by the simultaneous effect on the textural properties. The reason can be explained from the next example; two co-building blocks carrying different functional groups thus heteroatoms will produce OPZs of different structure. Thus, their carbon analogues would have not only different heteroatom-doping but also different microporous structures. Nevertheless, a continuous research on such carbon materials is necessary in order to get in-depth knowledge on new heteroatom-dopants.

Last but not least, both OPZ@BaTiO$_3$ and C@BaTiO$_3$ need to be tested as fillers in PVDF composites in order to better understand their properties as potential dielectric and electroactive materials. The OPZ nanospheres of this project, showed ε_r of 15 at 1 kHz, which is close to the reported values for neat PVDF films ($\varepsilon_r \approx 10$ at 1 kHz). This "compatibility" of the e_r values would be beneficial for OPZ-based PVDF nanocomposites, since the lower differences in ε_r between the polymer matrix and the inorganic filler lead to homogenous electric field, thus higher dielectric breakdown filed strength.[1]

6.3   References

1.   P. Barber, S. Balasubramanian, Y. Anguchamy, S. Gong, A. Wibowo, H. Gao, H. Ploehn and H.-C. Zur Loye, *Materials*, 2009, **2**, 1697.